Numeričko modeliranje procesa izgaranja e-goriva polioksimetilen dimetil etera

Pečaver Šošić, Dominik

Master's thesis / Diplomski rad

2021

Degree Grantor / Ustanova koja je dodijelila akademski / stručni stupanj: **University of Zagreb, Faculty of Mechanical Engineering and Naval Architecture / Sveučilište u Zagrebu, Fakultet strojarstva i brodogradnje**

Permanent link / Trajna poveznica: https://urn.nsk.hr/urn:nbn:hr:235:278663

UNIVERSITY OF ZAGREB

FACULTY OF MECHANICAL ENGINEERING AND NAVAL ARCHITECTURE

MASTER'S THESIS

Dominik Pečaver Šošić

Zagreb, 2021.

UNIVERSITY OF ZAGREB

FACULTY OF MECHANICAL ENGINEERING AND NAVAL ARCHITECTURE

NUMERICAL MODELLING OF THE COMBUSTION PROCESS OF E-FUEL POLYOXYMETHYLENE DIMETHYL ETHER

Mentor:

Izv. prof. dr. sc. Milan Vujanović

Student:

Dominik Pečaver Šošić

Zagreb, 2021.

This Master's thesis was funded under the auspice of the European Regional Development Fund, Operational Programme Competitiveness and Cohesion 2014−2020, KK.01.1.1.04.0070.

I hereby declare that this thesis was composed by myself, that the work contained here is my own, except where stated otherwise. All references have been acknowledged and fully cited.

I would like to thank my supervisor Milan Vujanović for his guidance and all the help during the writing of this thesis.

I would like to thank Dr. Schmalhorst from AVL Munchen and Dr. Priesching from AVL Graz for their guidance and advice.

Very special thanks to Filip Jurić, who was always available to help and offered his assistance for every problem, no matter how difficult.

I would like to thank my family, especially my father and grandmother, for their support, patience and encouragement to finish my studies.

Dominik Pečaver Šošić

SVEUČILIŠTE U ZAGREBU
FAKULTET STROJARSTVA I BRODOGRADNJE
Središnje povjerenstvo za završne i diplomske ispite
Povjerenstvo za diplomske ispite studija strojarstva za smjerove:
Procesno-energetski, konstrukcijski, inženjersko modeliranje i računalne simulacije i brodostrojarski

Sveučilište u Zagrebu Fakultet strojarstva i brodogradnje	
Datum	Prilog
Klasa: **602 - 04 / 21 - 6 / 1**	
Ur.broj: **15 - 1703 - 21 -**	

MASTER'S THESIS

Student: **Dominik Pečaver Šošić** JMBAG: 0035203577

Title of thesis in Croatian: **Numeričko modeliranje procesa izgaranja e-goriva polioksimetilen dimetil etera**

Title of thesis in English: **Numerical Modelling of the Combustion Process of E-Fuel Polyoxymethylene Dimethyl Ether**

Assignment description:

In order to meet the reduction of carbon dioxide emissions, carbon-neutral synthetic fuels (e-fuels) produced by the catalytic conversion of water and carbon dioxide are drawing increasing attention from both academic research and industry. Carbon-neutral synthetic fuels are produced by hydrogenating carbon dioxide from the air or exhaust gases to store excess electricity from renewable sources. An e-fuel applicable in existing internal combustion engines is polyoxymethylene dimethyl ether (OME), which shows similar combustion characteristics as conventional fuels in the transport sector. Computational fluid dynamics and chemical kinetics or combustion models are commonly used to investigate the combustion and self-ignition properties of new fuels, including e-fuels. Within the Master's thesis, it is necessary to:

1. Present a brief overview and classification of e-fuels and technologies for the synthesis of e-fuel by the electricity generated from the renewable energy sources;
2. Present into details the technologies for production, characteristics, and chemical mechanisms of e-fuel trioxymethylene dimethyl ether $CH_3O(CH_2O)_3CH_3$, (OME-3);
3. Describe the fundamental equations of computational fluid dynamics and describe the equations of modelling chemical kinetics using the chemical mechanisms of fuel combustion;
4. Present numerical models used for numerical calculations;
5. Using the commercial software package "AVL FIRE ™ Workflow Manager" perform a detailed numerical simulation on the moving computational mesh of an industrial internal combustion engine;
6. Analyse and compare the obtained results with the conventional fuel combustion process results and available experimental data.

All necessary literature, model description, input, and initial data for analysis will be obtained from the mentor and co-supervisor.

It is necessary to reference the used literature and any help received.

Thesis assigned:	Thesis submission date:	Thesis defence date:
March 4th, 2021	May 6th, 2021	May 10th –14th, 2021

Supervisor:

Izv. prof. dr. sc. Milan Vujanović

Committee Chair:

Prof. dr. sc. Tanja Jurčević Lulić

Table of contents

List of figures

List of tables

Nomenclature

Label	Unit	Description
A		Pre-exponential factor in Arrhenius law
A_S	m^2	Surface area
C		Model constant
c	$kmol/m^3$	Concentration
D	m	Droplet diameter
D_k	m^2/s	Diffusion coefficient
E	J/kg	Activation energy
e	J/kg	Specific energy
F_d	N	Drag force
f		Fuel mixture fraction
f_i	m/s^2	Resulting volume force
g		Residual gas mass fraction
k	m^2/s^2	Turbulent kinetic energy
k		Global reaction rate coefficient
L	m	Turbulence length scale
M	kg/kmol	Molar mass
P_k	m^2/s^3	Production of turbulent kinetic energy
p	Pa	Pressure
q	W/kg	Specific heat
R	J/molK	Ideal gas constant
r	m	Droplet radius
S_k		Source term
t	s	Time
T	K	Temperature
T	s	Turbulence time scale
u	m/s	Velocity
x_i	m	Coordinates
y		Mass fraction
α	W/m^2K	Coefficient of convective heat transfer

β		Coefficient in Arrhenius law
Γ	m^2/s	Diffusion coefficient
ε	m^2/s^3	Turbulent energy dissipation rate
ζ	m/s	Velocity scale ratio
κ		Chemical symbol for species k
Λ	m	Wave length
λ	W/mK	Thermal conductivity
μ	Pas	Dynamic viscosity
μ_t	Pas	Turbulent viscosity
ν		Stoichiometric coefficient
ρ	kg/m^3	Density
Σ	1/m	Flame surface density
σ_{ji}	N/m^2	Stress tensor
τ	N/m^2	Viscous stress
τ_a	s	Break-up time
υ	m^2/s	Kinetic viscosity
Ω	s	Wave growth rate
ω	kg/m^3s	Combustion source

Abbreviation	
BDC	Bottom Dead Centre
CA	Crank Angle
CFD	Computational Fluid Dynamics
DDM	Discrete Droplet Method
DME	Dimethyl ether
DMM	Dimethoxymethane (methylal)
EGR	Exhaust Gas Recirculation
FT	Fischer Tropsch
ICE	Internal Combustion Engine
LHV	Lower Heating Value
LLNL	Lawrence Livermore National Laboratory
OME	Poly-oxymethylene Dimethyl Ether

P2G	Power-to-Gas
P2L	Power-to-Liquid
RES	Renewable Energy Sources
SST	Standard Species Transport
TDC	Top Dead Centre

Dimensionless quality	
Nu	Nusselt number
Pr	Prandtl number
Re	Reynolds number
Sc	Schmidt number

Abstract

In order to meet the reductions of carbon dioxide, carbon-neutral synthetic fuels are drawing attention as an alternative to fossil fuels. One particular fuel, which can be implemented in existing internal combustion engines and shows similar combustion characteristics as conventional fuels, is polyoxymethylene dimethyl ether (OME). Computational fluid dynamics is often used to assess and test the properties of new fuels, including e-fuels. In this work, an overview of e-fuels and synthesis technologies is given, with an emphasis on OME-3. Furthermore, a numerical simulation of the combustion process with this e-fuel was conducted in the computational fluid dynamics software AVL FIRE™. The simulation was verified by comparing the simulation data for n-heptane as fuel and validated with experimental data provided by AVL GmbH Graz. For the simulations with OME-3, both chemical kinetics and a combustion model were used to compare results. Two cases, one being a single injection case, the other being a multi-injection case, were used in 3 different injection regimes to assess how e-fuel OME-3 compares to n-heptane fuel, which is a substitute for diesel fuel. By varying the injection profile and injected mass of fuel of OME-3, results which were more comparable to conventional fuel were achieved.

Keywords: Internal combustion engine, E-Fuel, OME-3, numerical simulation, CFD

Sažetak

Kako bi se zadovoljili propisi za smanjenje ugljičnog dioksida, ugljično neutralna sintetička goriva privlače sve više pozornosti kao alternative fosilnim gorivima. Posebna vrsta goriva koje se može primijeniti u postojeće motore s unutarnjim izgaranjem i pokazuje slične karakteristike izgaranja kao i konvencionalna goriva, je polioksimetilen dimetil eter (OME). Računalna dinamika fluida često se koristi za procjenu i ispitivanje svojstava novih goriva, uključujući sintetska goriva. U ovom radu dan je pregled sintetskih goriva i tehnologija sinteze, s naglaskom na trioksimetilen dimetil eter OME-3. Nadalje, numerička simulacija procesa izgaranja s ovim sintetskim gorivom provedena je u računalnom softveru za dinamiku fluida AVL FIRE™. Simulacija s OME-3 gorivom je uspoređena s rezultatima simulacija koje su koristile n-heptan kao gorivo i validirana eksperimentalnim podacima koje je ustupio AVL GmbH Graz. Za simulacije s OME-3 korištena je kemijska kinetika i model izgaranja za usporedbu rezultata. Dva slučaja, od kojih je jedan slučaj s jednim ubrizgavanjem, a drugi slučaj s više ubrizgavanja goriva, korištena su u 3 različita režima ubrizgavanja kako bi se procijenilo izgaranje sintetskog goriva OME-3 naspram n-heptana, koje je predstavljalo zamjenu za dizel gorivo. Promjenom profila ubrizgavanja i ubrizgane mase goriva OME-3 postignuti su rezultati u skladu s konvencionalnim gorivom.

Ključne riječi: Motor s unutarnjim izgaranjem, Sintetsko gorivo, OME-3, numerička simulacija, CFD

Proširenisažetak

Uvod

Sve stroži propisi o emisijama CO2 u prometnom sektoru dovode do situacije da se fosilna goriva polako istiskuju iz upotrebe, sve u cilju dekarbonizacije i ugljične neutralnosti. Kao alternativa fosilnim gorivima, javljaju se ugljično neutralna sintetička goriva koja se mogu proizvoditi katalitičkom pretvorbom vode i ugljikovog dioksida. Oni predstavljaju izvrstan način za pohranu viška energije iz obnovljivih izvora energije, i predstavljaju alternativu spremanju energije u baterije. Jedna posebno zanimljiva kategorija sintetskih goriva je kategorija oksigeniranih goriva poput polioksimetilen dimetil etera (OME), koja se mogu koristiti u trenutnim motorima s unutarnjim izgaranjem s manjim ili nepostojećim preinakama samog motora. Također imaju slična svojstva samozapaljenja kao benzin ili dizel gorivo. Vrsta OME goriva, 3-oksimetilen dimetil eter (OME-3), pokazuje dobra svojstva za upotrebu u dizelskim motorima. Korištenjem računalne dinamike fluida, mogu se brzo i efikasno procijeniti prednosti i nedostatci upotrebe OME-3 kao goriva. Glavni cilj ovog rada bio je usporediti performanse konvencionalnog goriva (n-heptana) i sintetskog goriva (OME-3) u numeričkoj simulaciji izgaranja u dizel motoru.

Pregled sintetskih goriva

Sintetska goriva se mogu podijeliti u više kategorija s obzirom na način pohrane energije:

a) Pohrana u obliku prirodnog plina
b) Pohrana u obliku kapljevitog goriva
c) Pohrana u amonijak

Prvi korak u svim metodama je proizvodnja vodika elektrolizom koju pokreću obnovljivi izvori energije. Proizvedeni vodik može se kombinirati s CO2 ili dušikom tijekom procesa metaniranja, rasplinjavanja i Fischer-Tropsch te Haber-Bosch sinteze kako bi se dobio metan, kapljevita goriva ili amonijak.

Polioksimetilen dimetil eteri s duljinom lanca n u rasponu od 3 do 5 (OME3-5) smatraju se najprikladnijim aditivima za dizel gorivo zbog svojih povoljnih svojstava poput: cetanskog broja i temperature zapaljenja unutar granica norme EN 590 i relativno visoke viskoznosti. Usto se smatra da se dodavanjem OME u dizel gorivo drastično može smanjiti količina čađe u ispušnim plinovima.

Načini sinteze OME-3 se mogu podijeliti na:

a) Neizravna sinteza (konvencionalna metoda)
b) Proizvodnja izravnom oksidacijom metanola
c) Proizvodnja izravnim hidrogeniranjem ugljikovog dioksida

Neizravna sinteza je zasad najučestalija metoda dobivanja OME-3 goriva. Proces počinje djelomičnom oksidacijom metanola u formaldehid. Vodena otopina formaldehida se koncentrira i uz pomoć katalizatora se proizvodi trioksan. Trioksan ili koncentrirani formaldehid tada reagiraju s metanolom dajući OME-1. Konačno, OME-1 reagira s trioksanom stvarajući OME-n s dužim lancima ($n \geq 2$).

Proizvodnja izravnom oksidacijom metanola je noviji pristup proizvodnji OME-3 odnosno OME-1 goriva iz kojeg se onda proizvodi OME-3. Pristup se temelji na oksidaciji plinovitog metanola uz pomoć bifunkcionalnog katalizatora u reaktoru s fiksnim slojem. Katalizator mora omogućavati da se istovremeno odvija oksidacija metanola u formaldehid te pretvorba metanola i formaldehida u OME-1.

Proizvodnja izravnim hidrogeniranjem ugljikovog dioksida je najnoviji pristup proizvodnji OME-3 goriva. Pristup se temelji na metodi koja bi omogućila dobivanje OME-1 u samo jednom koraku kroz direktno hidrogeniranje ugljikovog dioksida uz prisustvo metanola. Metoda je još uvijek u eksperimentalnoj fazi, no smatra se da će omogućiti uštede energije, manju potrošnju vodika i u usporedbi s drugim metodama manje komponenti u sustavu.

Matematički model

U računalnoj dinamici fluida, strujanje fluida je opisano sa zakonom očuvanja mase, zakonom očuvanja količine gibanja, zakonom očuvanja energije i zakonom očuvanja mase kemijskih vrsta:

$$\frac{\partial \rho}{\partial t} + \frac{\partial}{\partial x_j}\left(\rho u_j\right) = 0$$

$$\frac{\partial}{\partial t}\left(\rho u_i\right) + \frac{\partial}{\partial x_j}\left(\rho u_i u_j\right) = \rho f_i + \frac{\partial \sigma_{ji}}{\partial x_j}$$

$$\frac{\partial}{\partial t}\left(\rho e\right) + \frac{\partial}{\partial x_j}\left(\rho e u_j\right) = \rho f_i u_i + S + \frac{\partial}{\partial x_j}\left(\sigma_{ji} u_i - q_j\right)$$

$$\frac{\partial}{\partial t}(\rho Y_k) + \frac{\partial}{\partial x_j}(\rho Y_k u_j) = \frac{\partial}{\partial x_j}\left(\rho \gamma_k \frac{\partial Y_k}{\partial x_j}\right) + S_k$$

Model turbulencije

Strujanje fluida se može podijeliti na laminarno, prijelazno i turbulentno, no u inženjerskoj praksi je skoro uvijek turbulentno. Za modeliranje turbulencije korišten je model k-zeta-f koji je podržan u programu AVL FIRE™.

Model spreja

Za modeliranje procesa spreja korišten je Euler Lagrangian pristup diskretnih kapljica u kojem se kapljice grupiraju u skupine kapljica (parcele) koje imaju slična fizikalna svojstva. Za kapljevitu fazu rješavaju se Lagrangeove jednadžbe, dok se za plinovitu fazu rješavaju Eulerove.

Za modeliranje spreja sljedeći pod modeli su bili korišteni:

- Model raspadanja čestica - WAVE
- Model isparavanja - Dukowicz
- Model turbulentne disperzije
- Model sile otpora – Schiller – Naumann
- Model međudjelovanja sa zidom – Walljet1

Modeliranje izgaranja

Modeliranje izgaranja se vršilo na dva načina:

- Korištenjem kemijskog mehanizma (kemijske kinetike)
- Korištenjem modela izgaranja

Korištenjem kemijskog mehanizma, za svaku kemijsku vrstu računaju se transportne jednadžbe. Izvorski član u jednadžbi očuvanja mase kemijskih vrsta se modelira pomoću Arrheniusove jednadžbe:

$$k = AT^{\beta} \exp\left(-\frac{E}{RT}\right)$$

Gdje je k globalni koeficijent brzine reakcije, a koeficijenti A, β and E su predeksponencijalni faktor, faktor ovisnosti o temperaturi i energija aktivacije.

Korištenjem modela izgaranja rješava se znatno manji broj transportnih jednadžbi za očuvanje kemijske vrste. U izabranom modelu ECFM-3Z rješavaju se transportne jednadžbe za sljedeće kemijske vrste: O2, N2, NO, CO2, CO, H2, H2O, O, H, N, OH. Dodatno se rješavaju još 3 transportne jednadžbe u okviru standardnog transportnog modela za gorivo, maseni udio goriva i maseni udio zaostalih ispušnih plinova. U samom modelu ECFM-3Z područje izgaranja je podijeljeno u 3 zone: zona čistog goriva, zona čistog zraka s mogućim udjelom zaostalih plinova te zona pomiješanog zraka i goriva.

Modeliranje emisija

Izgaranjem dizelskog goriva oslobađaju se između ostalog, znatne količine dušikovih oksida (NO_x). Tri su glavna načina formiranja NO emisija: uslijed disocijacije molekularnog zraka - dušika pri visokim temperaturama, tijekom izgaranja ugljikovodika na plamenoj fronti i zbog komponenata u gorivu koje sadrže dušik. Za modeliranje emisija NO_x korišten je prošireni Zeldovich model.

Numeričke postavke

Mreža za numeričke simulacije je napravljena u programu AVL ESE Diesel. Model motora je Volvo I5D i njegove specifikacije, a i specifikacije brizgaljke su dane u Tablici 1.

Tablica 1 *Specifikacije motora i brizgaljke*

Podaci o motoru	
Promjer cilindra	81 mm
Stapaj	93,15 mm
Duljina klipnjače	147 mm
Kompresijski omjer	16,5 : 1
Volumen	2,4 l
Broj cilindara	5
Podaci o brizgaljki	
Broj rupa	7
Kut konusa spreja	145°
Protok (pri Δp =100 bar)	440 ml / 30 s
Oblik kupole mlaznice	Micro Sac

Izgled mreže sa selekcijama za rubne uvjete, prikazan je na Slici 1. Mreža je kreirana za 1/7 volumena cilindra zbog činjenice da brizgaljka ima 7 rupa za ubrizgavanje goriva, a u simulaciji se simulira samo jedna mlaznica.

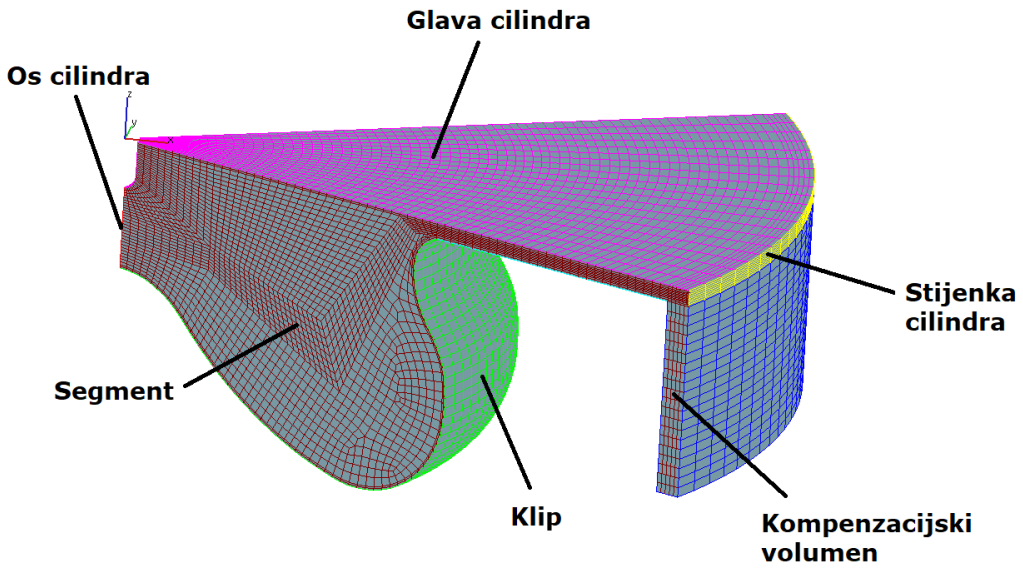

Slika 1 *Mreža sa selekcijama za rubne uvjete*

Rubni uvjeti simulacije su dani u Tablici 2.

Tablica 2 *Rubni uvjeti*

Selekcija	Rubni uvjet
Klip	Tip: Zid Temperatura: 473 K
Stijenka	Tip: Zid Temperatura: 423 K
Os	Tip: Simetrija
Segment	Tip: Cirkulacija Ulaz/Izlaz
Kompenzacijski volumen	Tip: Zid, Pomična mreža
Glava cilindra	Tip: Zid Temperature: 443 K

U sklopu rada, postavljena su dva različita slučaja, jedan opisuje jednokratno ubrizgavanje goriva u cilindar (slučaj A), dok drugi opisuje višekratno ubrizgavanje goriva u cilindar (slučaj

B), konkretno, četiri puta se odvija ubrizgavanje goriva. Kako bi se procijenilo ponašanje OME-3 goriva u dizel motoru i pod sličnim uvjetima izgaranja, provedena su tri režima ubrizgavanja goriva. Prvi je identičan režimu ubrizgavanja n-heptana, gdje se ubrizgava ista masa OME-3 kao u eksperimentu s n-heptanom. Drugi režim sadrži više ubrizgane mase kako bi odgovarao oslobođenoj energiji n-heptana, što podrazumijeva dulji period ubrizgavanja goriva. Treći režim je gotovo identičan drugom s obzirom na trajanje ubrizgavanja, dok su početak i kraj ubrizgavanja promijenjeni, a to je najuočljivije u slučaju višestrukog ubrizgavanja. Profili ubrizgavanja goriva za slučaj A i B, tijekom prvog i drugog režima ubrizgavanja, prikazani su na Slikama 2 i 3. Plavom bojom su označeni profili ubrizgavanja tijekom prvog režima, a narančastom bojom tijekom drugog režima.

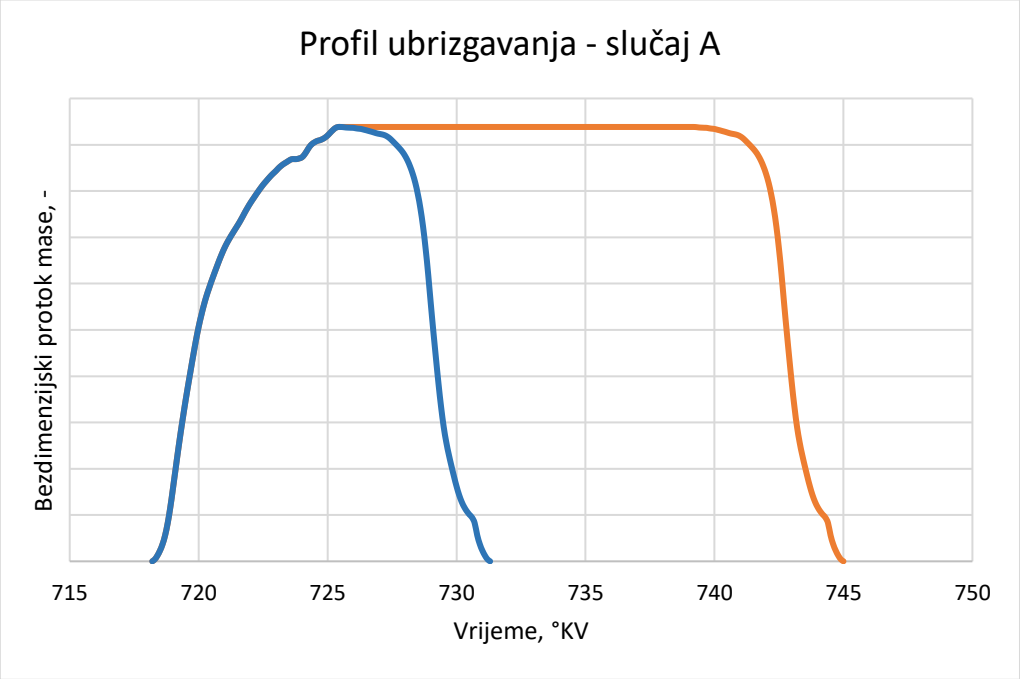

Slika 2 *Profil ubrizgavanja goriva – slučaj A – usporedba prvog (plavo) i drugog (narančasto) režima ubrizgavanja*

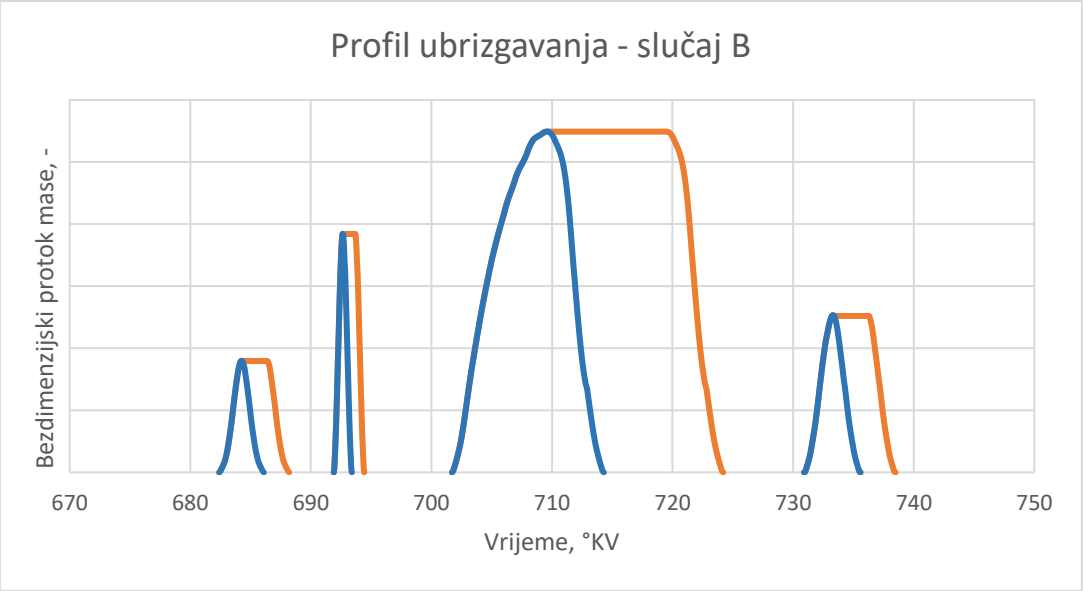

Slika 3 *Profil ubrizgavanja goriva – slučaj B – usporedba prvog (plavo) i drugog (narančasto) režima ubrizgavanja*

Rezultati

Za svaki pojedini slučaj i režim ubrizgavanja, dvije simulacije s OME-3 gorivom su prikazane. Jedna simulacija je koristila kemijski mehanizam Lin et al., dok je druga simulacija koristila model izgaranja ECFM-3Z. Lin et al. mehanizam se sastoji od 61 kemijske vrste i 190 kemijskih reakcija. Osim što su se rezultati tih simulacija uspoređivali međusobno, oni su se uspoređivali i s eksperimentalnim podacima i rezultatima simulacije za n-heptan.

S obzirom na to da OME-3 gorivo ima manju ogrjevnu vrijednost od n-heptana, očekivano je da će uz istu ubrizganu masu gorivo, OME-3 uzrokovati manje tlakove u cilindru i manju oslobođenu energiju nego n-heptan. Rezultati za prvi režim ubrizgavanja pokazuju upravo takvu situaciju.

Drugi i treći režim ubrizgavanja zato ubrizgavaju veću količinu goriva kako bi kompenzirali taj efekt. Razlika između drugog i trećeg režima je ta što je treći režim ubrizgavanja dodatno optimirao režim ubrizgavanja. Početci ubrizgavanja goriva su pomaknuti kako bi se dobile vrijednosti koje su sličnije eksperimentu s n-heptanom.

Rezultati tijekom trećeg režima ubrizgavanja pokazuju kako Lin et al. mehanizam i ECFM-3Z model postižu nešto manje tlakove za slučaj A nego n-heptan u simulaciji i eksperimentu, što je i vidljivo u Slici 4. Temperature za OME-3 su u prosjeku nešto niže nego kod n-heptana i porast u temperaturi je sporiji nego kod n-heptana. Isto tako, brzina oslobađanja energije je

manja za OME-3 nego kod n-heptana teje ravnomjernija nego za n-heptan, što je vidljivo u Slici 5. U slučaju B, vrijednosti tlaka za OME-3 su nešto veće nego za n-heptan te je porast tlaka više linearan, što može upućivati da je OME-3 gorivo bolje iskorišteno u slučaja kada se ubrizgavanje vrši u više ubrizgavanja. Vrijednosti tlaka su prikazane na Slici 6, dok je brzina oslobađanja energije prikazana na Slici 7.

Slučaj A

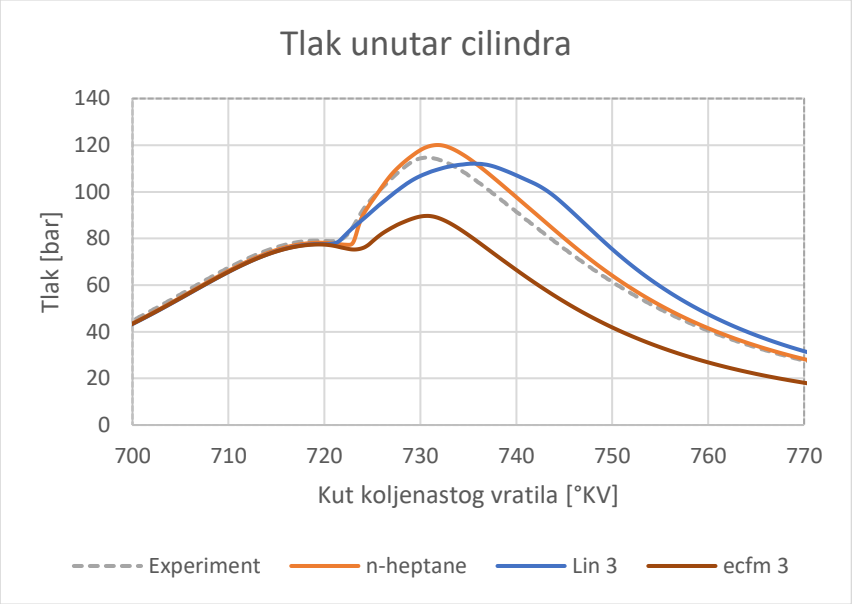

Slika 4 *Tlak unutar cilindra – slučaj A – treći režim ubrizgavanja*

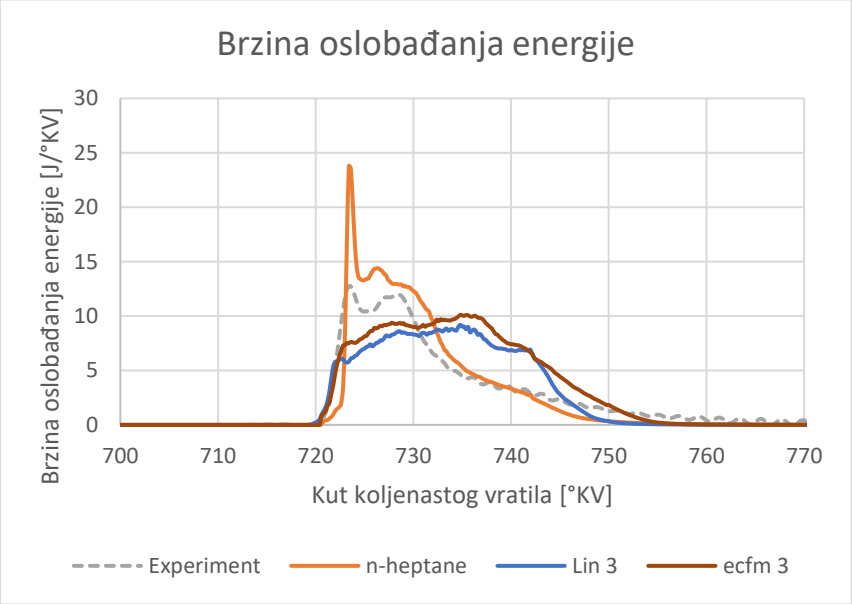

Slika 5 *Brzina oslobađanja energije – slučaj A – treći režim ubrizgavanja*

Slučaj B

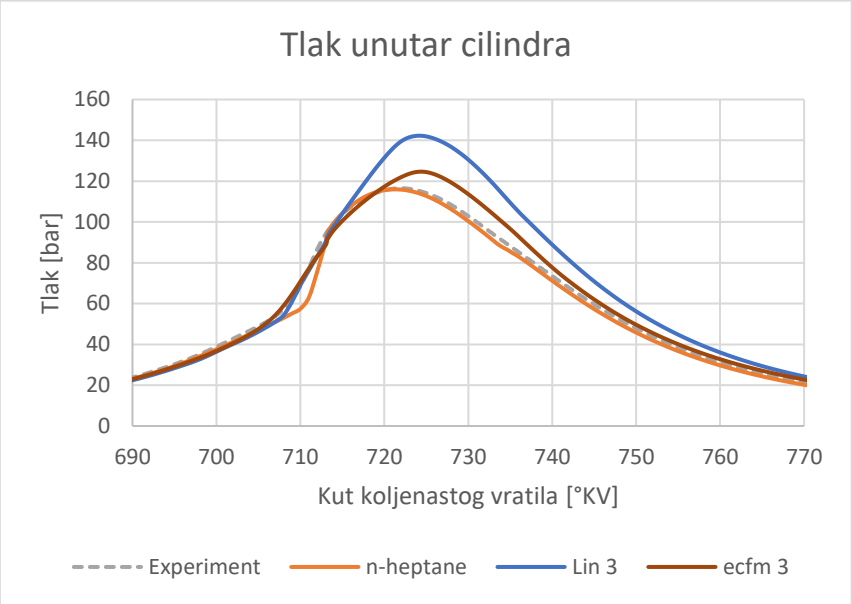

Slika 6 *Tlak unutar cilindra – slučaj B – treći režim ubrizgavanja*

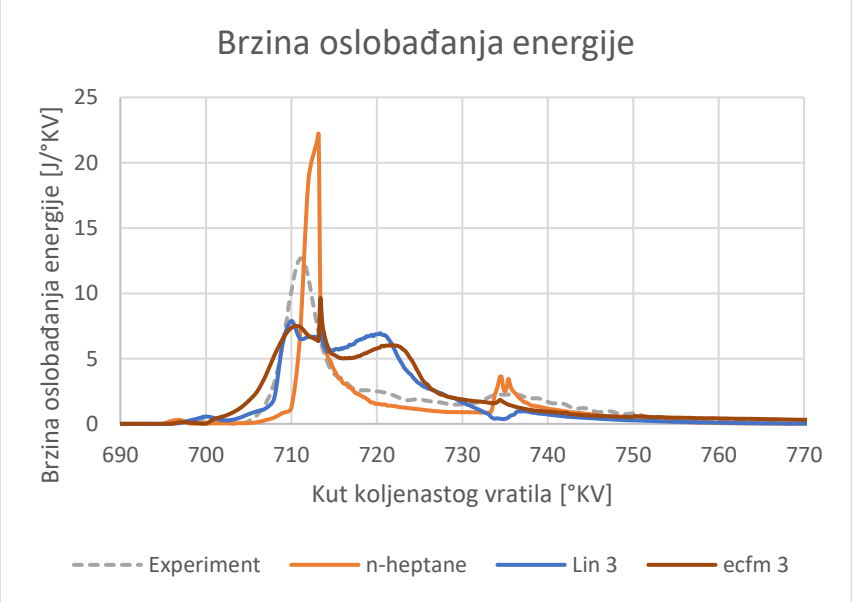

Slika 7 *Brzina oslobađanja energije – slučaj B – treći režim ubrizgavanja*

1. Introduction

More and more stringent regulations regarding CO_2 emissions in the transport sector (and in general) lead to the situation where fossil fuels are slowly being pushed out of the energy mix since the main goal of these regulations is decarbonisation and carbon neutrality of the sector. This puts car manufacturers in an inconvenient position since most of cars produced today are powered by internal combustion engines (ICE), and they, in most part, use fossil fuels. Car manufacturers but also governments have few options to solve this problem. One option is to focus on and encourage developing electric vehicles and the infrastructure surrounding them, which could mean a decrease of the ICE share in the transport sector, which was being developed and improved over a century. Another option that does not involve retiring the ICE and liquid fuels technology is introducing carbon-neutral synthetic fuels as a valid alternative to fossil ones. The production of synthetic fuels is a global and environmental issue and the subject of various EU directives that encourage infrastructure development around synthetic fuels. Even Porsche, an international automobile manufacturer, has announced plans to start producing synthetic fuel in order to prolong the availability of their high-performance sports cars [1].

Synthetic fuels are primarily liquid and gaseous fuels that are produced by a chemical process known as conversion. Synthetic fuels can be made from fossil fuels such as coal and natural gas, but this still does not solve the negative CO_2 impact of using the resulting synthetic fuels. The real potential lies in producing synthetic fuels from CO_2 and hydrogen, which would make the fuel carbon neutral. Since the production of these types of fuels also requires energy, it is envisioned that it is produced from renewable energy sources (RES).

In short, synthetic fuels produced from RES by catalytically converting water and CO_2 are precisely named e-fuels. These types of fuels are a great way to store excess energy produced by RES. They offer an alternative to storing energy in batteries with their drawbacks, some of which are the usage of rare and toxic elements and a relatively low energy density. This concept is just one of various others that fall in the category of power-to-X. The most notable examples of e-fuels are hydrogen, methane, and synthetic petrol and diesel.

One type of e-fuels that are particularly interesting is oxygenated fuels such as dimethyl ethers (DME) and Poly-oxymethylene dimethyl ethers (OME), which can be used in current ICE engines with minor or non-existent modifications to the engine itself. They also have similar autoignition characteristics as gasoline or diesel fuel. A type of OME fuel, 3-

oxymethylene dimethyl ether (OME-3), shows more promise for use in diesel engines. A comprehensive list of its physical and chemical properties is given in paragraph 2.4.1.

Even though OME-3 exhibits many favourable properties, OME-3 fuel should be evaluated and tested to see how it behaves in a real diesel engine and what phenomena occur during combustion. Since experiments can be expensive to conduct and require considerable planning, a preliminary Computational Fluid Dynamics (CFD) simulation is conducted to help understand the benefits and drawbacks of using OME-3 as a fuel.

With the increase in computer processing power, CFD offers a qualitative description and a quantitative description of the phenomena occurring during combustion. The simulation is conducted in the CFD simulation package software – AVL FIRE™. The piston and injector are modelled after the Volvo D5 engine. Cases simulating various loads for the engine were validated against experimental data to ensure the mesh and settings were acceptable for the simulation.

2. Overview of synthetic fuels

Synthetic fuels can be divided into several groups based on the way they are produced:

a) Power-to-Gas
b) Power-to-Liquid
c) Power-to-Ammonia

All of these groups of fuels can be further divided into subgroups, and a short overview will be given in the following paragraphs. Figure 1 shows a basic overview of Power-to-X technologies and processes. The first step in all methods is producing hydrogen via electrolysis powered by RES. The resulting hydrogen can be combined with CO_2 or nitrogen via methanation, gasification & Fischer-Tropsch synthesis, and Haber-Bosch synthesis to create methane, liquid fuels or ammonia.

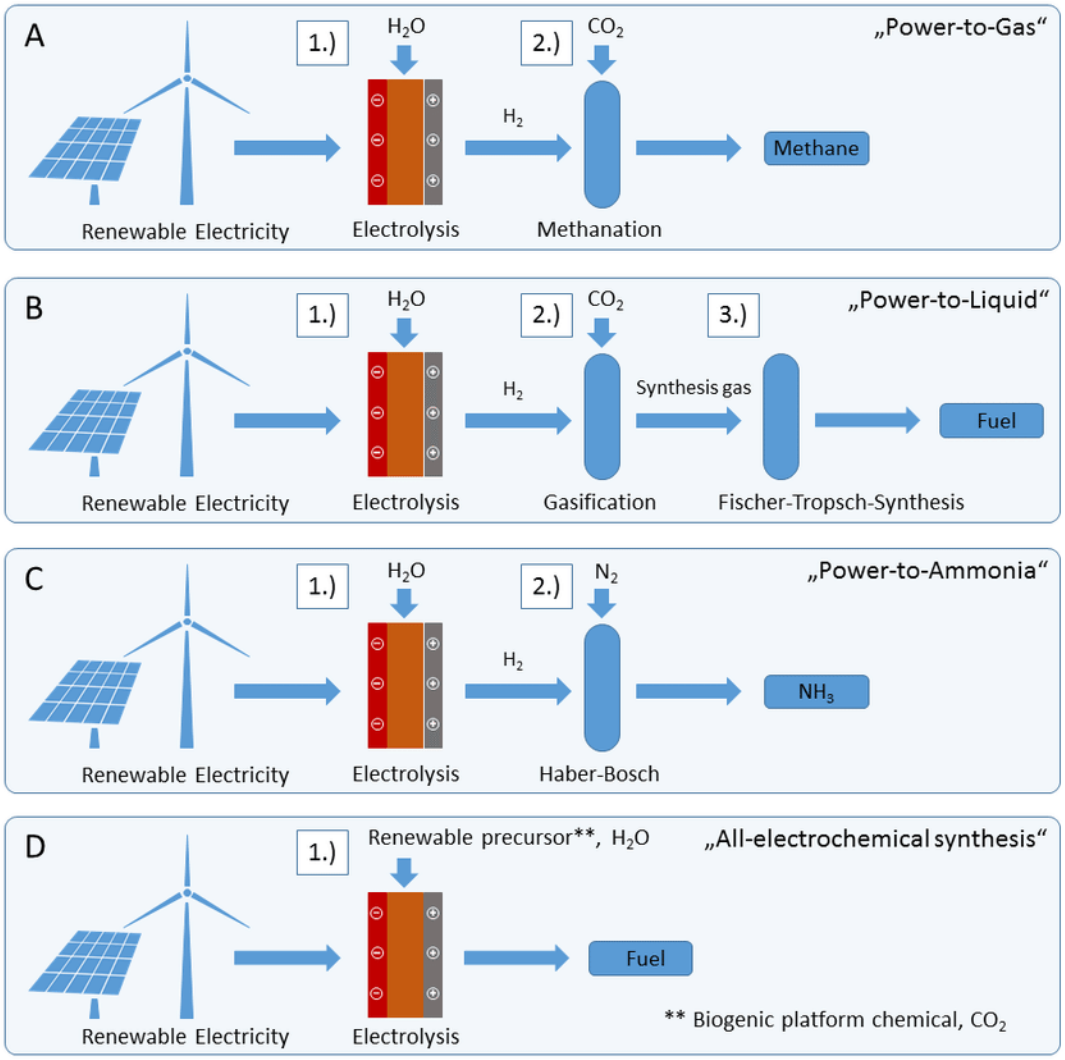

Figure 1 *Overview of various Power-to-X technologies* [2]

2.1. Power-to-Gas

Power-to-Gas (P2G) fuels are gaseous fuels produced by using electrical power. Most systems use electrolysis to produce hydrogen. Hydrogen is a key component in Power-to-X technologies in general. It can be used either directly, for combustion or for producing electricity in fuel cells, or as a component for producing syngas and other synthetic fuels.

As mentioned before, hydrogen is mainly produced via electrolysis. Water is thus split into hydrogen and oxygen molecules, so there are not any CO2 emissions compared to producing hydrogen from steam methane reforming. The main types of electrolysers are alkaline electrolysers, solid oxide electrolysers and polymer electrolyte membrane electrolysers with the latter gaining more attention since they offer more efficiency in hydrogen production.

The process is described with the equation:

$$2H_2O\ (l) \rightarrow 2H_2\ (g) + O_2\ (g) \quad (1)$$

Produced hydrogen can be used to create methane or syngas. In the process known as methanation, hydrogen is combined with carbon dioxide or even carbon monoxide to create synthetic natural gas (SNG). The process known as Sabatier reaction is described with the following equations:

$$CO + 3H_2 \rightarrow CH_4 + H_2O \quad (2)$$

$$CO_2 + 4H_2 \rightarrow CH_4 + 2H_2O \quad (3)$$

Methanation is a challenging process due to the high heat of the reaction and sensitive catalysts. One of the catalysts in wider use is Nickel due to its high selectivity and low cost [3].

2.2. Power-to-Liquid

Power-to-Liquid (PtL or P2L) fuels are liquid fuels produced mostly from syngas by using electrical power. The processes have some similarities with the ones used in P2G. However, P2L processes are more complex in comparison. Two main types of producing liquid fuels are via the Fischer Tropsch process and via methanol synthesis. Ammonia is also one type of synthetic fuel that could have been observed in this paragraph, but because of its specificness, it is described separately.

Fischer Tropsch (FT) process encompasses a range of reactions that convert syngas (usually a mixture of carbon monoxide and hydrogen) into liquid hydrocarbons. This process requires the

presence of metal catalysts and moderately high temperatures and pressures [4]. The reactions can be written as:

$$(2n + 1)H_2 + nCO \rightarrow C_nH_{2n+2} + nH_2O \quad (4)$$

And *n* typically ranges from 10 to 20. If the generated alkanes are straight-chained, they can be used as a diesel fuel since FT diesel is a mixture of various n-alkanes of different lengths [5]. Apart from creating FT diesel fuel, FT kerosene can also be created.

Methanol synthesis is another CO or CO_2 hydrogenation reaction. The difference between FT synthesis and methanol synthesis is that CO is not polymerised [6].

The process can be described with the equations:

$$CO + 2H_2 \leftrightarrow CH_3OH \quad (5)$$

$$CO_2 + 3H_2 \leftrightarrow CH_3OH + H_2O \quad (6)$$

The reactions are very exothermic, which provides a challenge to remove the excess heat. Even though methanol is produced with high selectivity due to the equilibrium limitation, the conversion rate per pass is limited and usually does not top over 25%. To overcome the limitation, unreacted syngas is recirculated, the operation temperature is lowered, and methanol is quickly removed during its production [7].

Methanol is an essential chemical and a vital component to producing synthetic gasoline and other oxygenated fuels like DMM and OME.

Gasoline is produced via the Mobil process [8] described in the equation:

$$nCH_3OH \rightarrow C_nH_{2n} + nH_2O \quad (7)$$

and *n* typically ranges from 3 to 10.

The produced gasoline is of high quality as it contains virtually no sulfur or benzene and octanes exceed the current regulatory requirements. As shown in Figure 2, gasoline can be produced with two types of reactors: an adiabatic fixed-bed and a fluid-bed reactor, suitable for producing larger quantities of the fuel since the reaction heat removal is simplified and can run continuously unlike the fixed-bed reactor. Fixed bed reactors are the simplest to design and consist of solid particles packed into the bed. They, however, have a problem with small catalyst surface area, which is solved with the fluid-bed reactor where better mixing of fluid and catalyst ensures an improved mass and heat transfer.

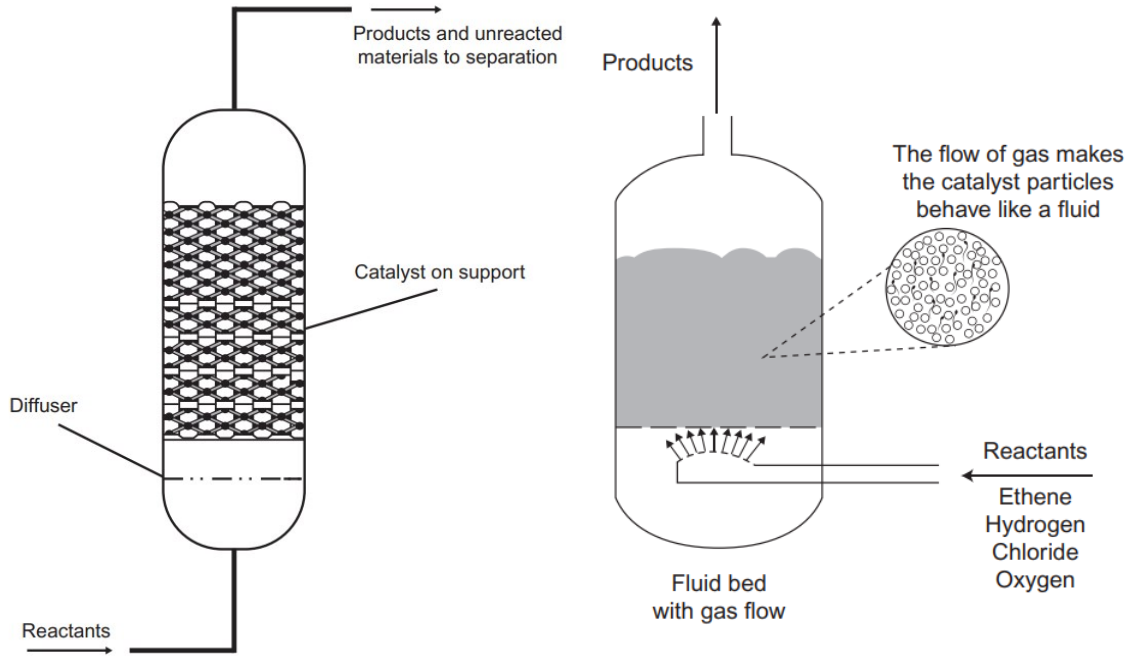

Figure 2 *Fixed bed reactor (left) & fluidised bed reactor (right)* [9]

For producing DME from methanol, the chemical reaction can be described with the following equation:

$$2CH_3OH \leftrightarrow CH_3OCH_3 + H_2O \tag{8}$$

Alternatively, it can be produced from syngas which can be described with the following chemical reaction:

$$3CO + 3H_2 \leftrightarrow CH_3OCH_3 + CO_2 \tag{9}$$

DME (dimethyl ether) is an organic compound being promoted as a synthetic fuel due to its excellent combustion properties (cetane number ranges from 55 to 60). It could be used as a substitute for petroleum gas or diesel fuel. The advantage of using DME as diesel fuel is that the diesel engine would require only minor modifications to run on DME. It also prevents soot formation in OME fuels since they do not have so many carbon covalent bonds [10].

2.3. Power-to-Ammonia

Ammonia is a compound with the chemical formula NH_3. It could be created by combining hydrogen made from water electrolysis and nitrogen from the air. It can be used as a chemical storage medium because of the high efficiency and low cost of nitrogen sourcing [11]. Nitrogen can be produced by cryogenically separating it from the air or using pressure swing adsorption

(PSA), or using a semi-permeable membrane [12]. Pure nitrogen and hydrogen enter a compression unit (centrifugal compressor) to increase the synthesis gas pressure.

The most common way to produce ammonia is the Haber-Bosch process, and it uses a high temperature/pressure reactor to convert the synthesis gas into ammonia [13].

2.4. Poly-oxymethylene dimethyl ethers

2.4.1. Physico-chemical properties

Polyoxymethylene dimethyl ethers (OME), like DME, are receiving more and more attention due to their favorable combustion properties and lower emissions of soot particles, hydrocarbons, and carbon monoxide compared to conventional diesel fuel [14]. However, there are a few advantages OME has over DME as a synthetic fuel: OME are liquid at ambient temperature, unlike DME, which is gaseous, and there is no miscibility gap between OME and diesel fuel, which occurs with DME under 0 °C [15].

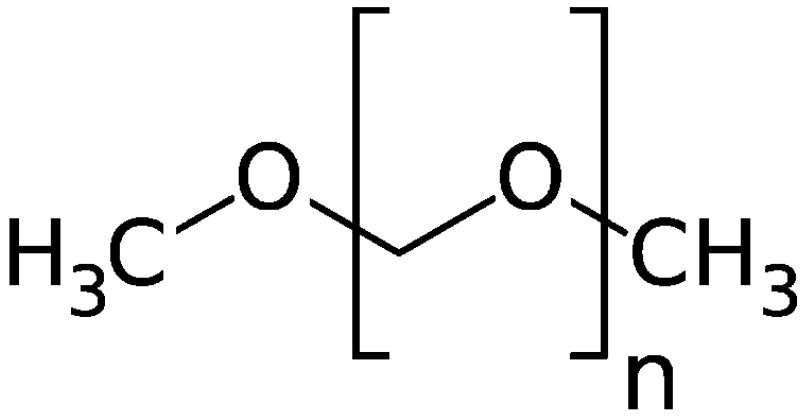

Figure 3 *Chemical formula of OME_n*

According to some studies [15][16], OME_{3-5} are the most suitable fuel additives to be used with current diesel engines. OME_{3-5} have higher cetane numbers than the minimum required by EN 590 for diesel fuel. Their flash points mostly meet the lower limit of 55 °C. OME with n in the range of 3-5 is mainly considered a fuel substitute due to the lower chain lengths. Although, for OME species with $n < 3$ feature that feature lower viscosity than diesel fuel, additional modification of the injector are required. Due to the lower vapour pressure and flash point, they do not meet the safety criteria. On the other hand, OME with $n > 5$ precipitate at temperatures below 18°C, leading to blockage of the fuel filter. This is shown in Table 1, along with other physical properties of OME_{1-6} currently found in literature [17].

***Table 1** Physico-chemical properties OME_{1-6}* [17]

	OME_1	OME_2	OME_3	OME_4	OME_5	OME_6
Molecular formula	$C_3H_8O_2$	$C_4H_{10}O_3$	$C_5H_{12}O_4$	$C_6H_{14}O_5$	$C_7H_{16}O_6$	$C_8H_{18}O_7$
Oxygen content [wt%]	42,1	45,3	47,1	48,2	49,0	49,6
Melting point [°C]	-105	-65	-41	-7	18,5	58
Boiling point [°C]	42	105	156	202	242	280
Density at 25°C [kg/m^3]	860	960	1020	1060	1100	1130
Lower heating value [MJ/kg]	22,4	20,6	19,4	18,7	18,1	17,7
Cetane number	29	63	78	90	100	104

OME fuels have a lower heating value and energy content than diesel fuel, leading to increased fuel consumption if used instead of diesel.

Since OME species do not contain carbon-carbon bonds, which are structural elements of soot, soot particle emissions are drastically lower. Also, soot precursors are degraded by hydroxyl radicals formed during the combustion of OME. This allows higher exhaust gas recirculation rates (EGR), which can reduce NO_x emissions. Adding as little as 5% of OME_2 to regular diesel fuel could decrease soot emissions by 30% [18].

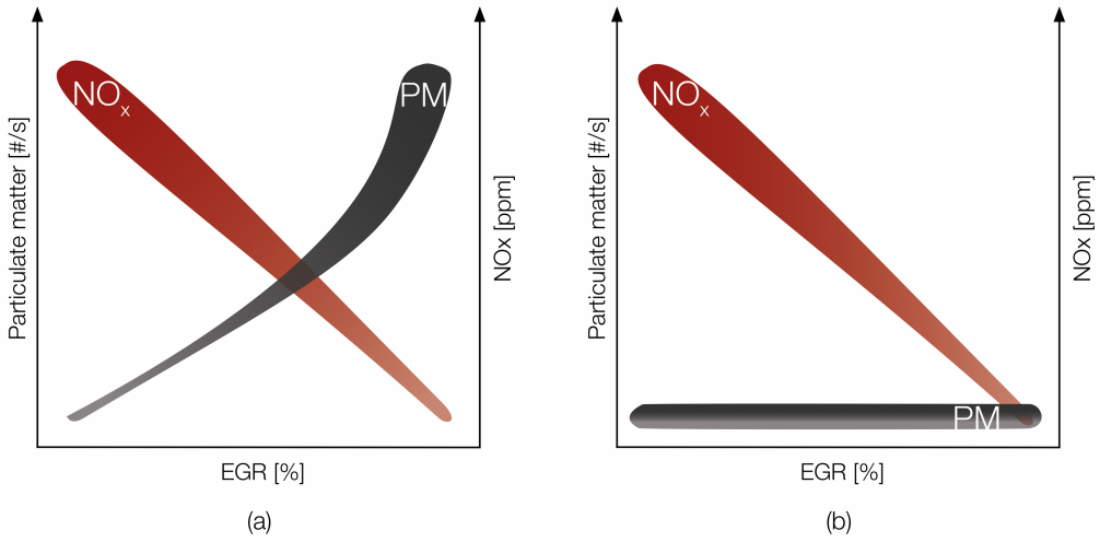

Figure 4 *Graph of particulate matter and NOx emissions versus EGR for combustion of (a) diesel & (b) OME* [19]

Figure 4 shows how OME can drastically decrease particulate matter emissions. and enable higher EGR rates to decrease NO_x emissions.

With conventional diesel fuel, increased EGR rates reduce the oxygen concentration in the combustion chamber and this leads to soot formation. The lower tendency for soot formation of OME allows for generating conditions of reduced soot but also NO_x emissions [20].

2.4.2. Production

OME species are produced by reacting a methyl-end ($-CH_3$) group provider and an oxymethylene ($-CH_2O-$) group provider under acidic conditions. Depending on the type of synthesis, the end group provider can be methanol or DMM, while the chain-group provider can be trioxane, paraformaldehyde or formaldehyde [17]. As shown in Figure 5, the main three production routes are indirect synthesis, direct oxidation of methanol and a reductive route.

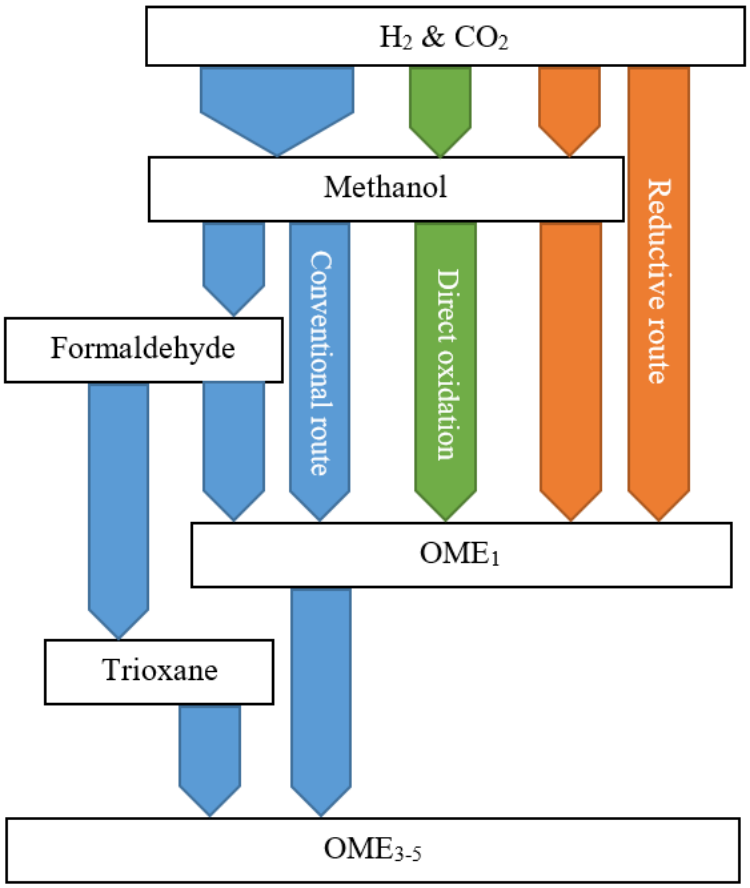

Figure 5 *Synthesis routes for OME_{3-5}* [21]

- **Indirect synthesis (conventional route)**

This is a standard route and the most common one. It starts with partial oxidation of methanol into formaldehyde (also known as Formox process). The aqueous solution of formaldehyde is concentrated and trimerised over an acid catalyst to produce trioxane. Trioxane or concentrated formaldehyde then reacts with methanol to yield OME_1. Finally, OME_1 reacts with trioxane to create OME_n with longer chains ($n \geq 2$) [22] [23]. Figure 6 shows the components needed to synthesise OME_n. It has to be noted that methylal is another name for OME_1, and that POMDME is another name for OME_n.

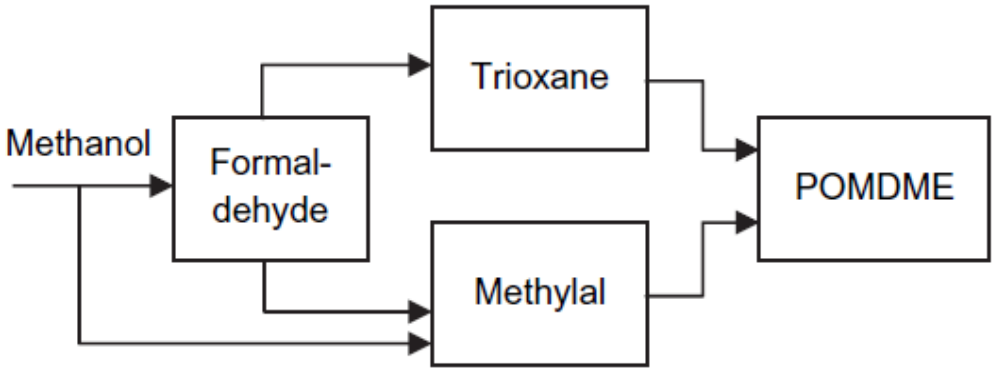

Figure 6 *Diagram of indirect synthesis of OME_{3-5}*

Methanol oxidises into formaldehyde over a catalyst such as iron-molybdenum, vanadium or silver. The reaction with iron-molybdenum and/or vanadium catalyst occurs from 300 up to 400 °C and can be written as:

$$CH_3OH + \frac{1}{2}O_2 \rightarrow CH_2O + H_2O \tag{10}$$

The reaction with a silver catalyst occurs at a higher temperature, at about 650 °C and includes 2 reactions to produce formaldehyde, the one shown before and also the dehydrogenation reaction:

$$CH_3OH \rightarrow CH_2O + H_2 \tag{11}$$

Trioxane is the chain-group provider as it provides a source of CH_2O. It is extracted from an aqueous formaldehyde solution by using sulfuric acid, which is described in the formula:

$$TRI \leftrightarrow 3CH_2O \tag{12}$$

In the next step, formaldehyde along with methanol, in the presence of an acid catalyst like sulfuric or hydrochloric acid, condensate and create OME in an aqueous solution [24] described as:

$$CH_2O + 2CH_3OH \rightarrow OME_1 + H_2O \tag{13}$$

Since this reaction is reversible, the yield of OME_1 is limited by chemical equilibrium. To counter this, low boiling OME_1 could be evaporated during the reaction.

The resulting OME_1 reacts with trioxane or formaldehyde to create OME of longer chain length:

$$OME_{n-1} + CH_2O \leftrightarrow OME_n \tag{14}$$

Catalysts used in the syntheses can be sulfuric or hydrochloric acids. However, they are corrosive, and the selectivity of OME_{3-5} is low. Ionic liquids can also be used as catalysts, but they are quite expensive, and it is not simple to reuse them and separate them from the products [17]. Molecular sieves were also documented as catalysts [24]. Other catalysts include ion exchange resins, sulfonated tetrafluoroethylene resins, heteropoly acids and zeolites.

This type of synthesis requires energy-intensive feed preparation steps, however, it produces a higher yield of OME_n than the feed since the resulting OME does not generate any H_2O.

- **OME_1 production via direct oxidation of methanol**

A newer approach to producing OME, precisely OME_1 is based on direct one-step oxidation of methanol to OME_1:

$$3CH_3OH(g) + \frac{1}{2}O_2(g) \rightarrow OME_1(g) + 2H_2O(g) \tag{15}$$

A solid bifunctional catalyst is used in a reactor in a fixed bed, where gaseous methanol and oxygen react to create OME_1, as shown in Figure 7. Formaldehyde is created inside the reactor and is subsequently acetalised in the presence of methanol to create the final product OME_1.

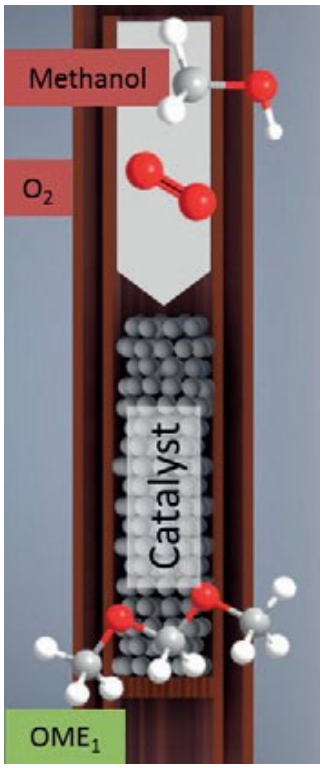

Figure 7 *Gasphase reactor for the direct oxidation of methanol* [21]

The required catalyst must be bifunctional, meaning it should have both metal and acid functionalities, the first enabling the oxidation of methanol to formaldehyde and the latter to enable the transformation of methanol and formaldehyde OME_1 [25] [26]. The strengths of oxidising and acidic sites have to be balanced. Otherwise, unwanted side reactions will occur. Strong oxidising sites could over-oxidise methanol to CO_2, CO or formic acid. The latter can create methyl formate in the presence of methanol. Strong acidic sites could produce dimethyl ether by dehydration of methanol.

Potential catalysts are ruthenium- and rhenium-based, but also molybdenum- and vanadium-based. Rhenium-based catalysts (ReO_x) were the first reported catalysts to produce OME_1 via direct oxidation of methanol. The temperature required for this process is at least 240 to 300°C and the selectivity of OME_1 reached over 90% [21]. Vanadium and molybdenum oxides are good choices for catalysts since they are non-noble metals and could improve the sustainability of these processes. They also demonstrate better performance than Re-based catalysts. At only 140°C, the selectivity of OME_1 could reach over 90%. Another advantage is that vanadium-based catalysts are well established in industrial oxidation processes.

- **One-step synthesis of OME_1 via direct hydrogenation of CO_2**

Another newer approach to producing OME_1 is the direct hydrogenation of CO_2 with H_2 in the presence of methanol in one step only:

$$2CH_3OH + CO_2 + 2H_2 \rightarrow OME_1 + 2H_2O \quad (16)$$

The conventional process of creating OME_1 is redox-inefficient since it also contains an oxidative step (production of formaldehyde). The new approach is purely reductive.

Even though there are not many research reports on this method, Deutz et al. expected that this method would save energy and resources compared to recently mentioned methods, most importantly renewable hydrogen, which significantly impacts on the cost of power-to-fuel applications [20].

Thenert et al. in 2016 were the first to implement this type of reductive approach to produce OME_1. The multifunctional catalytic consists of a ruthenium catalyst for hydrogenation and an acidic co-catalyst, aluminium triflate ($Al(OTf)_3$), for activating the ruthenium catalyst and catalysing the esterification and acetalisation [23].

Klankermayer et al. in 2017 used cobalt salts together with triphos ligand and acid co-catalyst $HNTf_2$. The temperature during the reaction was 100°C, which is slightly higher than the one during the reaction with the ruthenium catalyst [27].

The advantage of using this type of synthesis is that, compared to conventional routes, one reactor less is required together with fewer heat exchangers and separation equipment if the synthesis system is optimised. Also, the size of the methanol plant can be reduced as well.

The direct route also operates with lesser exergy losses: according to one study [20] the direct route has an exergetic efficiency of 86%, while the conventional route has an exergetic efficiency of 74%. This is a significant advantage, and it means that hydrogen is more efficiently used as a feedstock to fuel production.

All of these advantages have a strong positive impact on the sustainability of OME_1 production.

3. Mathematical model

This section will provide an overview of all the fundamental equations of continuum mechanics based on mass, momentum, and energy conservation laws. It will also describe which models were used to describe the process of combustion and heat release.

Mass conservation equation

$$\frac{\partial \rho}{\partial t} + \frac{\partial}{\partial x_j}(\rho u_j) = 0 \tag{17}$$

The differential form of the mass conservation equation consists of 2 terms: the first describing local change over time and the second describing convective change due to occurring flow.

Momentum conservation equations

$$\frac{\partial}{\partial t}(\rho u_i) + \frac{\partial}{\partial x_j}(\rho u_i u_j) = \rho f_i + \frac{\partial \sigma_{ji}}{\partial x_j} \tag{18}$$

The differential form of the momentum conservation equation consists of 4 terms. The first term describes the rate of change of momentum. The second term describes the rate of momentum flux. The third and fourth terms describe the resulting volume and surface forces acting on the fluid.

Energy conservation equation

$$\frac{\partial}{\partial t}(\rho e) + \frac{\partial}{\partial x_j}(\rho e u_j) = \rho f_i u_i + S + \frac{\partial}{\partial x_j}(\sigma_{ji} u_i - q_j) \tag{19}$$

The energy conservation equation consists of 5 terms. The first term on the left side represents the rate of increase of total energy. The second term on the left side represents the total energy lost on the control volume boundaries. The first term on the right side represents the power by the volume forces. The second term represents the internal heat source due to radiation or chemical reactions. The last term represents the difference between the time rate of work done by the surface forces, and the heat flux vector.

Species mass conservation

$$\frac{\partial}{\partial t}(\rho Y_k) + \frac{\partial}{\partial x_j}(\rho Y_k u_j) = \frac{\partial}{\partial x_j}\left(\rho \gamma_k \frac{\partial Y_k}{\partial x_j}\right) + S_k \tag{20}$$

The equation describing the species mass conservation consists of 4 terms. The left two terms are analogous to the terms in the mass conservation equation. The terms on the right side are the diffusion term, modelled by Fick's law, and the source term.

Species transport

There are two different models to describe species transport [28]:

- General Species Transport Model
- Standard Species Transport Model

In the General Species Transport Model, each chemical species has its transport equation, which is needed to be solved (Eq. (20)). The model has a list of all possible reactions in the combustion process, including intermediary reactions.

For comparison, the Standard Species Transport Model (SST Model) has only one global reaction, which means there is no information on how other intermediate compounds are formed during combustion. The advantage to this model is the lower need for computational resources due to the reduced number of equations.

The SST Model uses dimensionless quantities to express the reactive system.

Mass fraction of fuel, y_{fu} is defined as:

$$y_{fu} = \frac{m_{fu,u}}{m_{mix}} \tag{21}$$

Where $m_{fu,u}$ is the mass of unburned fuel, while m_{mix} is the total mixture mass. Fuel mixture fraction is defined as:

$$f = \frac{m_{fu,u} + m_{fu,b}}{m_{mix}} \tag{22}$$

Where $m_{fu,b}$ is the mass of burned fuel. Residual gas (EGR) mass fraction is defined as:

$$g = \frac{m_{rg}}{m_{oxid}} \tag{23}$$

Where m_{rg} is the mass of residual gases and m_{oxid} is the oxidiser mass which is the sum of air and residual gases:

$$m_{oxid} = m_{air} + m_{rg} \tag{24}$$

In the model, three transport equations are solved, for fuel, fuel mixture fraction and residual gas mass fraction:

$$\frac{\partial}{\partial t}(\rho y_{fu}) + \frac{\partial}{\partial x_i}(\rho y_{fu} u_i) = \frac{\partial}{\partial x_i}\left(\Gamma_{fu}\frac{\partial y_{fu}}{\partial x_i}\right) + S_{fu} \tag{25}$$

$$\frac{\partial}{\partial t}(\rho f) + \frac{\partial}{\partial x_i}(\rho f u_i) = \frac{\partial}{\partial x_i}\left(\Gamma_{f}\frac{\partial f}{\partial x_i}\right) \tag{26}$$

$$\frac{\partial}{\partial t}(\rho g) + \frac{\partial}{\partial x_i}(\rho g u_i) = \frac{\partial}{\partial x_i}\left(\Gamma_{g}\frac{\partial g}{\partial x_i}\right) \tag{27}$$

The system consists of fuel $C_nH_mO_k$, O_2, CO_2, H_2O and N_2.

Turbulence model – k-zeta-f

This model, along with the k-ε model, is one of the more often used models for solving turbulence in CFD. The model aims to improve the numerical stability of the original $\overline{v^2} - f$ model by solving a transport equation for the velocity scale ratio $\zeta = \overline{v^2}/k$ instead of the velocity scale $\overline{v^2}$.

The eddy viscosity is obtained from:

$$\nu_t = C_\mu \zeta \frac{k^2}{\varepsilon} \tag{28}$$

Where C_μ is model constant, ζ is velocity scale ratio, k is turbulent kinetic energy and ε is the rate of turbulent energy dissipation.

The main transport equations are [29]:

$$\rho\frac{Dk}{Dt} = \rho(P_k - \varepsilon) + \frac{\partial}{\partial x_j}\left[\left(\mu + \frac{\mu_t}{\sigma_k}\right)\frac{\partial k}{\partial x_j}\right] \tag{29}$$

$$\rho\frac{D\varepsilon}{Dt} = \rho\frac{(C^*_{\varepsilon 1}P_k - C_{\varepsilon 2}\varepsilon)}{T} + \frac{\partial}{\partial x_j}\left[\left(\mu + \frac{\mu_t}{\sigma_k}\right)\frac{\partial \varepsilon}{\partial x_j}\right] \tag{30}$$

$$\rho\frac{D\zeta}{Dt} = \rho f - \rho\frac{\zeta}{k}P_k + \frac{\partial}{\partial x_j}\left[\left(\mu + \frac{\mu_t}{\sigma_\zeta}\right)\frac{\partial \zeta}{\partial x_j}\right] \tag{31}$$

Where f can be written as:

$$f - L^2 \frac{\partial^2 f}{\partial x_j \partial x_j} = \left(C_1 + C_2 \frac{P_k}{\varepsilon}\right) \frac{(2/3 - \zeta)}{T} \tag{32}$$

Turbulent time scale and length scale are given by:

$$T = \max\left(\min\left(\frac{k}{\varepsilon}, \frac{a}{\sqrt{6} C_\mu |S| \zeta}\right), C_T \left(\frac{\upsilon}{\varepsilon}\right)^{1/2}\right) \tag{33}$$

$$L = C_L \max\left(\min\left(\frac{k^{3/2}}{\varepsilon}, \frac{k^{1/2}}{\sqrt{6} C_\mu |S| \zeta}\right), C_\eta \frac{\upsilon^{3/4}}{\varepsilon^{1/4}}\right) \tag{34}$$

Spray model

Spray models are crucial to accurately describe the ignition and combustion processes happening inside the IC engine. Spray simulations describe the multi-phase flow phenomena and require solving conservation equations for both the gas and liquid phase. The most common method used is the Discrete Droplet Method (DDM). This method approximates spray droplets as groups of droplets (parcels) that exhibit the same properties. The Lagrangian approach is used for the liquid phase, while the Eulerian approach is used for the gas phase. The atomisation process of sprays is described with various sub-models.

The most essential sub-models used in this simulation are:

- Break-up model
- Evaporation model
- Turbulence dispersion model
- Drag law model
- Wall interaction model

Break-up model

In the WAVE break-up model, the growth of an initial perturbation on a liquid surface is linked to its wavelength and to other physical and dynamic parameters of the injected fuel and the domain fluid.

There are two break-up regimes: low-velocity Rayleigh and high-velocity Kevin-Helmholtz. The Rayleigh regime is not representative of high-pressure injection systems, so it will not be used.

The radius reduction ratio of the drops is defined as:

$$\frac{dr}{dt} = -\frac{(r - r_{stable})}{\tau_a} \tag{35}$$

where τ_a is the break-up time of the model:

$$\tau_a = \frac{3{,}726 C_2 r}{\Lambda\Omega} \tag{36}$$

The constant C_2 corrects the characteristic break-up time and varies from one injector to another. The lower and upper-value limits for C_2 are 1 and 100, respectively.

$$r_{stable} = C_1 * \Lambda \tag{37}$$

The product droplet radius is defined as a product of a constant C_1 and the wavelength of the fastest growing wave on the parcel surface. The recommended value of C_1 is 0,61. The wave length Λ and wave growth rate Ω depend on the local flow properties. [30]

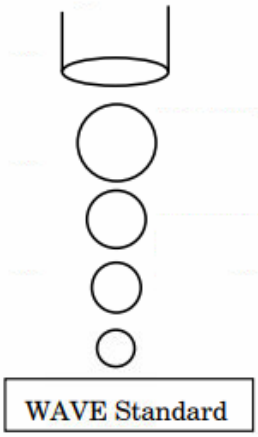

Figure 8 *Process of droplet forming in the WAVE break-up model* [30]

Evaporation model

The heat and mass transfer processes in the Dukowicz evaporation model are based on the following assumptions [30]:

- The spherical symmetry of droplets
- Quasi-steady gas film around the droplet
- Uniform droplet temperature along the drop diameter
- Uniform physical properties of the surrounding fluid
- Liquid-vapour thermal equilibrium on the droplet surface

The temperature of the droplet is defined with the following equation, which states that energy conducted to the droplet either heats the droplet or supplies heat for vaporisation:

$$m_d c_{pd} \frac{dT_d}{dt} = L \frac{dm_d}{dt} + \dot{Q} \tag{38}$$

The convective heat flux between the gas and liquid phase is described with the following equation:

$$\dot{Q} = \alpha A_s (T_\infty - T_s) \tag{39}$$

If the convective heat transfer coefficient is replaced with the Nusselt number, the heat flux can be written as:

$$\dot{Q} = D_d \pi \lambda Nu (T_\infty - T_s) \tag{40}$$

The Nusselt number is obtained from the correlation proposed by Ranz and Marshall [30]:

$$Nu = 2 + 0{,}6 Re_d^{1/2} Pr^{1/3} \tag{41}$$

Turbulence dispersion model

Individual turbulent eddies influence the behaviour of particles passing through the flow, where their interaction deflects individual particles regarding the instantaneous velocity of the turbulent eddy and the particle inertia. A turbulent dispersion model is used to describe the turbulence effects on the spray particles.

The interaction time of a particle with the individual eddies is estimated from two criteria, the turbulent eddy lifetime and the time required for a particle to cross the eddy. The turbulence correlation time t_{turb} is the minimum of the eddy break-up time t_e and the time for the droplet to pass through the observed eddy t_{tr}, and is given by:

$$t_{turb} = \min(t_e, t_{tr}) \tag{42}$$

$$t_{turb} = \min\left(C_\tau \frac{k}{\varepsilon}, C_1 \frac{k^{\frac{3}{2}}}{\varepsilon} \frac{1}{|u_g + u' - u_d|} \right) \tag{43}$$

Where $C_\tau = 1$ and $C_1 = 0{,}16432$ are model constants. The fluctuation velocity u' is randomly determined from a Gaussian distribution.

In the case when the computational time step is larger than the turbulence correlation time, the spray integration time step will be reduced to t_{turb}.

Drag law model

The drag model from Shiller – Naumann is used to calculating the drag from the gas phase on the droplets. In most applications, it will give good results.

The drag coefficient is calculated by [30]:

$$C_D = \begin{cases} 24\dfrac{1+0{,}15Re^{0.687}}{Re}; & Re \leq 1000 \\ 0{,}44\ ; & Re \geq 1000 \end{cases} \tag{44}$$

The drag force is calculated by:

$$F_{di} = 0{,}5\pi r^2 \rho C_D u_i^2 \tag{45}$$

Wall interaction model

The behaviour of a droplet at wall interaction depends on several parameters like droplet velocity, diameter, droplet properties, wall surface roughness and wall temperature. At very low inlet velocities, the droplet sticks to the wall or the wall film. With the increase of inlet velocity, a vapour or gas boundary layer is trapped underneath the droplet, which causes the droplet to rebound. With an even higher increase of velocity, the drop enters the spread or the splash regime. In the spreading regime, the complete liquid spreads along the wall with hardly any normal velocity. In the splash regime, a part of the liquid remains near the surface, and the rest of it is reflected and broken up into secondary droplets.

In all of the simulations, the wall interaction model Walljet 1 is used. In this model, it is assumed that a droplet that hits a wall either rebounds or reflects in the form of a liquid jet. Wall film physics is not taken into account. The droplet diameter after impingement is calculated as a function of the Weber number [30].

Combustion modelling

Combustion modelling can be done in two different ways: using a chemical mechanism or employing a combustion model.

When using a chemical mechanism, all chemical species have their related chemical reactions. The reaction rates are calculated in the general form [31]:

$$\sum_{k=1}^{K} \nu'_{ki} \kappa_k \Leftrightarrow \sum_{k=1}^{K} \nu''_{ki} \kappa_k \ \ (i = 1, \dots, I) \tag{46}$$

Where ν are stoichiometric coefficients of the reactants and products and κ is the chemical symbol for the species k.

The stoichiometric coefficient of species k in reaction i is defined as:

$$\nu_{ki} = \nu'_{ki} - \nu''_{ki} \tag{47}$$

The rate of production of species k ($\dot{r}_k$) is defined as:

$$\dot{r}_k = \sum_{i=1}^{I} \nu_{ki}\, \dot{q}_i \tag{48}$$

while the reaction rate $\dot{q}_i$ of reaction is defined by the difference of forward and backward reaction rates:

$$\dot{q}_i = k_{f_i} \prod_{k=1}^{K} [c_{k,g}]^{\nu'_{ki}} - k_{r_i} \prod_{k=1}^{K} [c_{k,g}]^{\nu''_{ki}} \tag{49}$$

Where $c_{k,g}$ is the molar concentration of species k.

The source term S_K from the equation describing the species mass conservation can be modelled according to the Arrhenius law:

$$k = AT^{\beta} \exp\left(-\frac{E}{RT}\right) \tag{50}$$

Where k is the global reaction rate coefficient, and E represents activation energy. The coefficients A, β and E are determined from experimental data. The coefficients A, β and E are the pre-exponential factor, temperature dependence factor and activation energy. In this approach, the burning rate strongly depends on the chemical kinetics while turbulent fluctuations are ignored.

The source term can be defined as:

$$S_K = \dot{r}_k M_k \tag{51}$$

Where the rate of production of species k ($\dot{r}_k$) is defined in Eq. (48).

Coherent flame model – ECFM-3Z

An alternative to modelling combustion via chemical kinetics is using a coherent flame model suitable for simulating combustion inside Diesel engines. One of the models used is the ECFM-3Z model. It has a decoupled treatment of chemistry and turbulence. [32]

In the model, the following equation is solved for the flame surface density Σ:

$$\frac{\partial \Sigma}{\partial t} + \frac{\partial}{\partial x_j}\left(\bar{u}_j \Sigma\right) - \frac{\partial}{\partial x_j}\left(\frac{\nu_t}{\sigma_\Sigma}\frac{\partial \Sigma}{\partial x_j}\right) = S_\Sigma \tag{52}$$

In the model, transport equations for the following species are solved: O_2, N_2, NO, CO_2, CO, H_2, H_2O, O, H, N, OH:

$$\frac{\partial \bar{\rho}\tilde{Y}_X}{\partial t} + \frac{\partial \bar{\rho}\tilde{u}_i\tilde{Y}_X}{\partial x_i} = \frac{\partial}{\partial x_i}\left(\left(\frac{\mu}{Sc} + \frac{\mu_t}{Sc_t}\right)\frac{\partial \tilde{Y}_X}{\partial x_i}\right) + \overline{\dot{\omega}}_X \tag{53}$$

Where $\overline{\dot{\omega}}_X$ is the average combustion source term and $\tilde{Y}_X$ is the average mass fraction of species X.

The fuel is divided into two parts: the unburned ($\tilde{Y}_{Fu}^u$) and burned ($\tilde{Y}_{Fu}^b$) fuel. For both of them, additional transport equations are solved:

$$\frac{\partial \bar{\rho}\tilde{Y}_{Fu}^u}{\partial t} + \frac{\partial \bar{\rho}\tilde{u}_i\tilde{Y}_{Fu}^u}{\partial x_i} = \frac{\partial}{\partial x_i}\left(\left(\frac{\mu}{Sc} + \frac{\mu_t}{Sc_t}\right)\frac{\partial \tilde{Y}_{Fu}^u}{\partial x_i}\right) + \bar{\rho}\tilde{\dot{S}}_{Fu}^u + \overline{\dot{\omega}}_{Fu}^u - \overline{\dot{\omega}}_{Fu}^{u\to b} \tag{54}$$

$$\frac{\partial \bar{\rho}\tilde{Y}_{Fu}^b}{\partial t} + \frac{\partial \bar{\rho}\tilde{u}_i\tilde{Y}_{Fu}^b}{\partial x_i} = \frac{\partial}{\partial x_i}\left(\left(\frac{\mu}{Sc} + \frac{\mu_t}{Sc_t}\right)\frac{\partial \tilde{Y}_{Fu}^b}{\partial x_i}\right) + \bar{\rho}\tilde{\dot{S}}_{Fu}^b + \overline{\dot{\omega}}_{Fu}^b + \overline{\dot{\omega}}_{Fu}^{u\to b} \tag{55}$$

Where $\tilde{\dot{S}}_{Fu}^u$ is a source term representing fuel evaporation. $\overline{\dot{\omega}}_{Fu}^u$ and $\overline{\dot{\omega}}_{Fu}^b$ represent oxidation of (un)burned fuel, while $\overline{\dot{\omega}}_{Fu}^{u\to b}$ represents fuel mass transfers between various zones.

The combustion area can be divided into three zones: a pure fuel zone, a pure air plus possible EGR zone, and mixed air and fuel zone. The model describes autoignition and premixed and diffusion flames. A schematic showing these zones is shown in Figure 9. [33]

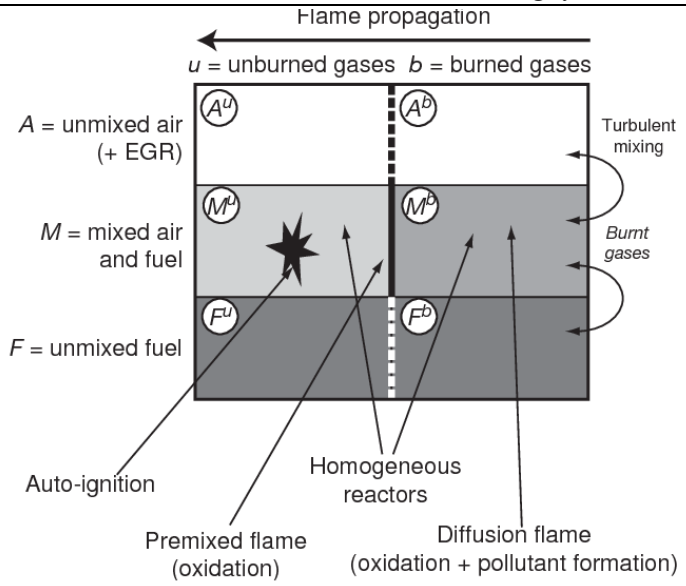

Figure 9 *Schematic of the ECFM-3Z model cell* [33]

NO formation model

There are three main mechanisms of nitric oxides (NO) formation that form during combustion [34]:

- Thermal NO – formed due to dissociation of the molecular air-nitrogen
- Prompt NO – formed during the hydrocarbon combustion at the flame front
- Fuel NO – formed from nitrogen-containing components in the fuel

In general, the most significant source of NO in ICE is Thermal NO, with Prompt NO and Fuel NO being almost negligible.

One of the most widely used models to describe NO formation at high temperatures is the extended Zeldovich mechanism:

$$N_2 + O \overset{k_1}{\leftrightarrow} N + NO \tag{56}$$

$$N + O_2 \overset{k_2}{\leftrightarrow} O + NO \tag{57}$$

$$N + OH \overset{k_3}{\leftrightarrow} H + NO \tag{58}$$

where k_1, k_2, k_3 are forward and backward reaction rates. The extended Zeldovich mechanism considers the effect of oxygen, nitrogen and hydrogen radicals on NO formation. It is worth noting that all three reactions exhibit a strong temperature dependency.

The change of NO concentration over time is given by:

$$\frac{dc_{NO}}{dt} = k_{1f}c_O c_{N_2} + k_{2f}c_N c_{O_2} + k_{3f}c_N c_{OH} - k_{1b}c_{NO}c_N - k_{2b}c_{NO}c_O - k_{3b}c_{NO}c_H \quad (59)$$

An expanded version of the mechanism is used in the simulations using ECFM-3Z: Extended Zeldovich. However, in those simulations, only the Thermal and Prompt NO models were used. For n-heptane, the LLNL NO mechanism was used as a part of the reduced n-heptane mechanism. The same NO mechanism was incorporated in Lin et al. mechanism since it does not contain an NO formation mechanism on its own.

The Extended Zeldovich is defined according to the chemical equilibrium assumption, and only atomic nitrogen (N) is needed as an additional intermediate species. Its concentration does not depend on the chemical kinetics of the combustion of the mixture. Hence there is no need to follow fuel oxidation in-depth but instead only several reactions.

The overall NO formation rate is given by:

$$\frac{dc_{NO}}{dt} = 2k_{1f}c_O c_{N_2} \frac{\left(1 - \frac{k_{1b}k_{2b}c_{NO}^2}{k_{1f}c_{N_2}k_{2f}c_{O_2}}\right)}{1 + \frac{k_{1b}c_{NO}}{k_{2f}c_{O_2} + k_{3f}c_{OH}}} \quad (60)$$

4. Numerical setup

In this chapter, all the details regarding the mesh, time step discretisation, boundary and initial conditions, spray setup and injection rates, and the combustion model parameters are shown. The engine and injector data are shown in Table 2:

Table 2 *Engine and injector specifications*

Engine data	
Bore	81 mm
Stroke	93,15 mm
Connecting rod length	147 mm
Compression ratio	16,5 : 1
Displacement	2,4 l
Number of cylinders	5
Injector data	
Number of nozzle holes	7
Spray cone angle	145°
Flow rate (at 100 bar Δp)	440 ml / 30 s
The shape of nozzle dome	Micro Sac

4.1. Mesh

The moving mesh was generated in dedicated software by AVL, FIRE™ ESE Diesel. The mesh contains two boundary layers that encompass the combustion chamber, including the compensation volume at the piston rim.

The cells tend to be more uniform and keep a rectangular shape where possible. The mesh passes all quality checks and shows no negative volumes or non-orthogonal cells. The large majority of cells are hexahedrons.

Figure 10 and Figure 11 show how the final numerical mesh looks like at TDC and BDC.

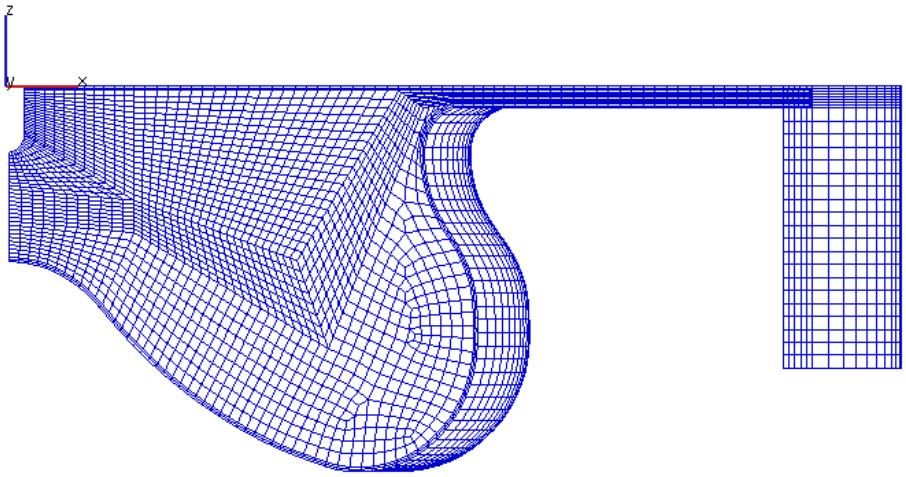

Figure 10 *The mesh at Top Dead Centre (TDC)*

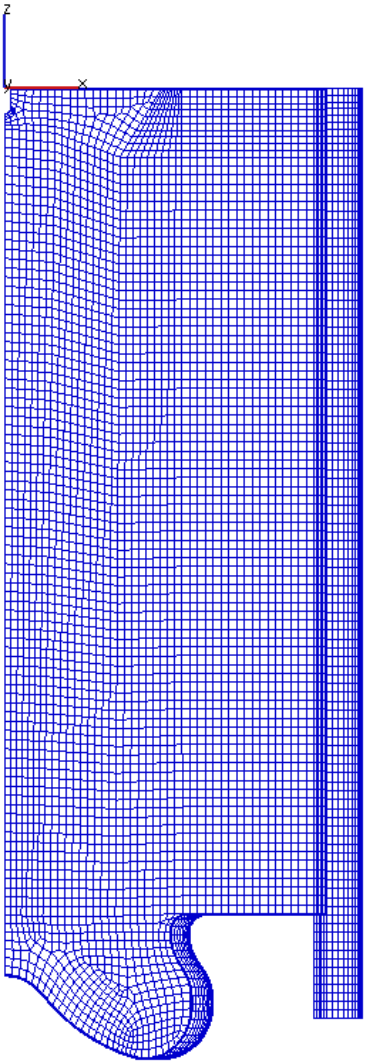

Figure 11 *The mesh at Bottom Dead Centre (BDC)*

Mesh details, like volume and number of cells are given in Table 3:

Table 3 *Mesh details*

	TDC	BDC
Volume	4,6719 cm^3	75,88 cm^3
Number of cells	54 663	112 854
Compression ratio	16,24	

4.2. Simulation run time

The simulation run time was set from 585 °CA to 855 °CA, during which the intake and exhaust valves were closed. In this period, the processes of compression, injection of fuel, combustion and expansion are covered. As shown in Table 4, during fuel injection, the time step is smaller to capture the spray phenomena more accurate and achieve more stable simulations.

Table 4 *Time step discretization*

Crank angle [°CA]	Time step [°CA]
585 – 700	1
700 – 760	0,2
760 – 800	0,5
800 – 855	1

4.3. Boundary conditions

Boundary conditions were defined via the boundary face selections shown in Figure 12 and listed in Table 5. For the piston, liner and cylinder head boundary conditions with constant temperature were used. The mesh covers only the volume around one nozzle hole to save computing power. As mentioned before, the injector contains seven nozzle holes, hence, the mesh covers 1/7 of the total cylinder volume. For the axis, the symmetry boundary condition is used, and for the segment, the inlet/outlet condition is used.

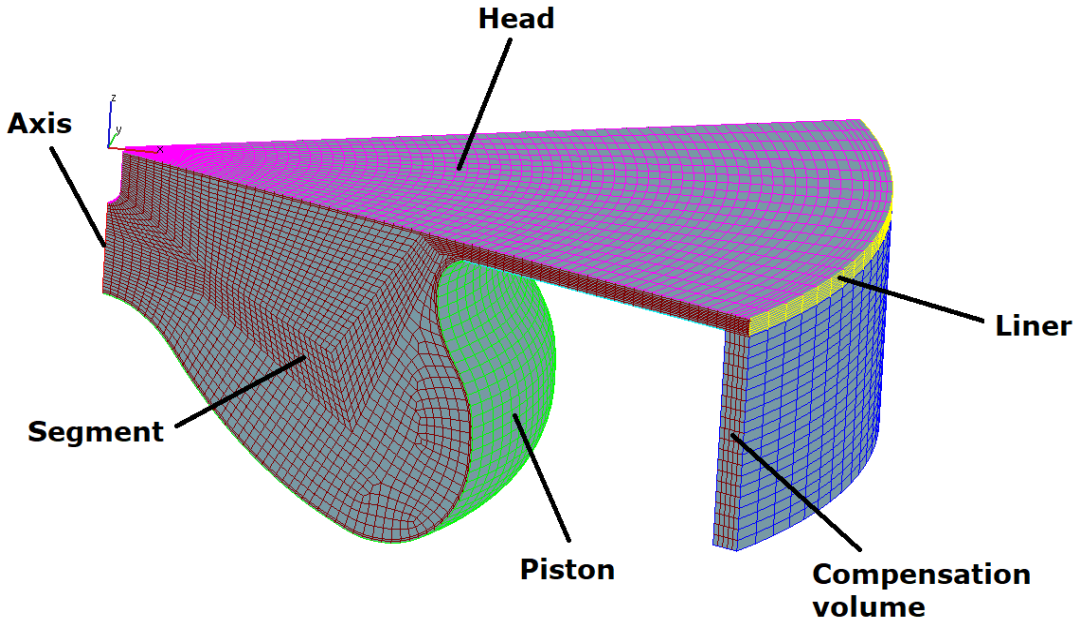

Figure 12 *Boundary selections of the computational mesh*

Table 5 *Boundary conditions for the cases*

Face	Boundary Condition
Piston	Type: Wall Temperature: 473 K
Liner	Type: Wall Temperature: 423 K
Axis	Type: Symmetry
Segment	Type: Inlet/Outlet
Compensation volume	Type: Wall, Mesh movement
Head	Type: Wall Temperature: 443 K

4.4. Initial conditions

Initial conditions were set separately for both of the cases which were simulated. The initial pressure, temperature and swirl of the gases inside the cylinder are shown in Table 6.

***Table 6** Initial conditions for the cases*

	Case A	Case B
Pressure	218500 Pa	192800 Pa
Temperature	365 K	396 K
Swirl	4740 1/min	4740 1/min

The initial mass composition of the gases inside the cylinder is defined in two ways since both the chemical mechanism and a combustion model were used in the simulations.

When the chemical mechanism was employed, the mass composition of gases was defined directly, as shown in Table 7.

***Table 7** Mass composition (chemical mechanism)*

Mass composition	Case A	Case B
O_2	22,80 %	20,38 %
N_2	76,72 %	76,22 %
CO_2	0,33 %	2,32 %
H_2O	0,15 %	1,08 %

The same values were plotted in Figure 13. In case A, it could be said that the only components are oxygen and nitrogen since CO_2 and water vapour make up for less than 0,5% in the mixture. In other words, there is no exhaust gas recirculation (EGR) at the start of the case. For case B, CO_2 and water make up a bit higher share in the mix, with 2% and 1%, respectively.

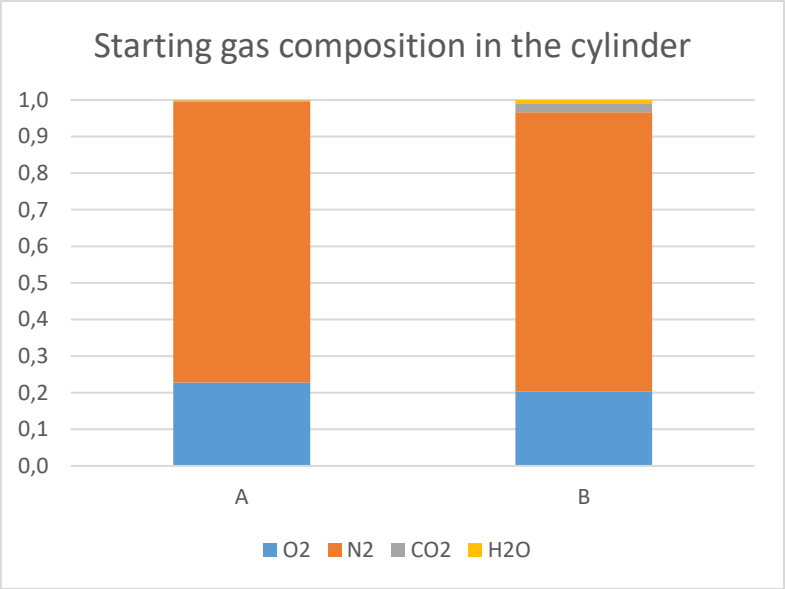

Figure 13 *Initial mass composition*

When the combustion model was used, the mass composition of gases was defined indirectly via the EGR mass fraction and composition. The values for these two parameters are given in Table 8. The resulting composition of gases was set to have the same amount of oxygen in the cylinder.

Table 8 *EGR parameters for ECFM-3Z model*

	Case A	Case B
EGR mass fraction	0,01745	0,122469
EGR composition	0,97	0,99

4.5. Spray setup

The spray module was used to modify all the parameters needed for the simulation of the spray. Since the observed OME-3 fuel is not contained in the current AVL FIRE™ version, a database with OME-3 liquid properties was provided as an object file from the internal project at AVL AST GmbH company. A database contains info about the physical and thermodynamic properties of the liquid phase of the fuel. The temperature of the injected fuel is constant for all cases and is equal to 317.11 K. A comprehensive list of all the sub-models used is shown in Table 9.

Table 9 *Spray sub-models*

Drag law model	Schiller Naumann
Turbulent dispersion model	Enable
Particle interaction model	Disable
Wall interaction model	Walljet1
Evaporation model	Dukowicz E_1=1 E_2=1
Break-up model	Wave C_1=0,61 C_2=18 C_3=1 C_4=0.1 C_5=0.3 C_6=C_7=C_8=0

In Table 10, additional details about particle introduction are defined as the size and number of particles.

Table 10 *Particle introduction from a nozzle*

Number of different particle sizes introduced per time step and ring	3
Number of radial parcels release locations on each injection hole	6
Number of circular parcels release locations on each ring	6

Additional data about the injector, nozzle hole and droplet sizes were given in Table 11 and Table 12. The spray angle delta 1 is the angle of spray between two opposite nozzle holes. There is also an assumption that particles exiting the nozzle hole will have the same size as the nozzle hole diameter.

Table 11 *Nozzle geometry data*

Nozzle position (X, Y, Z coordinate)	(0 , 0 , 1,5) mm
Nozzle direction (X, Y, Z)	(0, 0, 1)
Nozzle diameter at hole centre position	1,84 mm
Number of simulated nozzle holes	1
Spray angle delta 1	145 °

Table 12 *Droplet data*

Outer diameter	0,125 mm
Particle sizes	0,125 mm
Half outer cone angle	8

Injection rates

Three injection regimes were implemented to evaluate how OME-3 fuel behaves in current diesel engines and similar combustion conditions. The first one is identical to the injection regime with n-heptane, where the same mass of OME-3 is injected as in the experiment with n-heptane. The second regime features more injected mass to match the released energy of n-heptane, which implies an extended period of fuel injection. The third regime is almost identical to the second one in terms of injection duration, while the start and end of injection were changed, which is most noticeable in the multi injection case.

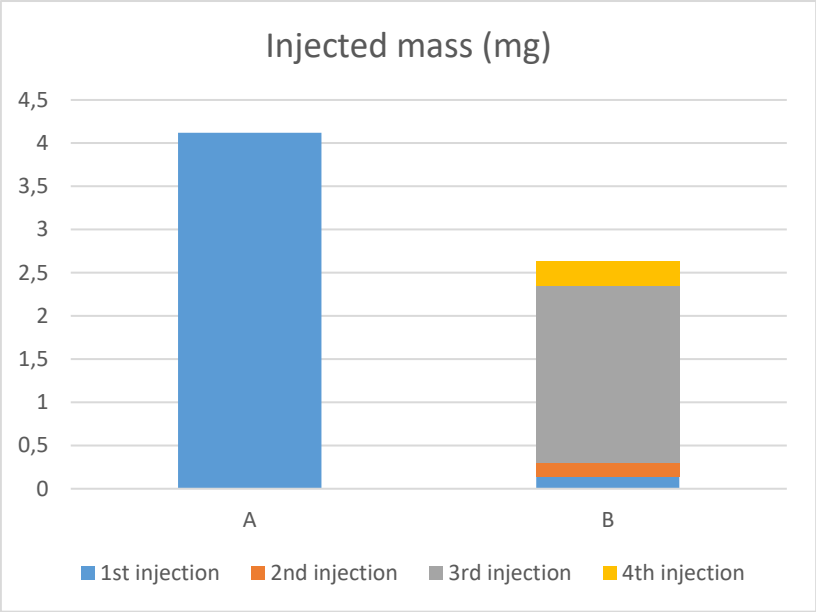

***Figure 14** Injected mass*

Figure 14 shows how much fuel is injected inside the cylinder. Case A is a single injection case, while case B is a multi injection case, meaning fuel is injected in different stages. Case B features four separate injections, where the 3rd stage making up for most fuel injection and is called the main injection. The following two figures show the dynamic of fuel injection when the injections are taking place and at what intensity. These were used to validate the cases, using n-heptane as the fuel, with the experimental data.

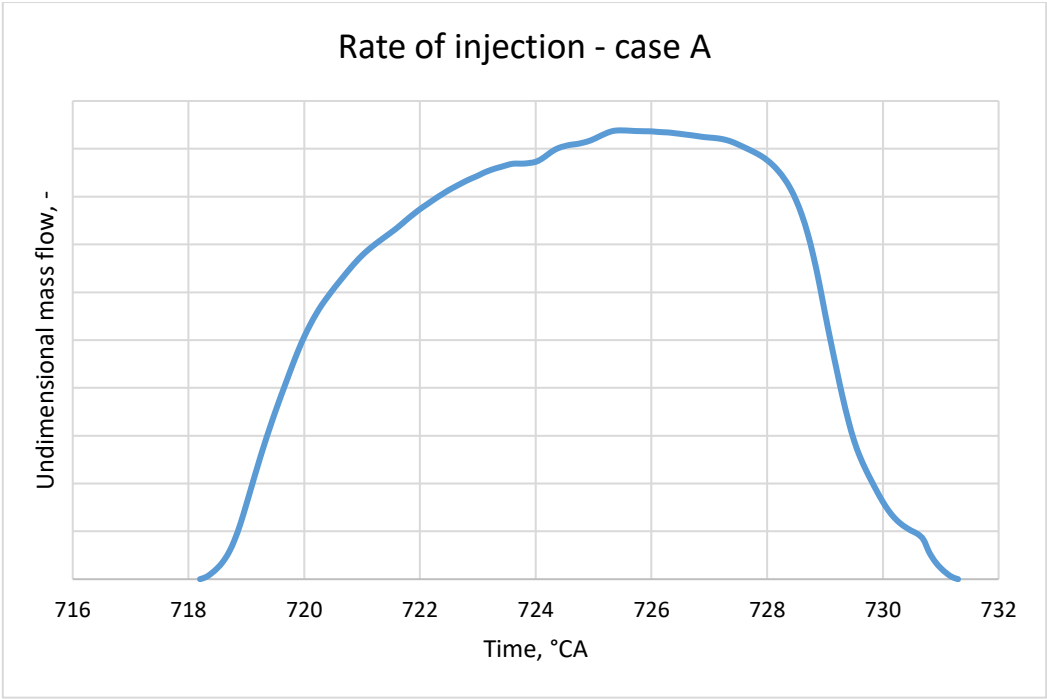

***Figure 15** Rate of injection – case A*

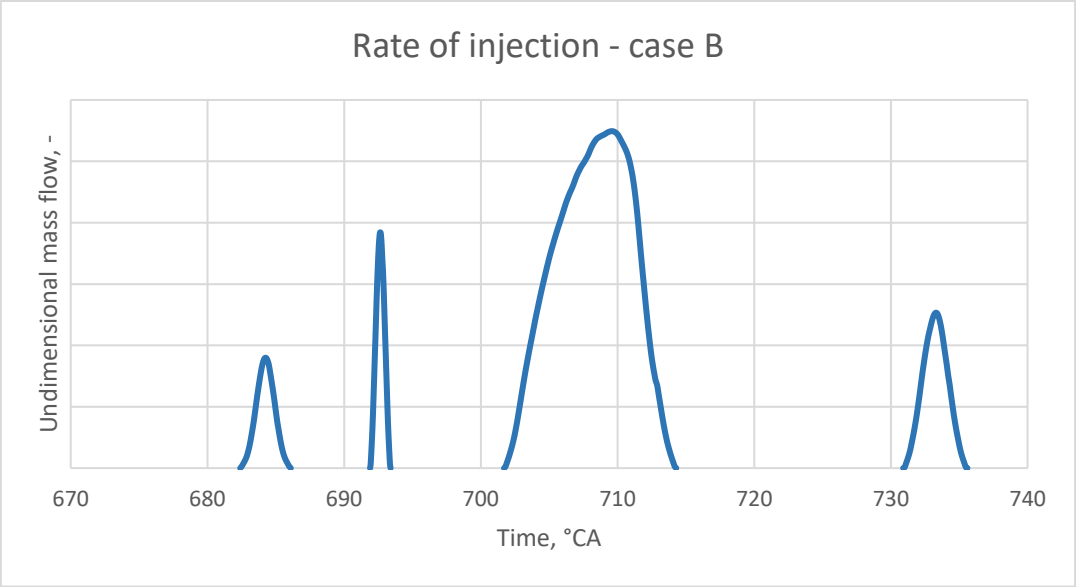

Figure 16 *Rate of injection – case B*

The above injection profiles are scaled to the injected mass, so the area under the injection curve corresponds to the amount of injected fuel.

Three different injection regimes were applied to see how the different fuel affects the resulting pressure, mean temperature, and rate of heat release (RoHR). The first injection regime is used in the simulation with n-heptane. It serves as a preliminary analysis to see how different properties of the fuel affect the combustion dynamic. In the second injection regime, more fuel is injected, and the injection process lasts longer. More fuel is injected since OME-3 has a lower LHV than n-heptane and the overall released energy in the first injection regime is higher for n-heptane than for OME-3. To compensate for this and have two comparable cases regarding power, pressure, and RoHR, more mass is injected in the second injection regime. The injected mass and the second injection regime were calibrated to ensure that the overall released energy in that regime is almost the same as in the experiment. In the third injection regime, the amount of injected mass was the same as in the second injection regime. Therefore the individual injection profiles are the same, while the injection timing is changed to attempt to match the experimental data more accurately in terms of primary pressure and the start of rate of heat release.

The amount of fuel injected in the second and third regime is shown in Figure 17.

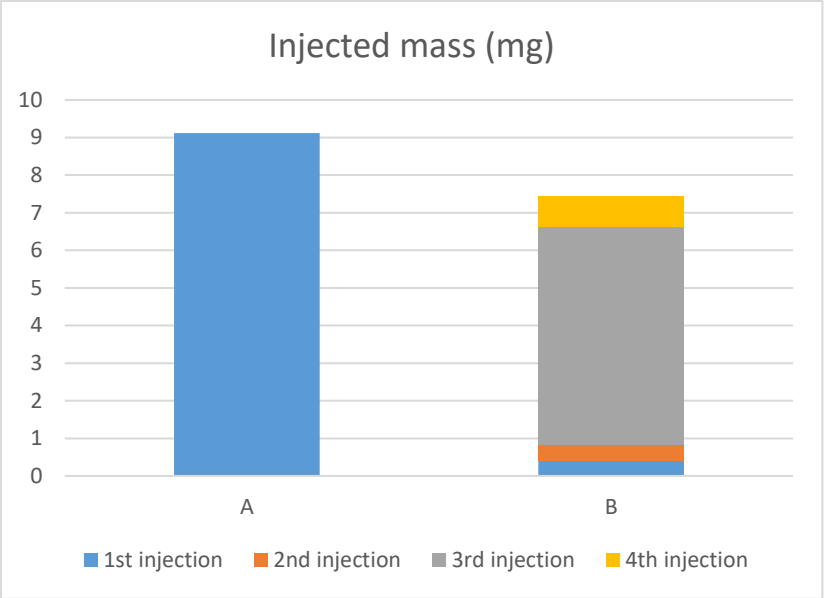

Figure 17 *Injected mass – second and third regime*

When comparing the injected mass between the second regime and the first regime, significantly more fuel is needed to ensure that the same amount of energy is released, more than twice as much. The increase in mass is minor for the single injection case than the multi injection case, which may mean that OME-3 fuel is best implemented in single injection regimes.

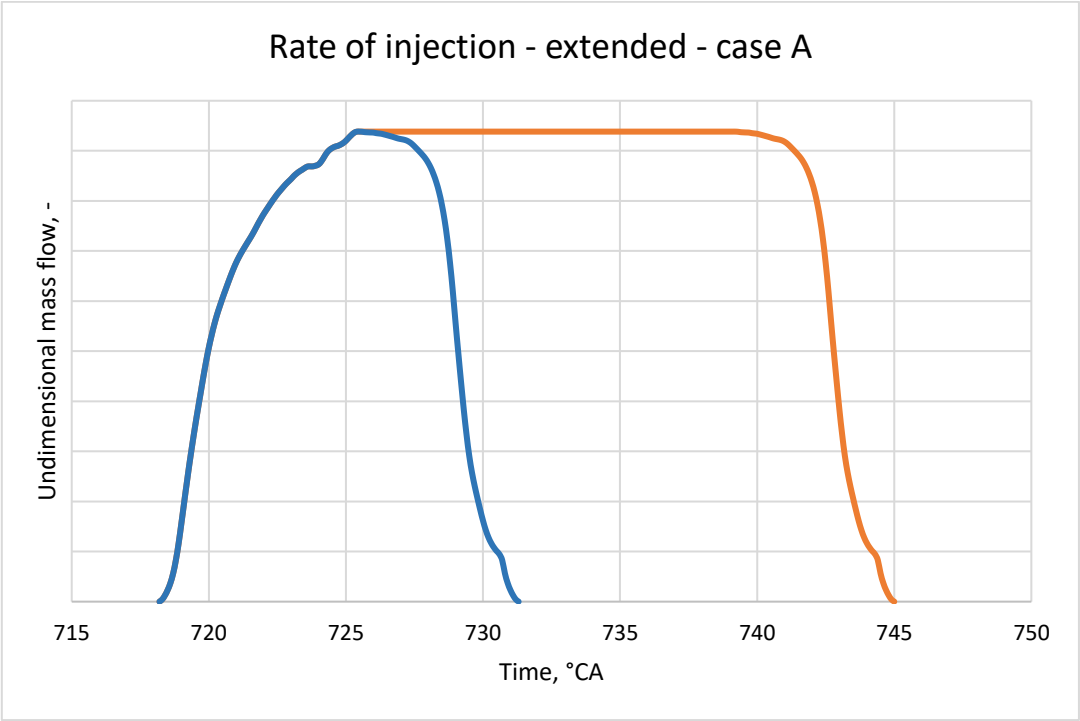

Figure 18 *Rate of injection – comparison – case A*

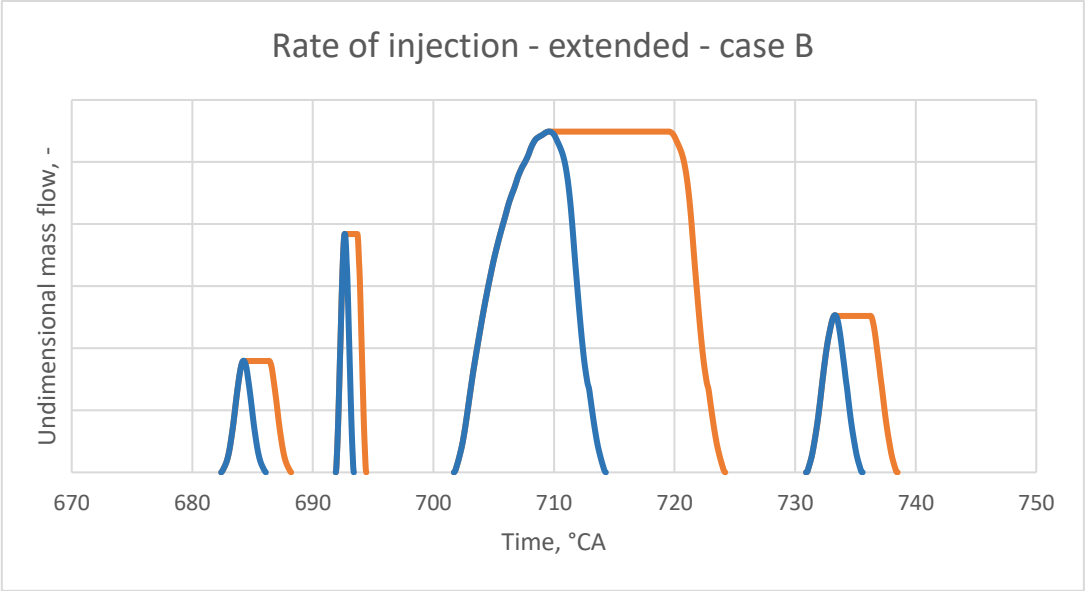

Figure 19 *Rate of injection – comparison – case B*

The two above figures show a comparison of both injection regimes for both cases. The second regime was created based on the first regime. The idea was that the start and end of the injection remain the same, while the only difference was the prolongation of the maximum injection rate.

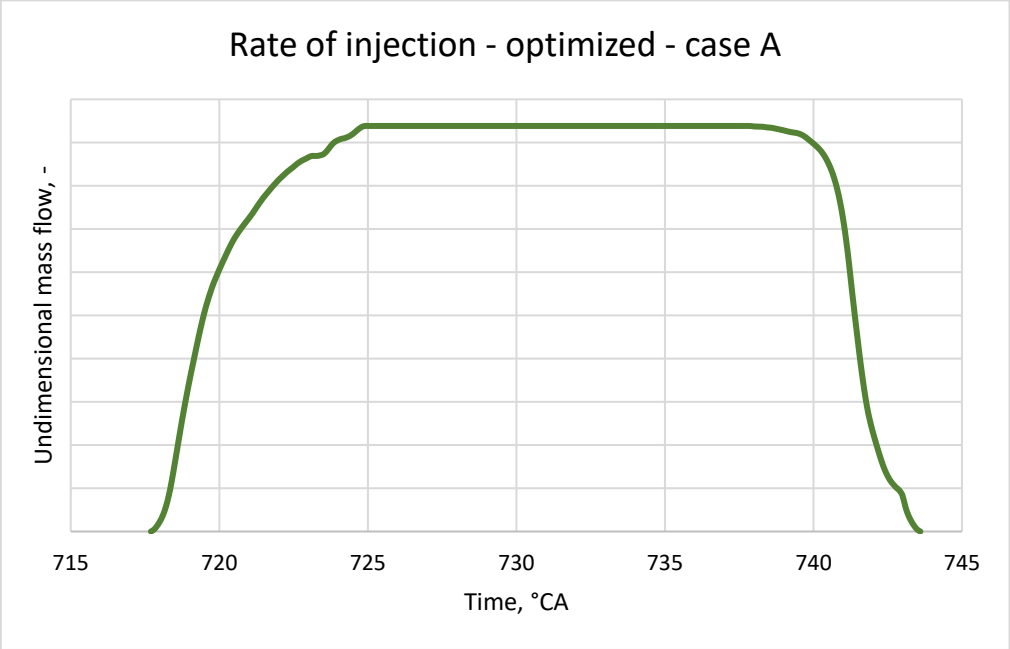

Figure 20 *Rate of injection – optimised – case A*

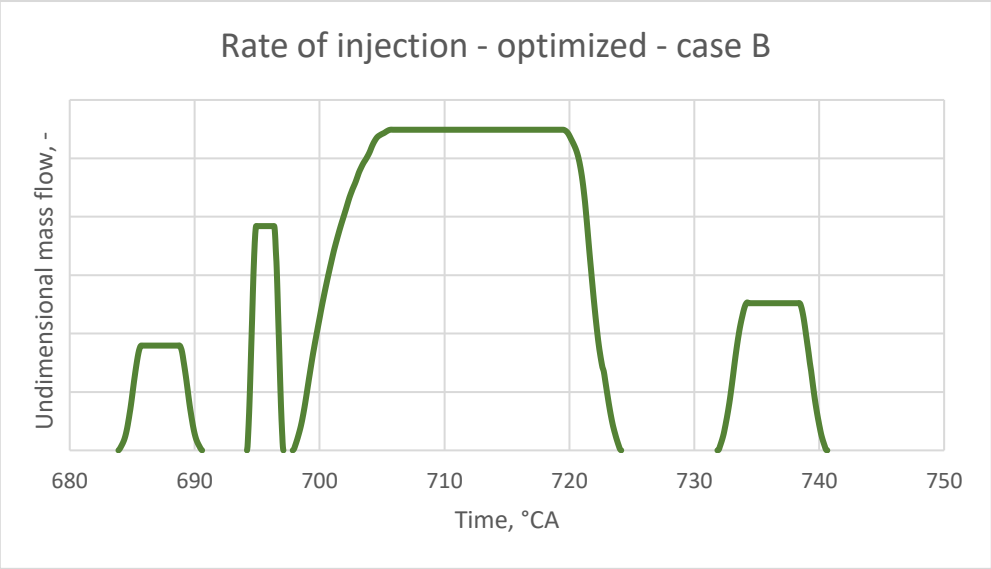

Figure 21 *Rate of injection – optimised – case B*

In case A, when injected mass is increased, the injection regime is quite similar to the optimised injection regime since there was no need for considerable optimisation and significant change at the start of injection. In case B, the difference is more pronounced, and it can be noticed that the second injection of fuel ends almost as the third injection is starting. Overall, the start of injection occurs later than before.

4.6. Combustion model parameters

For the cases where a combustion model was used instead of a chemical mechanism, Table 13 shows all the combustion model parameters used. The combustion model which was used is ECFM-3Z. The mixing model parameter describes the transfer of fuel from the pure fuel zone to the mixed zone, while the autoignition model parameter and chemical reaction time influence the acceleration of ignition or the rate of reaction.

Table 13 *Combustion model parameters*

	Case A	Case B
Mixing model parameter	50	90
Auto ignition model	Two-Stage	Two-Stage
Autoignition model parameter	1000	100
Chemical reaction time	10 s	5 s
Extinction temperature	200 K	1500 K

5. Results

5.1. Validation of the mesh

The first step in this project was to validate the meshes and used models by comparing the simulation results with the experimental data. The fuel used in the simulation and experiment is n-heptane. For all cases, pressure, mean temperature, and rate of heat release (RoHR) were compared to see how much the results from the simulation match with experimental data.

5.1.1. Single injection case – case A

The pressure curve shows a good match between experimental and simulation data. A slight delay before ignition and pressure rise is observed in the simulation pressure curve, which is slightly higher than the experimental data.

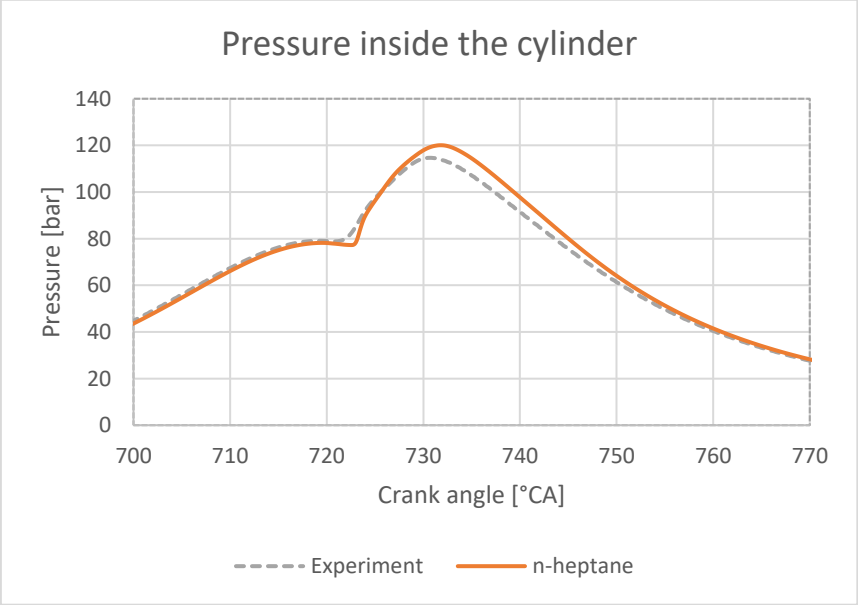

Figure 22 *Pressure inside the cylinder – case A*

Similarly to the pressure curve, the maximum temperature is higher for the simulation than in the experiment.

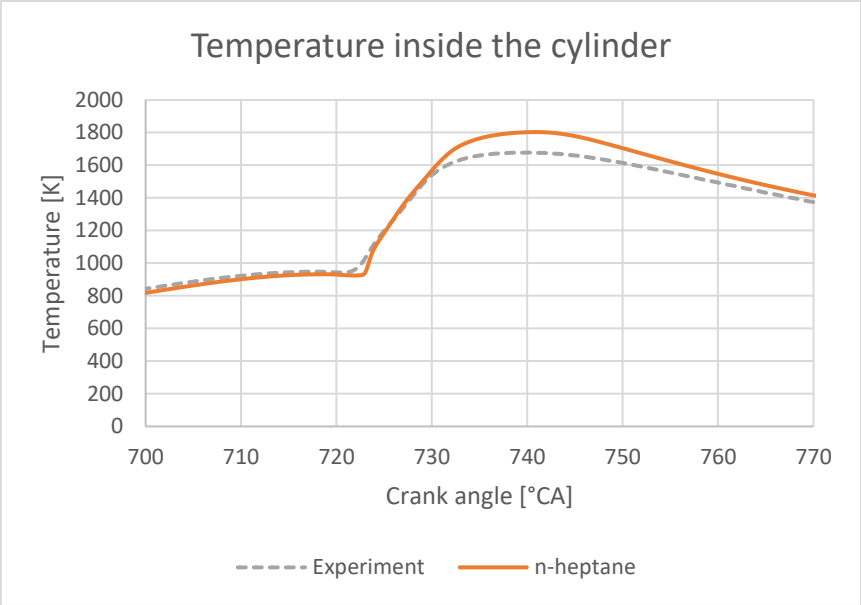

Figure 23 *Temperature inside the cylinder – case A*

There is a more significant deviation between the experimental and simulation data for the RoHR. Rapid ignition is present at the beginning of the combustion, explaining why the pressure rises faster in the simulation than in the experiment. After this initial peak, the RoHR curve from the simulation matches the experimental data quite well.

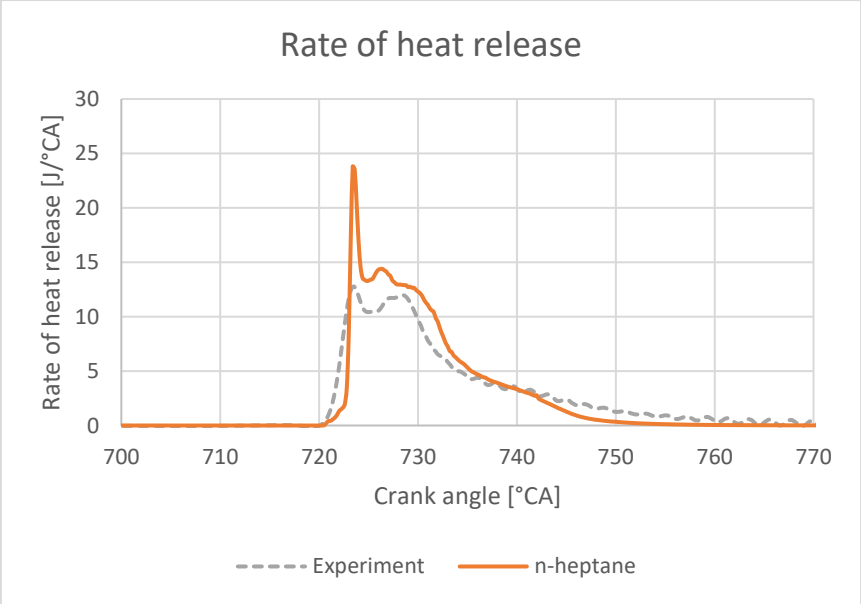

Figure 24 *Rate of heat release – case A*

5.1.2. Multi injection case – case B

In this case, the pressure curves show an excellent match. Despite minor discrepancies at the beginning of combustion, the maximum pressure achieved in the simulation is almost identical to experimental data

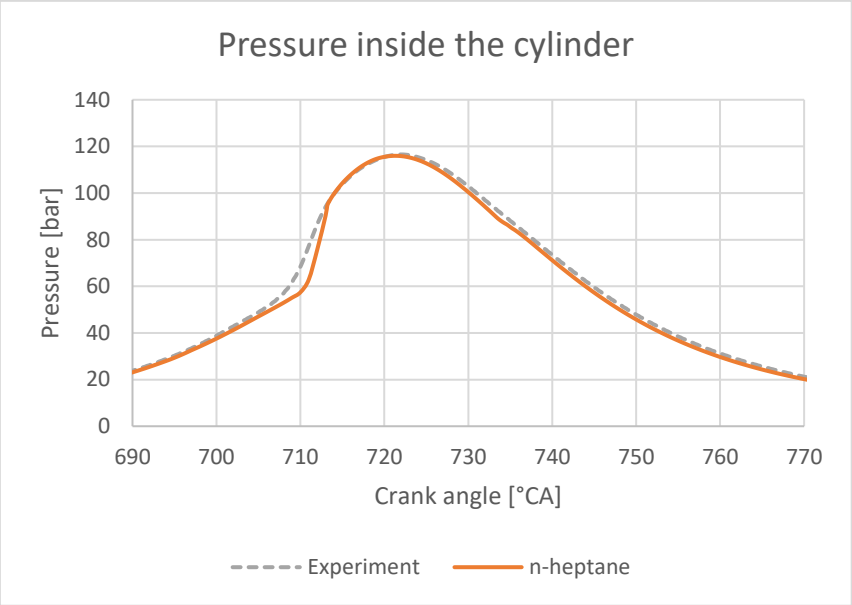

Figure 25 *Pressure inside the cylinder – case B*

The discrepancies in temperatures are more visible than those for pressure but still show a better match than case A. The ignition timing in calculated results is delayed compared to experimental data, and the faster combustion process then compensates the combustion process to achieve the same peak temperature. The faster combustion process in Figure 26 can be observed as a higher gradient value of the temperature curve at the ignition stage.

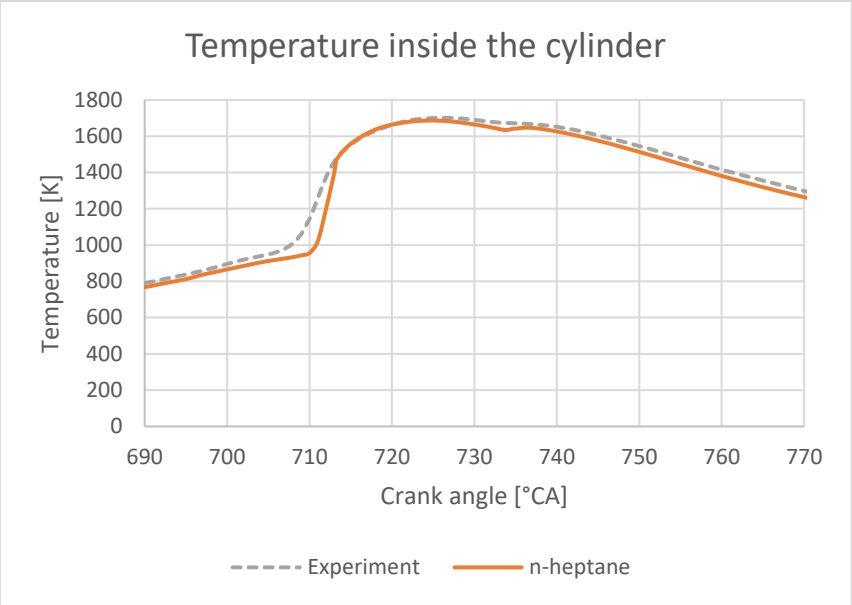

Figure 26 *Temperature inside the cylinder – case B*

Like in the previous case, rapid ignition is present. Despite this, it can be said that simulation results follow the experimental ones and reflect on all the trends occurring during combustion. The delay in ignition and heat release is also seen on the graphs showing the pressure and temperature values. Due to this delay, both the pressure and temperature start to increase later and faster than in the experiment.

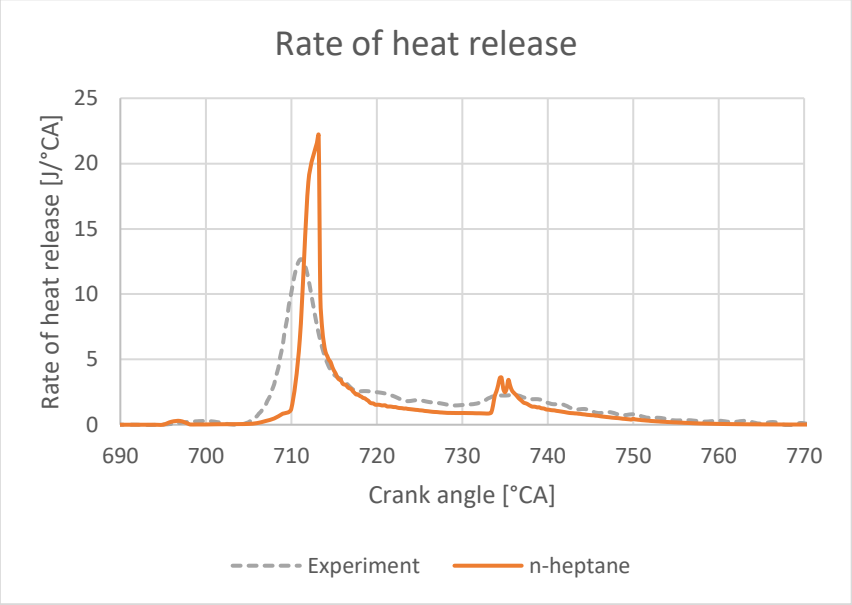

Figure 27 *Rate of heat release – case B*

5.2. First injection regime

Two different methods describe how the fuel will react in the cylinder to compare the new e-fuel OME-3 with n-heptane. One method was implementing the Lin et al. mechanism [35], which is based on the GGPR approach, describing all the possible reactions during combustion. The reasons why this mechanism was chosen is that it contains a small number of chemical species and reactions, and it was developed for ICE simulations. In general, reaction mechanisms to describe the combustion of OME-3 are computationally demanding for 3-D numerical simulations, but the Lin mechanism identifies and uses only the most crucial reactions. The mechanism consists of 61 species and 190 reactions.

The second method uses a combustion model, precisely ECFM-3Z model, which was described in Chapter 3. This method allows for even shorter computing times than Lin et al. mechanism due to the smaller number of transport equations, which are needed to be solved. The parameters used in the simulation are listed in Chapter 4.6.

As mentioned before, in the first injection regime, the start of injection, duration, and injected mass is identical to the ones from the experiment with n-heptane. The only difference is the fuel itself, which is OME-3.

5.2.1. Single injection case – case A

Figure 28 shows that combustion of OME-3 in the equivalent mass as n-heptane will produce overall lower pressure and consequently lower torque. The main reason can be found in the fact that the Lower Heating Value (LHV) of OME-3 (19,4 MJ/kg) equals less than half of the LHV of n-heptane (44,9 MJ/kg). Consequently, it is expected that less energy will be released during combustion for the same injected mass.

When comparing the Lin et al. mechanism and ECFM-3Z combustion model, the rise in pressure occurs simultaneously, however, at a slower rate in the ECFM-3Z model. The peak pressure is smaller in the ECFM-3Z model, about 10% less than the peak pressure from the model using Lin et al. mechanism.

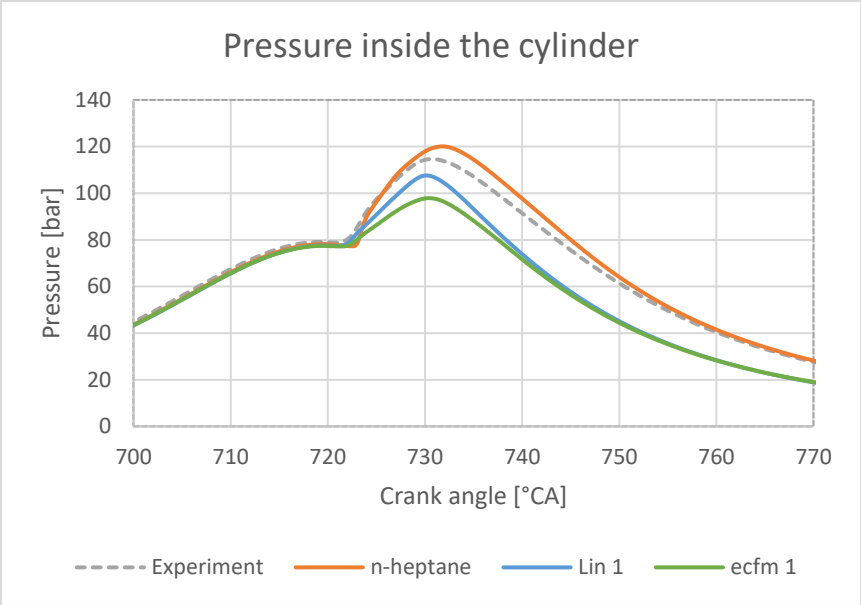

Figure 28 *Pressure inside the cylinder – case A – first injection regime*

Figure 29 shows how OME-3 burns at a lower temperature, which is expected since the amount of released energy is smaller for OME-3 than for n-heptane. One unusual thing is that the simulation using the ECFM-3Z model shows a higher increase in temperature, even though the peak pressure is lower than in the simulation, which used Lin et al. mechanism.

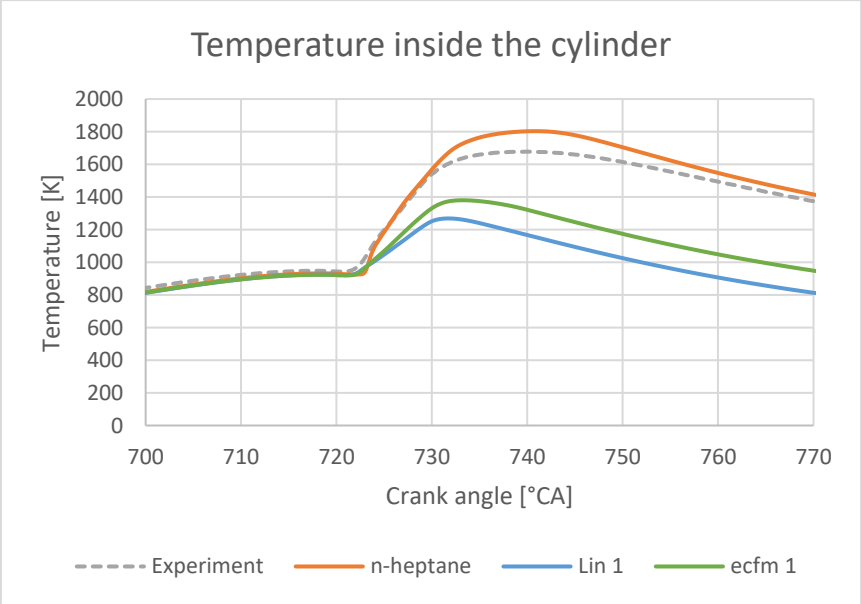

Figure 29 *Temperature inside the cylinder – case A – first injection regime*

Figure 30 shows the dynamic of OME-3 combustion well. OME-3 initially shows a faster rate of heat release than the rate of heat release in the n-heptane simulation. Although, when compared to experimental data, both n-heptane and OME-3 show a good initial match. A faster rate of heat release could be caused by weaker bonds within the atoms of the molecule and a higher oxygen content that improves combustion. The simulation with the ECFM-3Z model exhibits an overall slightly higher rate of heat release and, consequentially, higher overall increased released energy, which is measured by the area under the RoHR curve.

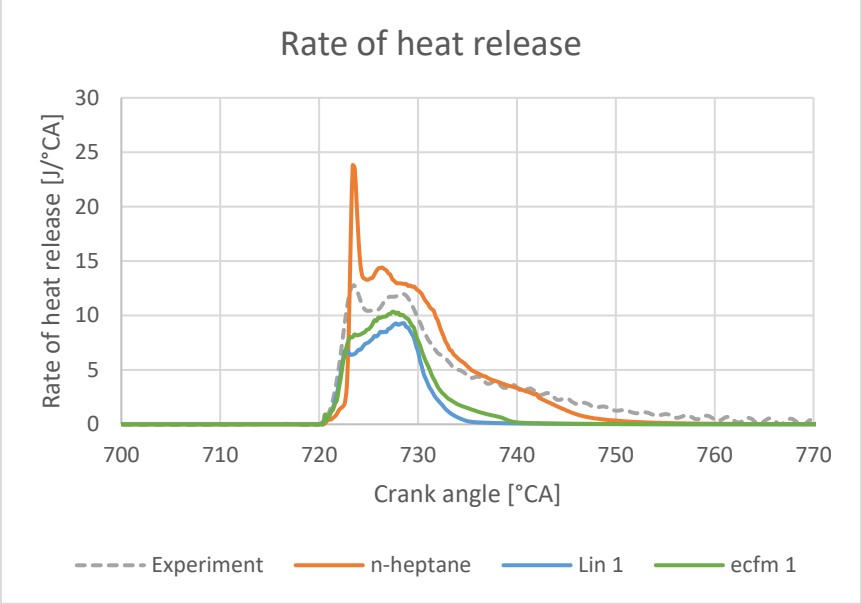

Figure 30 *Rate of heat release – case A – first injection regime*

5.2.2. Multi injection case – case B

Figure 31 shows similarly to Figure 28 how n-heptane fuel generates higher pressure during combustion than OME-3 for the same injected mass. When comparing the Lin et al. mechanism and ECFM-3Z combustion model, the rise in pressure occurs sooner with the ECFM-3Z model. In this case, ECFM-3Z model exhibits a higher peak pressure.

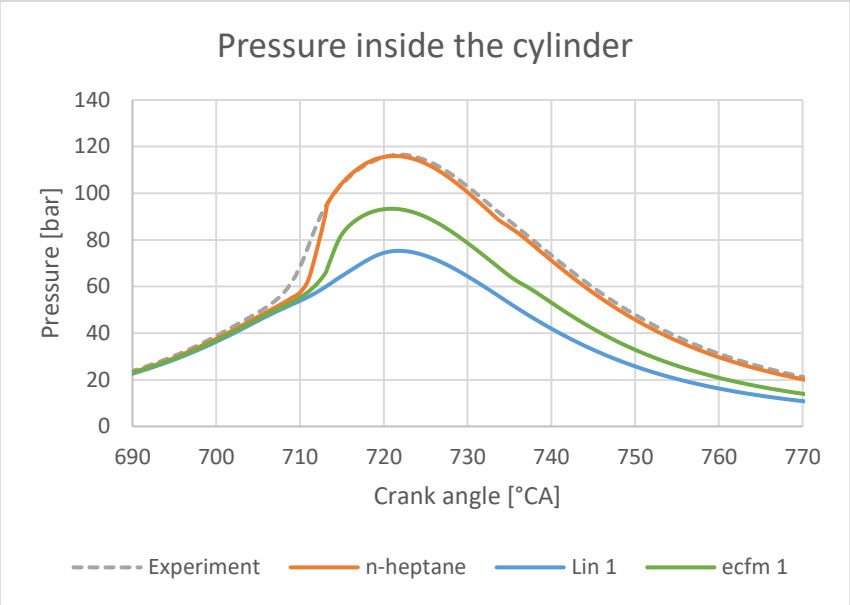

Figure 31 *Pressure inside the cylinder – case B – first injection regime*

Figure 32 shows similarly to Figure 29 how OME-3 burns at a lower temperature. The ECFM-3Z model shows significantly higher temperature values. Still, for both models can be concluded that the temperature rises slower in OME-3 than with n-heptane.

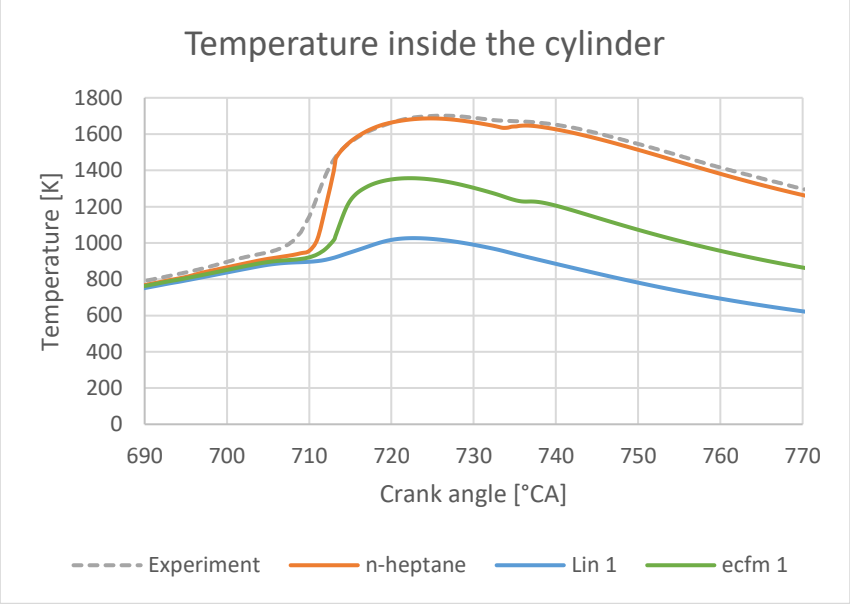

Figure 32 *Temperature inside the cylinder – case B – first injection regime*

Figure 33 shows how in the simulation with Lin et al. mechanism, the RoHR values are drastically lower than for n-heptane. Surprisingly, the simulation where ECFM-3Z was implemented shows a spike in value at the later crank angle degrees than in the experiment and about the same value. It is also noticeable how the first two injections of OME-3 have a comparatively non-existent effect on the RoHR.

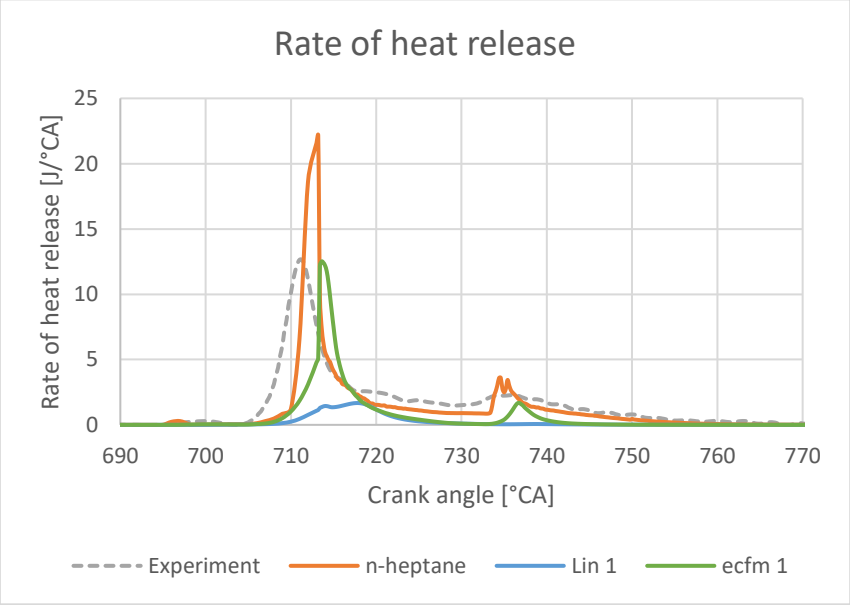

Figure 33 *Rate of heat release – case B – first injection regime*

5.3. Second injection regime

As seen in the previous chapter, injecting the same mass of OME-3 synthetic fuel as n-heptane will yield lower overall values in pressure, temperature and heat release. To compensate for this and have more comparable results, the second injection regime was created, allowing for increased injected fuel. The newly decided amount of fuel was calibrated to ensure that the accumulated heat release is almost the same as in the experiment. The start of injection in the second injection regime is the same as in the first injection regime. The only difference is the amount of injected fuel and injection duration.

5.3.1. Single injection case – case A

Figure 34 shows how the peak pressure for OME-3 fuel is slightly lower than for n-heptane and for both of the combustion models used, this peak occurs at the later crank angle degrees than for n-heptane. The rise in pressure is slower than for n-heptane, and it also decreases in value slower.

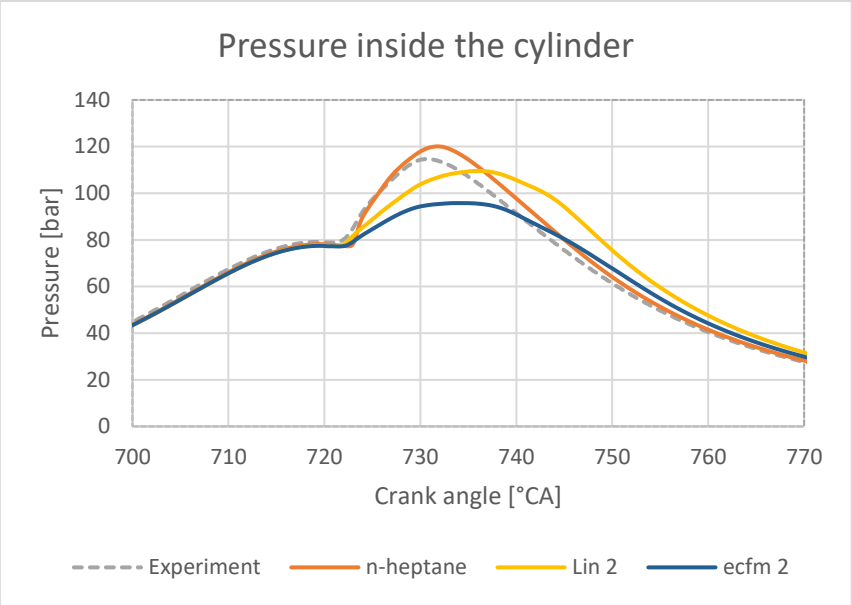

Figure 34 *Pressure inside the cylinder – case A – second injection regime*

Figure 35 shows that for the simulation with Lin et al. mechanism, lower temperature values are achieved, even when pressure is higher than for n-heptane. As was the case with the first injection regime, the ECFM model exhibits higher temperatures even though the pressure is lower than for Lin et al. mechanism.

Compared to Figure 29, the temperature gradient at the ignition start is slightly lower than in the first injection regime, where a lower amount of fuel was injected. Furthermore, ignition occurs slightly earlier, where a lower amount of fuel was injected, which can be attributed to the lower required energy for evaporation of less injected fuel. That means the mixture does not cool down as much, as in the case where more fuel is injected. When more fuel is continuously being injected, this lowers the temperature of the mixture even during combustion, so the temperature rise is slower.

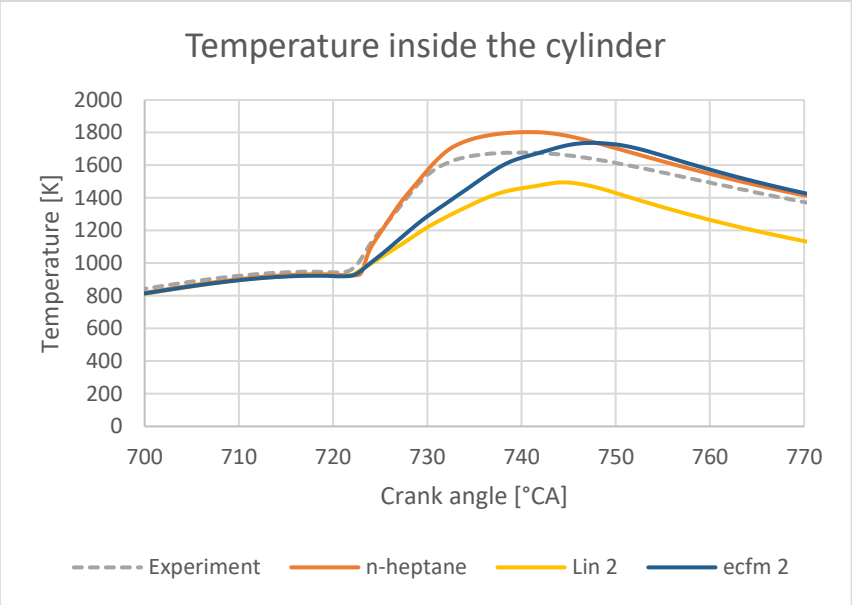

Figure 35 *Temperature inside the cylinder – case A – second injection regime*

Similar to Figure 30, Figure 36 shows a more uniform release of energy for OME-3 than for n-heptane. Both Lin et al. mechanism and ECFM-3Z combustion model show a similar trend of RoHR. It is worth mentioning that the overall released energy (measured by the area under the curves) for n-heptane and OME-3 (with higher injected mass) is almost equal. In comparison between n-heptane and OME-3, it can be concluded that OME-3 offers a more uniform release of energy without sharp increases of the RoHR. The peak value of RoHR occurs later in the second injection regime than in the first injection regime. The reason for this could be a longer injection of fuel, which cools the gas mixture while evaporating, and the longer time needed to mix the air and fuel.

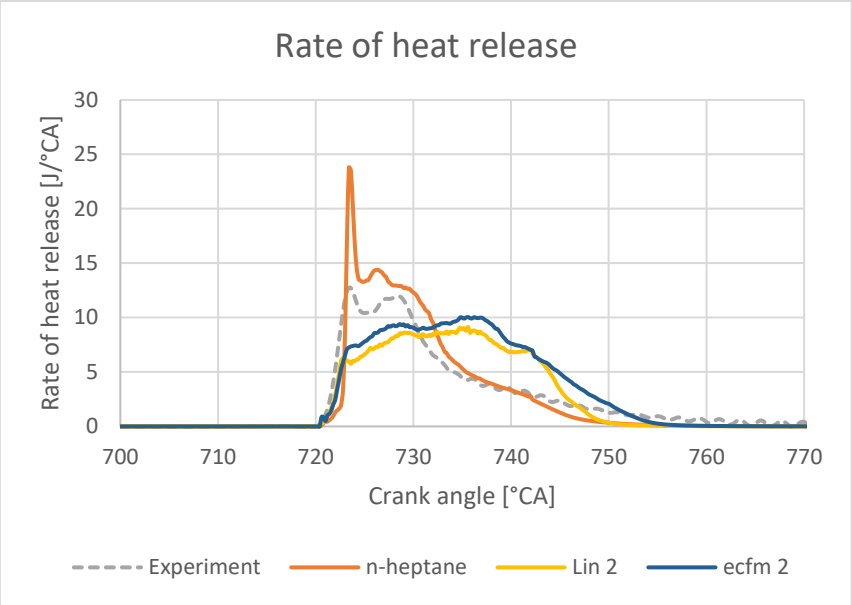

Figure 36 *Rate of heat release – case A – second injection regime*

3D results were shown in the following figures to analyse the acquired data further. In all of the figures, three simulations were examined. The first column shows the data where n-heptane and its reduced chemical mechanism were used. The second column shows the results with the chemical mechanism Lin et al., and the third column shows the combustion model ECFM-3Z results.

Figure 37 shows the behaviour of particles during the injection phase. Apart from the obvious fact that the injection lasts longer for OME-3 fuel, it is also notable that the particles of OME-3 fuel travel at a slower rate on average. Since OME-3 has a higher density than n-heptane, they have larger inertia, and the droplets will move slower out of the nozzle. Droplets that are reaching higher speeds will break up sooner, which will cause them to evaporate sooner and ignite sooner. This is another argument why n-heptane ignites sooner. There is also a slightly larger spread of particles on the end of the injected stream at 723 °CA.

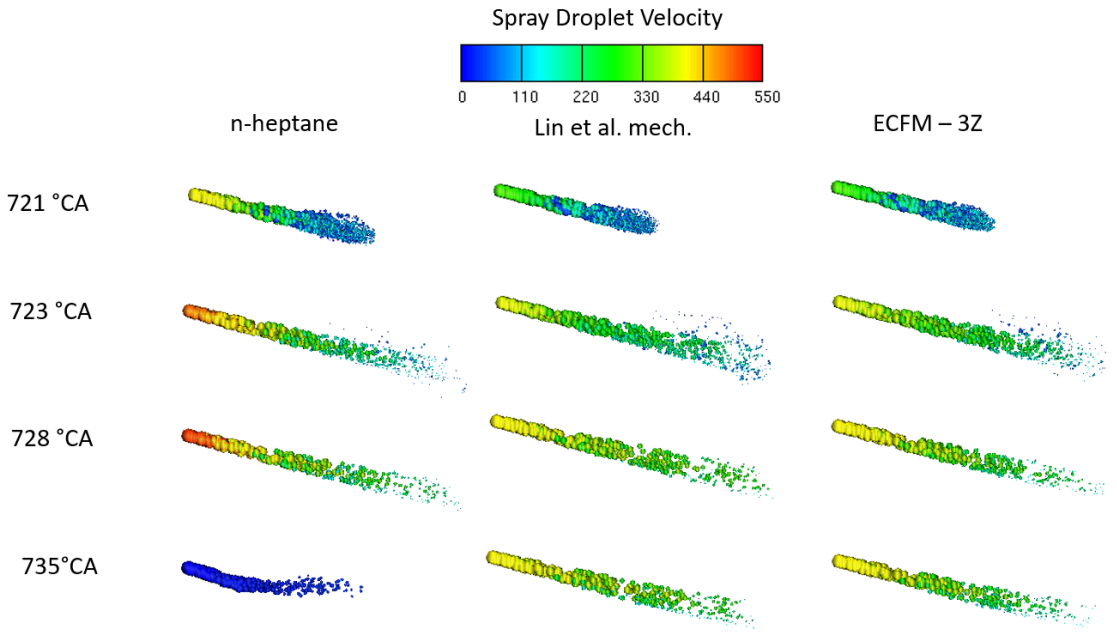

Figure 37 *Spray droplet velocity – case A – second injection regime*

Figure 38 shows the mass fraction of evaporated fuel. At the start of injection, at 721 °CA all simulations show similar behaviour. At 728 °CA, the evaporated fuel profile for n-heptane and Lin et al. mechanism is almost identical, while the ECFM-3Z case exhibits a higher amount of evaporated fuel, which also leads to better mixing of fuel and higher temperatures in comparison to the Lin et al. mechanism which can be noted in the below figure. At 740 °CA, all the fuel is already burned up in the n-heptane case, so there is no shown. The Lin et al. mechanism shows similar behaviour as at 728 °CA, while ECFM-3Z shows even more overall evaporated fuel and better mixing.

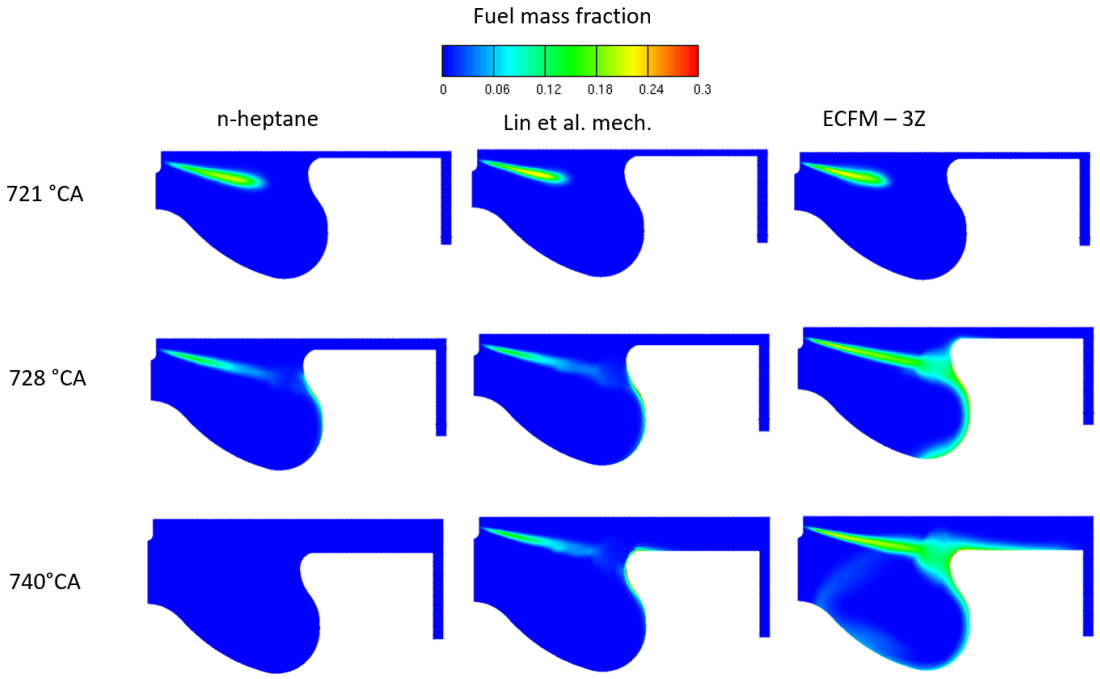

Figure 38 *Fuel mass fraction – case A – second injection regime*

Figure 39 shows the temperature profiles for various crank angles. At 721 °CA, it can be seen how due to fuel evaporation, the gases around the spray area are cooled down. N-heptane exhibits overall higher temperatures and reaches its maximum at 740 °CA, while Lin et al. and ECFM-3Z reach their maximum soon afterwards, as shown in Figure 35. Lin et al. mechanism exhibits the lowest temperatures. At 740 °CA, a local decrease in temperature around the spray area can be seen due to the 4th and final injection of fuel.

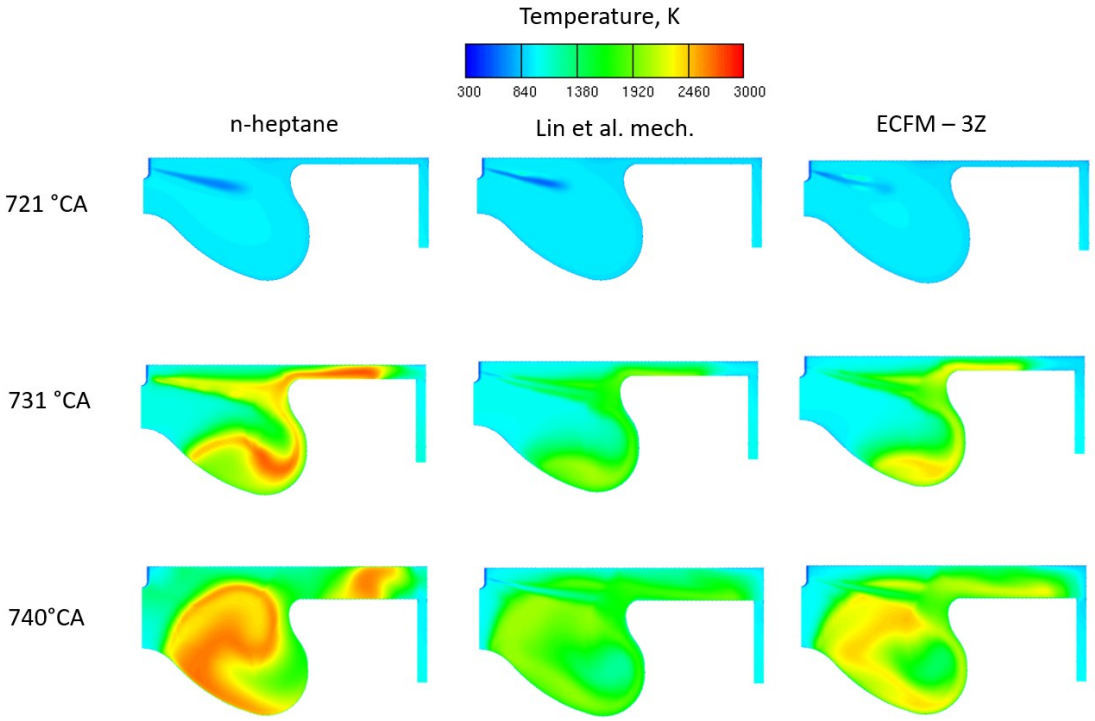

Figure 39 *Temperature field inside the cylinder – case A – second injection regime*

Figure 40 shows the CO_2 profiles inside the cylinder. From the very start, it can be seen that Lin et al. mechanism shows the highest concentration of CO_2 inside the cylinder, which indicates complete combustion of fuel. The ECFM model exhibits lower CO_2 emissions than Lin et al. mechanism, closer to the values from n-heptane.

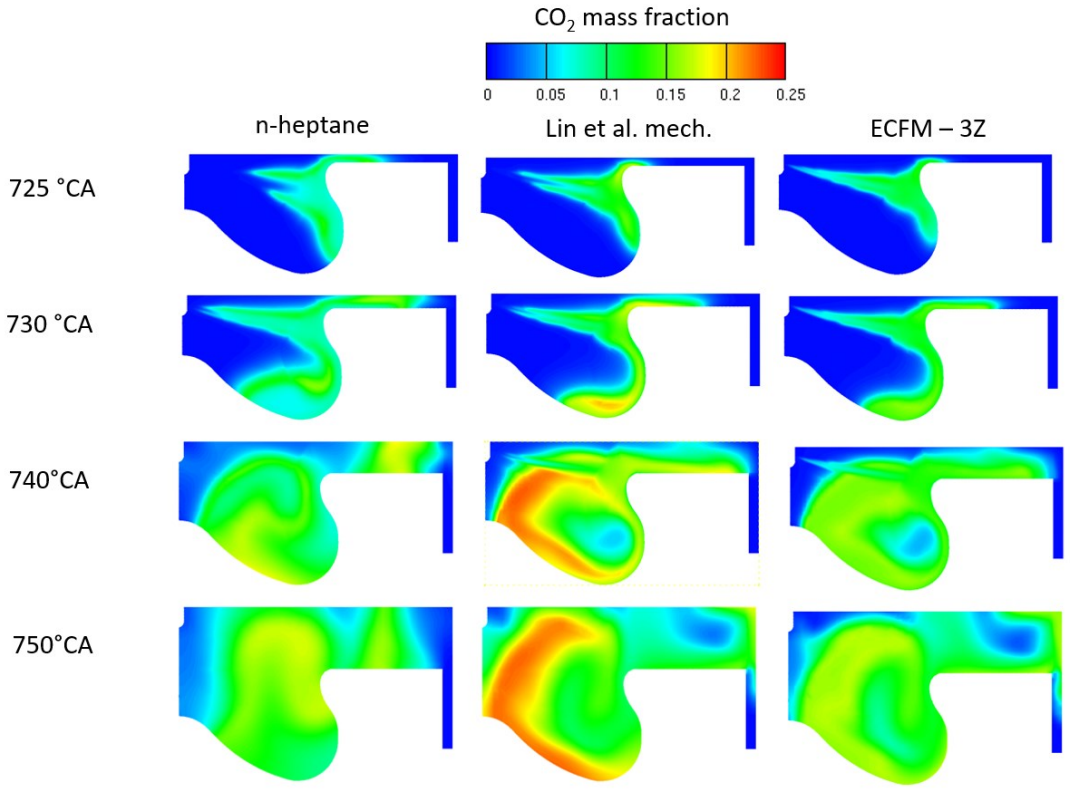

Figure 40 *CO_2 mass fraction – case A – second injection regime*

Table 14 and the subsequent figure show the resulting NOx emissions in exhaust gases. The results for Lin et al. mechanism and ECFM-3Z model are compared to experimental data and data from the simulation with n-heptane.

	NO_x mass fraction in exhaust gases
Experiment	2,53E-04
n-heptane simulation	1,65E-03
Lin et al. mech.	5,06E-06
ECFM-3Z	2,87E-04

Table 14 *NO_x mass fraction in exhaust gases – case A – second injection regime*

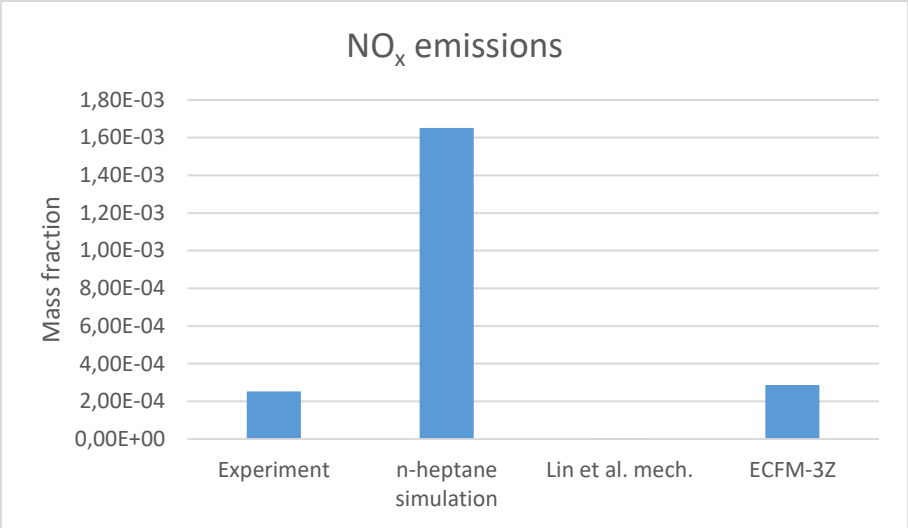

Figure 41 *NO_x mass fraction in exhaust gases – case A – second injection regime*

First off, when experimental data are compared to simulation data with n-heptane, it is seen how the simulation overpredicts NO_x emissions by almost one order of magnitude. Since simulations with OME-3 exhibit lower temperatures inside the cylinder, lower NO_x emissions are expected. ECFM-3Z model shows emissions slightly higher than the experiment with n-heptane, but considerably lower than the simulation with n-heptane.

5.3.2. Multi injection case – case B

Figure 42 shows how with the higher injected mass of OME-3, the overall pressure is higher than for n-heptane. It could indicate that OME-3 fuel performs better in the multi injection regime than the single injection regime. Also, the rise in the pressure for OME-3 is more linear than for n-heptane.

Compared to Figure 31, the rise in pressure occurs sooner in the second injection regime than in the first. This could occur due to higher injected mass during the first and second injection of fuel, before the main injection of fuel, which helped prepare the mixture inside the cylinder prior to combustion and provide enough time for fuel to evaporate and mix with the air inside the cylinder.

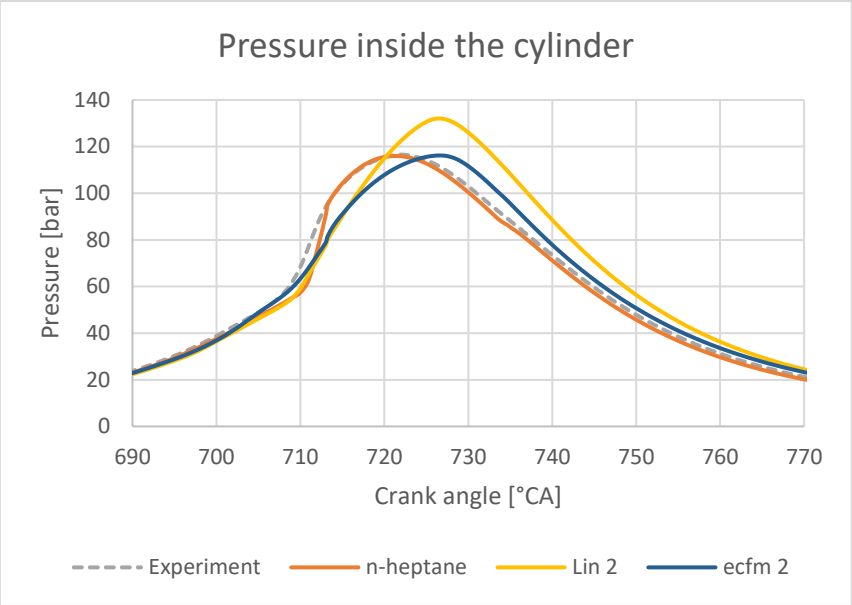

Figure 42 *Pressure inside the cylinder – case B – second injection regime*

Figure 43 shows how the simulation using Lin et al. mechanism, exhibits a lower combustion temperature despite higher pressure than for n-heptane. However, for the simulation using the ECFM-3Z model, the temperature is slightly higher, and the resulting pressure is roughly the same as for n-heptane. Compared to the first injection regime, the temperature rise is significantly higher and occurs at earlier crank angles.

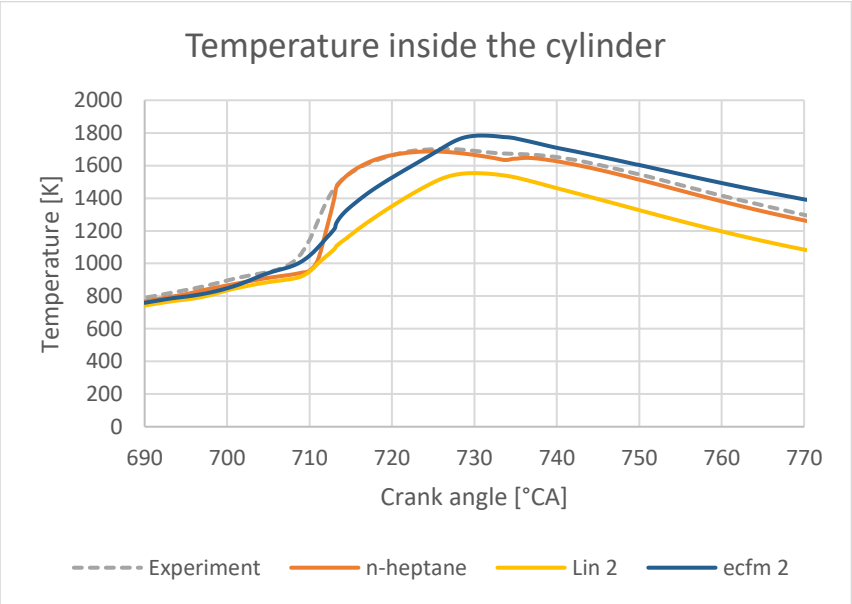

Figure 43 *Temperature inside the cylinder – case B – second injection regime*

Figure 44 shows a more uniform release of energy for OME-3 than for n-heptane. It is also noticeable how the first two injections of n-heptane fuel have a comparatively non-existent

effect on the RoHR. The injection of OME-3 (with increased mass) has a more noticeable effect.

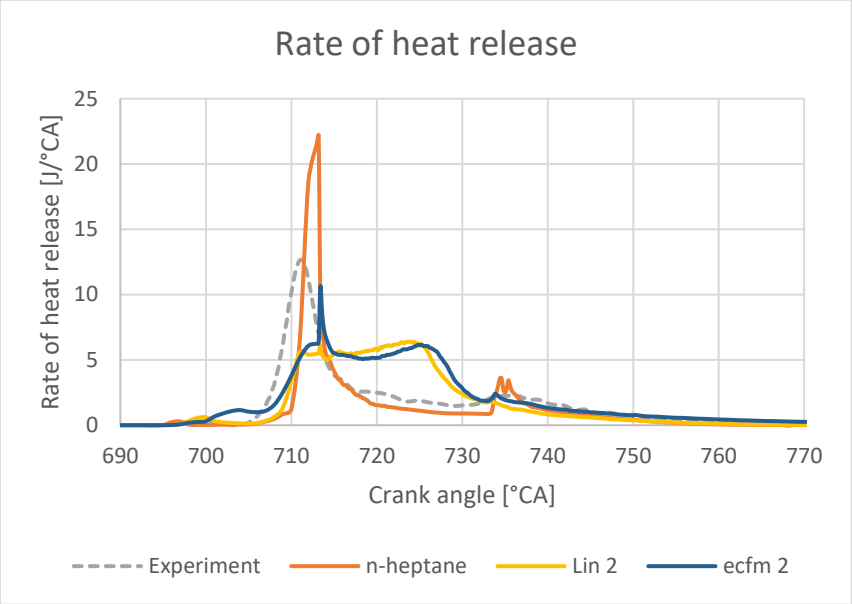

Figure 44 *Rate of heat release – case B – second injection regime*

Figure 45 shows the behaviour of particles during all of the injection phases. On the first injection of fuel, all spray profiles are very similar. On the second injection, it can be seen how droplets for OME-3 fuel travel at a higher velocity which is apparent also at later injections. The droplets are also more dispersed and smaller on the end of the stream. During the third (main) injection phase, the droplets from Lin et al. mechanism are colliding with the piston wall, resulting in a more significant dispersion of smaller particles at the end of the stream. For n-heptane and ECFM-3Z, this is not expressed in the same magnitude, a larger quantity of particles evaporate before colliding with the wall.

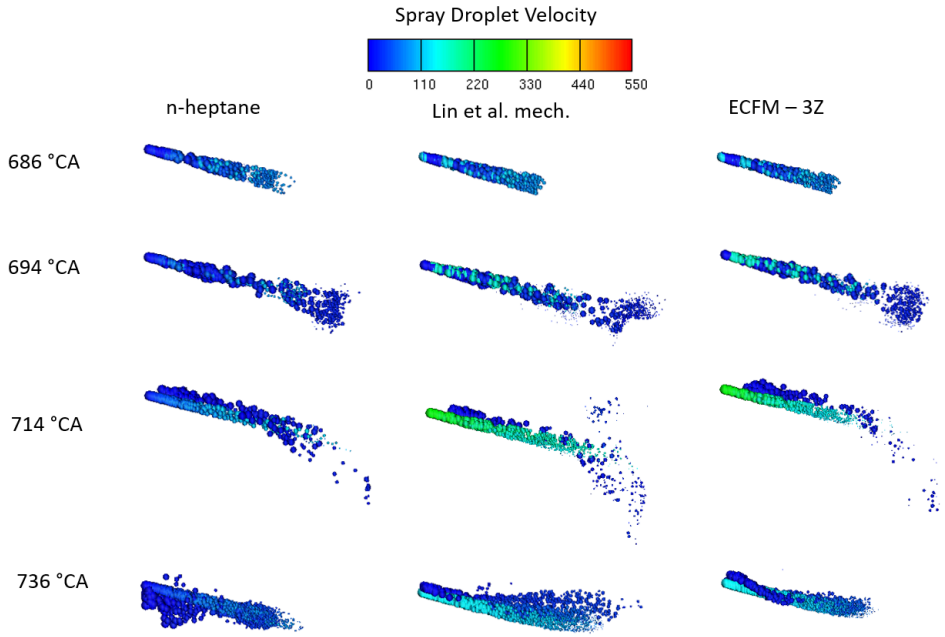

Figure 45 *Spray droplet velocity – case B – second injection regime*

Figure 46 shows the mass fraction of evaporated fuel during the 2nd, 3rd and 4th injection of fuel. At the 2nd injection, OME-3 shows slightly better evaporation than n-heptane. At later crank angles, the ECFM-3Z model clearly shows the best evaporation and mixing of fuel, leading to higher temperatures, as shown in Figure 43.

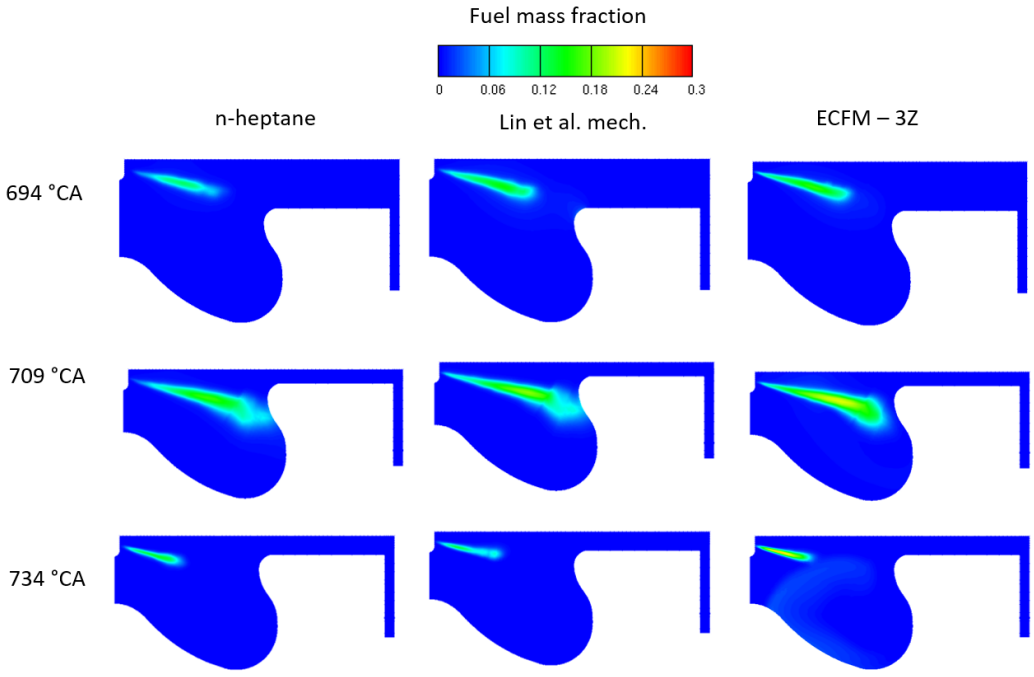

Figure 46 *Fuel mass fraction – case B – second injection regime*

Figure 47 shows the temperature profiles for various crank angles. The first two rows show temperature profiles during the 2nd and 3rd (main) injection of fuel and how temperature decreases in the spray area. At 707 °CA, combustion already starts in the ECFM-3Z model, which is also apparent in Figure 44, which shows an earlier start of heat release for ECFM-3Z than the chemical mechanism model. At later crank angles, both models with OME-3 fuel show more uniform temperature profiles, which is best observed for Lin et al. mechanism. Even though ECFM-3Z model does not reach temperatures as high as n-heptane, due to better mixing, the average temperature surpasses the average temperature of n-heptane, as seen in Figure 43.

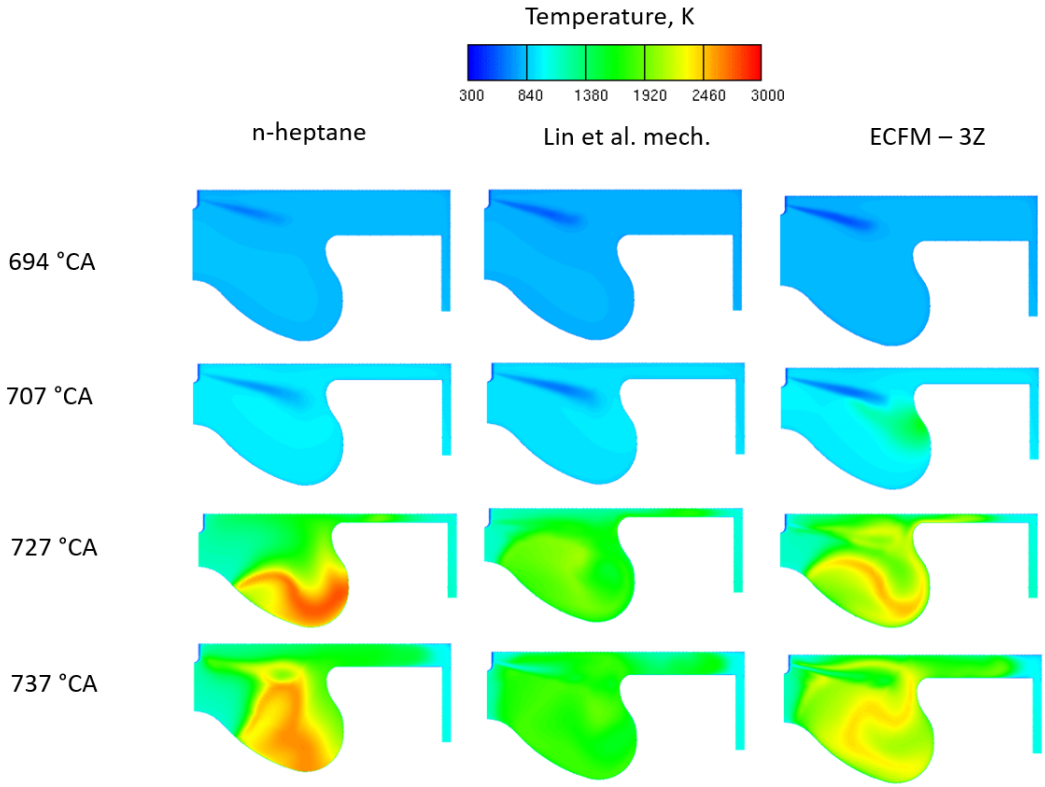

Figure 47 *Temperature field inside the cylinder – case B – second injection regime*

Figure 48 shows the CO_2 profiles inside the cylinder. At 714 °CA, simulations with OME-3 are still in the injection phase, unlike those with n-heptane. This leads to combustion not yet being fully developed and having a lower CO_2 mass fraction inside the cylinder at that moment. At later crank angles, combustion is more developed, and OME-3 cases show higher CO_2 mass fractions. This is to be expected since OME-3 is an oxygenated fuel, and it should contribute to having fewer products of incomplete combustion.

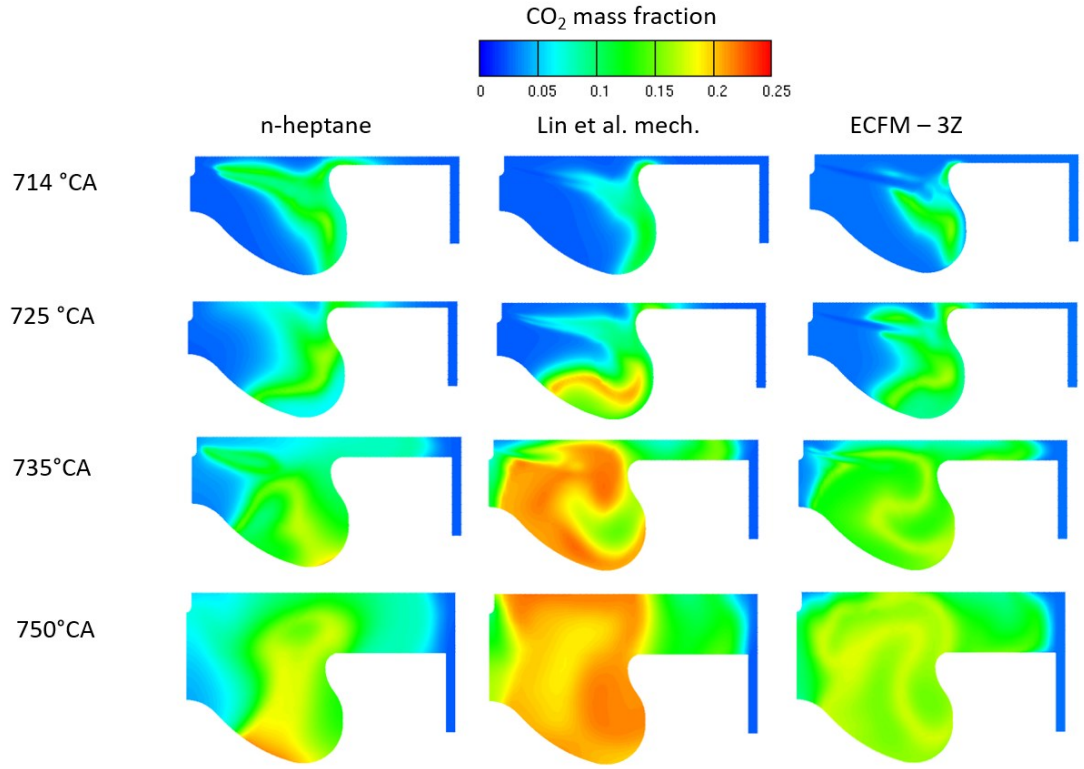

Figure 48 *CO_2 mass fraction – case B – second injection regime*

Table 15 and the subsequent figure show the resulting NOx emissions in exhaust gases. The results for Lin et al. mechanism and ECFM-3Z model are compared to experimental data and data from the simulation with n-heptane.

	NO_x mass fraction in exhaust gases
Experiment	8,80E-04
n-heptane simulation	9,77E-04
Lin et al. mech.	7,72E-07
ECFM-3Z	6,42E-04

Table 15 *NO_x mass fraction in exhaust gases – case B – second injection regime*

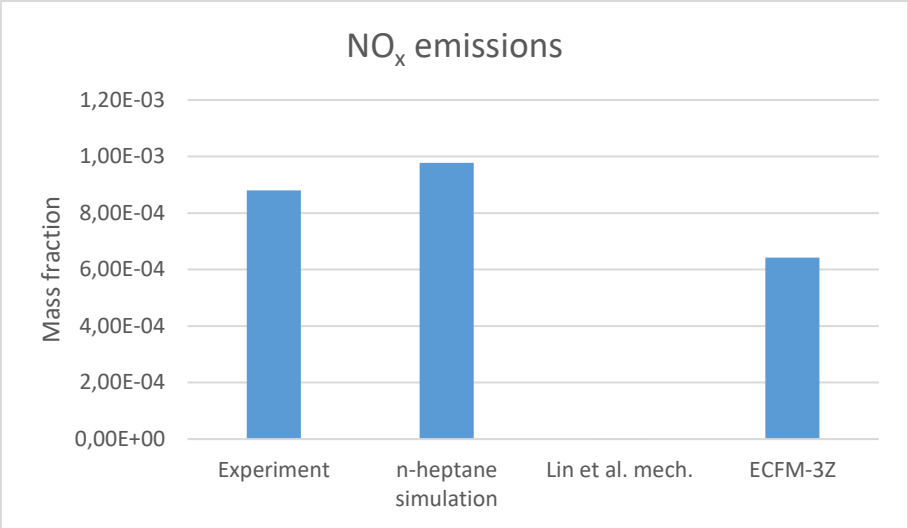

Figure 49 *NO_x mass fraction in exhaust gases – case B – second injection regime*

First off, in this case, experimental data matches simulation data with n-heptane accurately. Similarly to case A, Lin et al. mechanism shows drastically lower NOx emissions than the experiment and n-heptane simulation, while ECFM-3Z shows somewhat lower emissions, even though the temperature values for ECFM-3Z reach higher values than those for n-heptan.

5.4. Third injection regime

The third injection regime is created in order to attempt to match the experimental data in terms of pressure and the start of RoHR. The injected mass is equal to the second regime, while the start of injections is changed.

Since the simulations that use Lin et al. mechanism and the combustion model ECFM-3Z exhibit different results, optimisation was focused on the simulation using the Lin et al. mechanism. It is more accurate than the simulation with the ECFM-3Z model. This means that the optimal start of injection is decided for that simulation, and afterwards, the same injection parameters are used in the simulation with the ECFM-3Z model.

5.4.1. Single injection case – case A

Figure 50 shows results similar to Figure 34 since there weren't drastic changes in the injection parameters. In this case, the start in the rise of pressure occurs at the same time as in the experiment. Compared to the results in the second injection regime, these results show a higher maximum value of pressure which also occurs at an earlier crank angle. In the simulation with Lin et al. mechanism, the resulting pressure is the same as in the experiment, but it occurs slightly later.

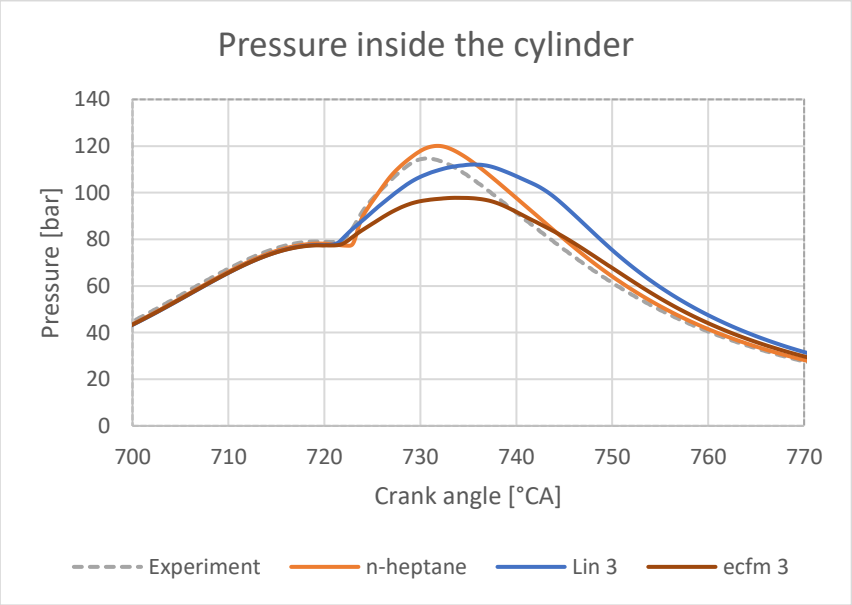

Figure 50 *Pressure inside the cylinder – case A – third injection regime*

Figure 51 shows results similar to Figure 35 since there weren't drastic changes in the injection parameters. In both simulations the rise in temperature is slower than for n-heptane. The simulation with the ECFM-3Z model matches the temperature for n-heptane around 745 °CA, while the simulation with the Lin et al. mechanism, exhibits constantly lower temperatures. The temperature gradient is almost the same as in the second injection regime, however, the rise in temperature occurs earlier in the third injection regime and matches the late stage combustion more accurately.

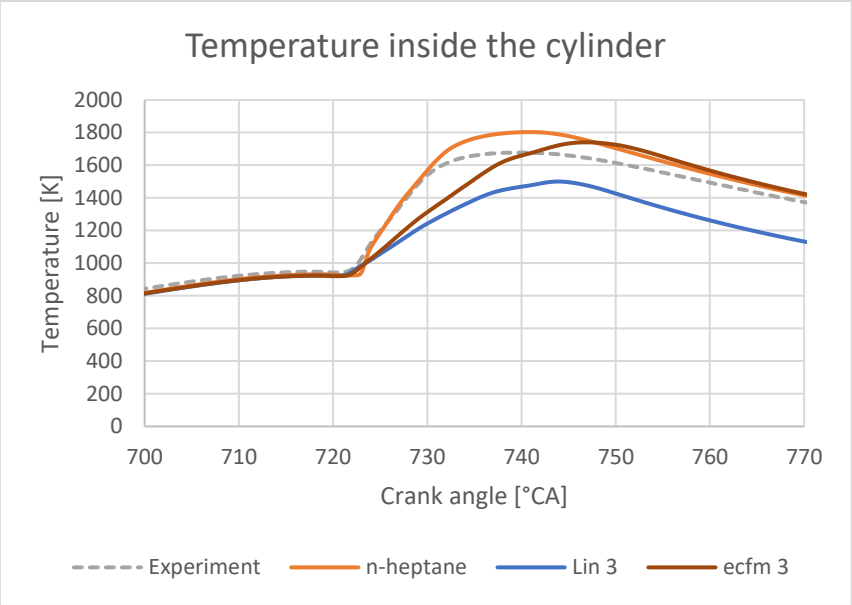

Figure 51 *Temperature inside the cylinder – case A – third injection regime*

Figure 52 shows a slightly better match at the start of RoHR than in Figure 36. The accumulated energy released is higher for the simulation with ECFM-3Z model than for the simulation with Lin et al. mechanism. OME-3 fuel shows a more uniform heat release rate in both simulations, which is also lower in value.

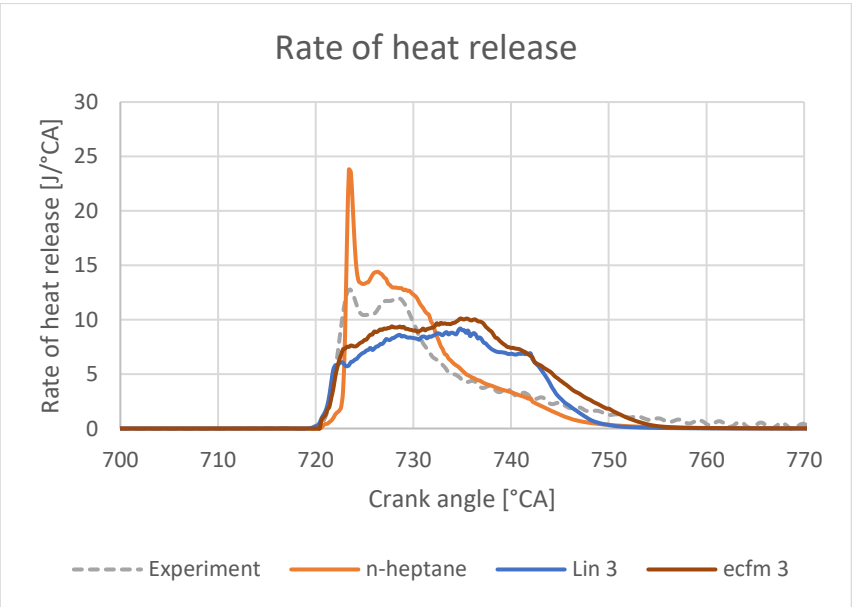

Figure 52 *Rate of heat release – case A – third injection regime*

Figure 53 shows the mass fraction of evaporated fuel. The results are almost identical to Figure 38. The main difference is that the phenomena, which occurred in the previously mentioned figure, now occur slightly earlier. At 725 °CA, the evaporated fuel profile for n-heptane and Lin et al. mechanism is almost identical. At the same time, the ECFM-3Z case exhibits a higher amount of evaporated fuel, which also leads to better mixing of fuel and higher temperatures compared to the Lin et al. mechanism, which can be noted in the figure below.

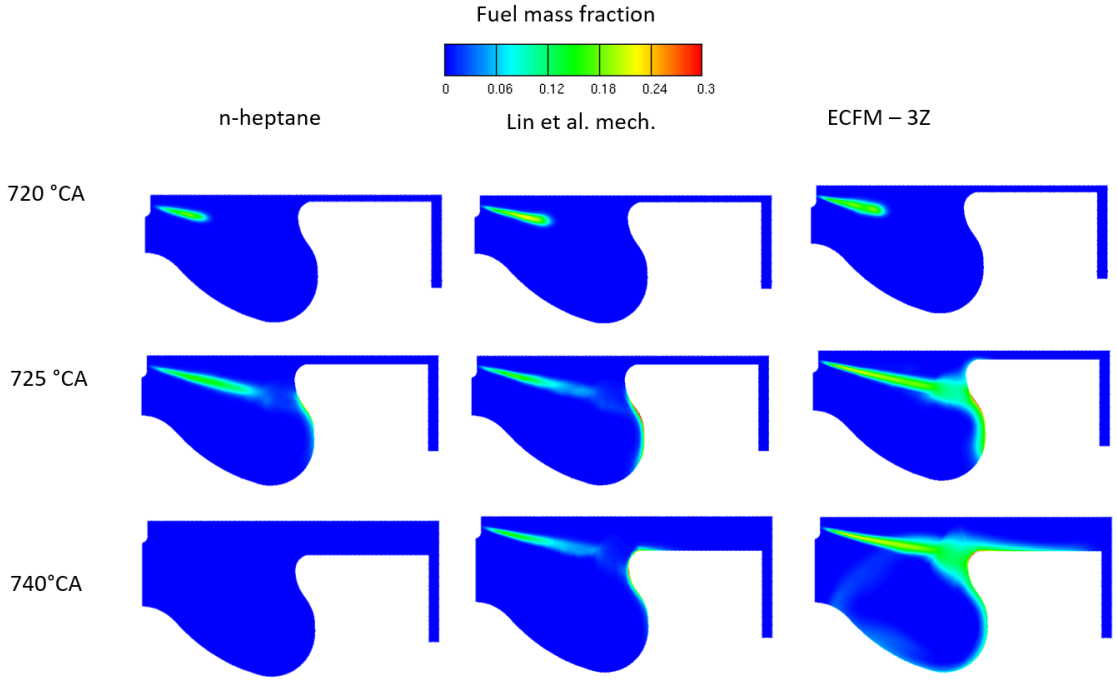

Figure 53 *Fuel mass fraction – case A – third injection regime*

Figure 54 shows the temperature profiles for various crank angles. Like in the previous case, the results are almost identical to Figure 39. However, the phenomena occur slightly earlier and match the experimental data more accurately.

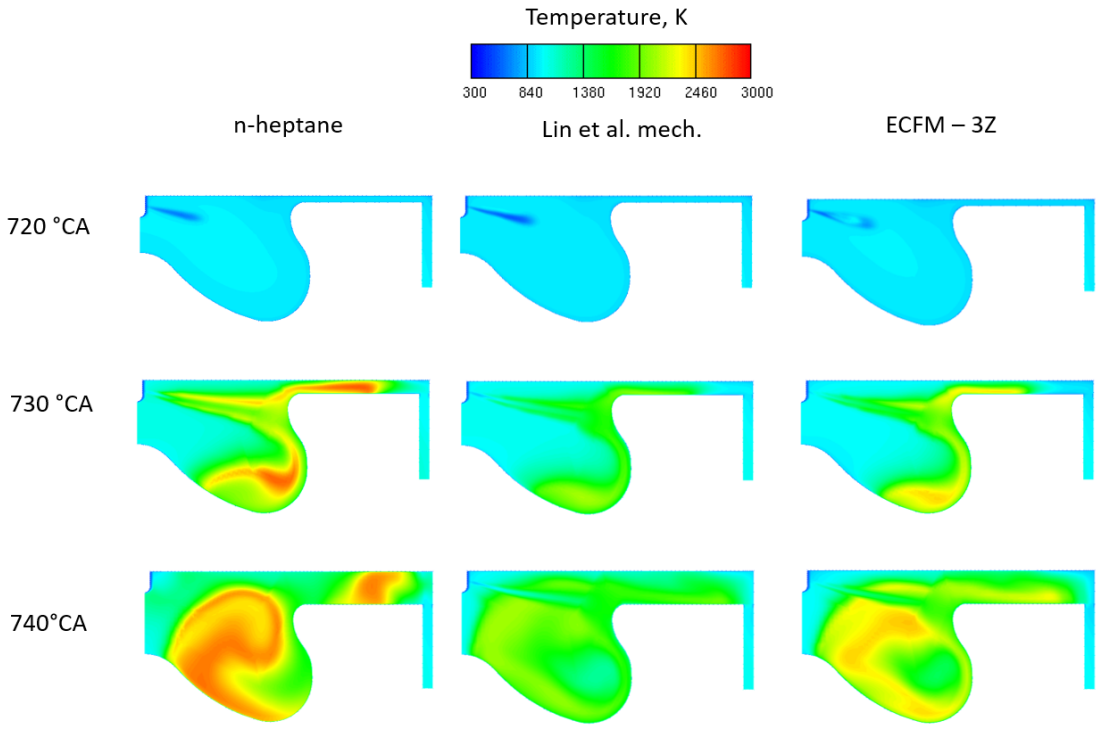

Figure 54 *Temperature field inside the cylinder – case A – third injection regime*

Figure 55 shows CO profiles inside the cylinder. N-heptane reaches overall the highest CO mass fraction, while ECFM-3Z reaches the lowest CO mass fraction. The highest CO concentrations are observed in the spray area during the injection phase. In cases when OME-3 was used, after the injection phase, the CO oxidises to CO_2 at a faster rate than when n-heptane was used. This can also be observed in Figure 56 which shows the highest concentration of CO_2 for Lin et al. mechanism.

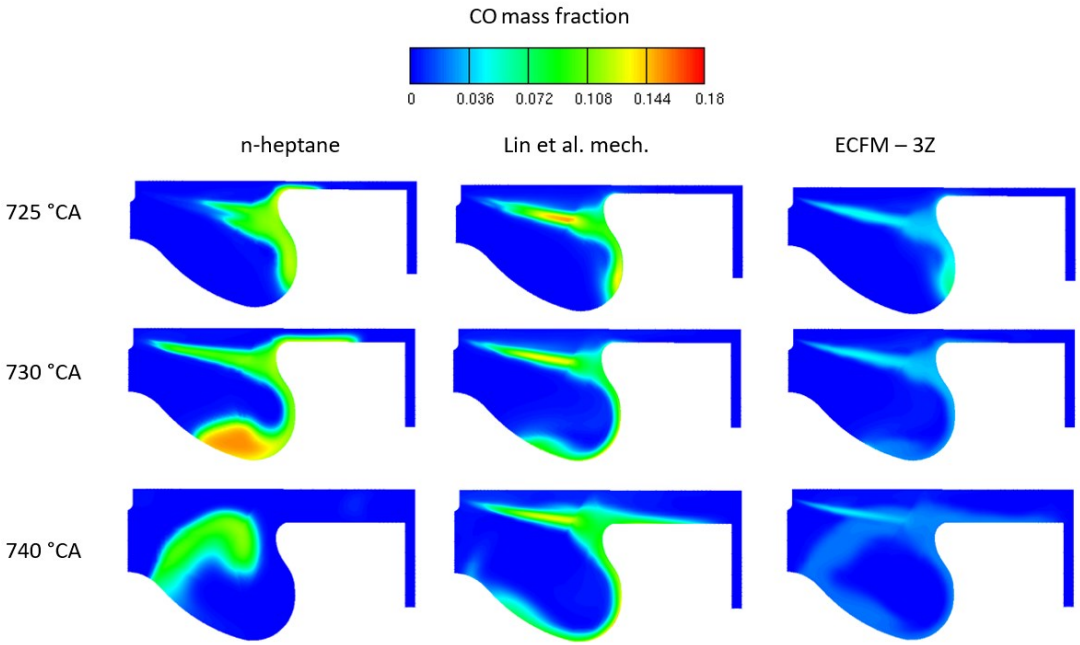

Figure 55 *CO mass fraction – case A – third injection regime*

Figure 56 shows the CO_2 profiles inside the cylinder. At 724 °CA, all simulations are in the injection phase, and fuel combustion is beginning. In this period, Lin et al. mech. and ECFM-3Z show a higher amount of CO_2 in the cylinder than n-heptane. As seen in previous figures showing CO_2 mass fractions, the Lin et al. mechanism exhibits the highest amounts of CO_2. The CO_2 profiles between Lin et al. mechanism and ECFM-3Z are almost similar in shape but different quantitatively.

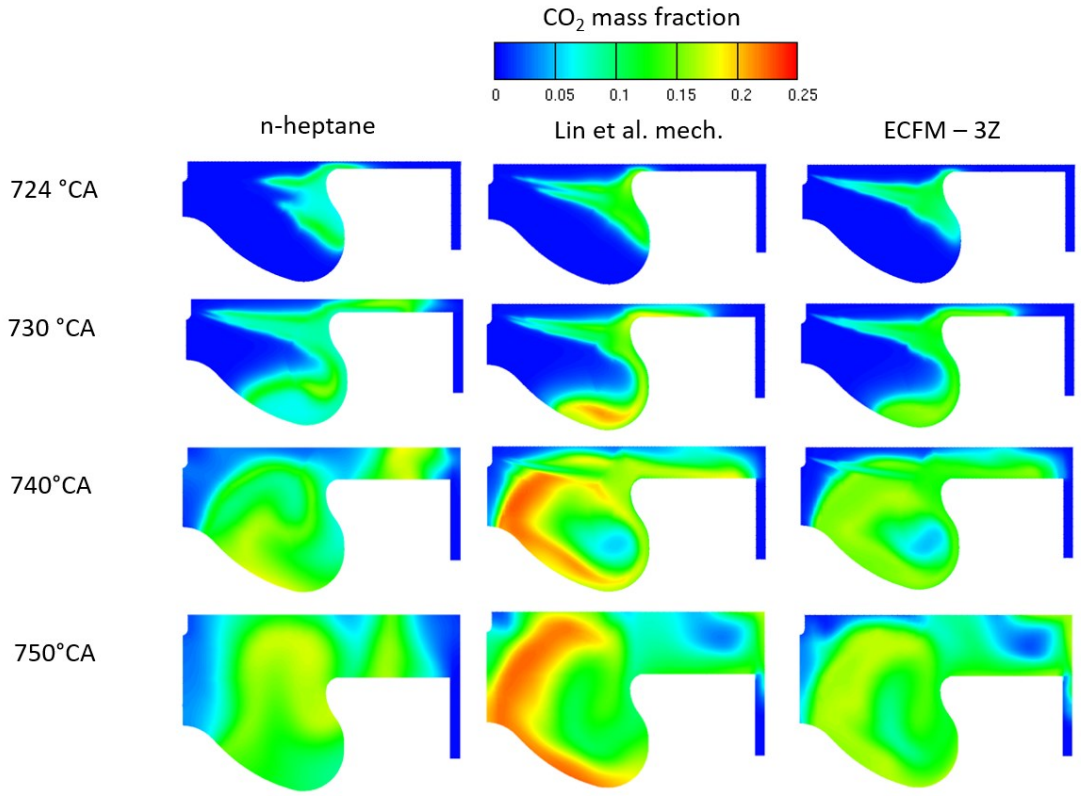

Figure 56 *CO_2 mass fraction – case A – third injection regime*

Table 16 and the subsequent figure show the resulting NO_x emissions in exhaust gases. The results for Lin et al. mechanism and ECFM-3Z model are compared to experimental data and data from the simulation with n-heptane.

	NO_x mass fraction in exhaust gases
Experiment	2,53E-04
n-heptane simulation	1,65E-03
Lin et al. mech.	5,41E-06
ECFM-3Z	3,05E-04

Table 16 *NO_x mass fraction in exhaust gases – case A – third injection regime*

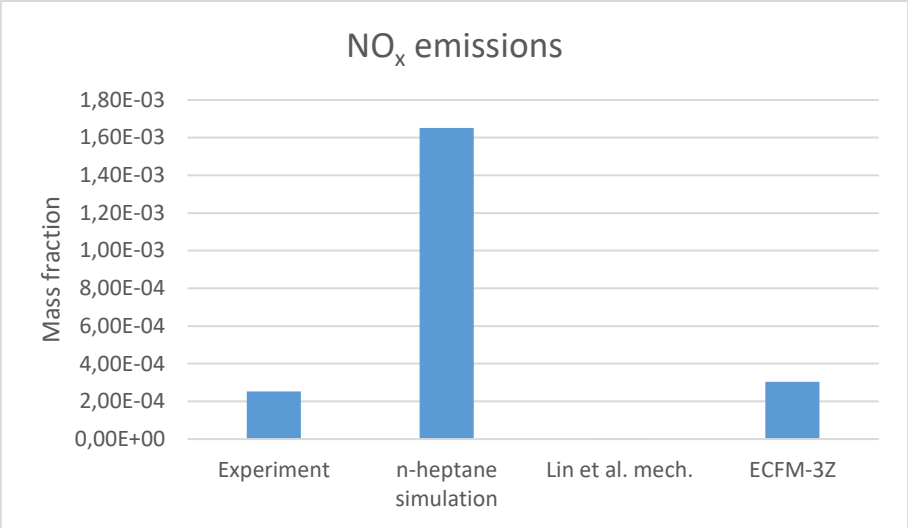

Figure 57 *NO_x mass fraction in exhaust gases – case A – third injection regime*

As it was mentioned before, in the single injection case, the simulation data overpredicts the NO_x emissions by almost one order of magnitude. In the OME-3 simulations, the temperature values are mostly lower than for n-heptane, so lower emissions of NO_x are expected. Lin et al. mechanism exhibits drastically lower NO_x emissions than expected. ECFM-3Z model shows emissions slightly higher than the experiment with n-heptane but considerably lower than the simulation with n-heptane. Compared to the second injection regime, NO_x emissions are only slightly higher due to higher temperature values in the simulation.

5.4.2. Multi injection case – case B

Figure 58 shows an earlier start in the rise of pressure than in Figure 42. It shows a better match with experimental data in the earlier stages of ignition. The resulting pressure is still higher than in experimental data. It can be assumed that the amount of injected fuel could be further decreased to achieve the same values for pressure. When comparing these results with the ones from the second injection regime, the maximum pressure value increases significantly, which would mean that the old injection regime started too late to utilise OME-3 as a fuel optimally.

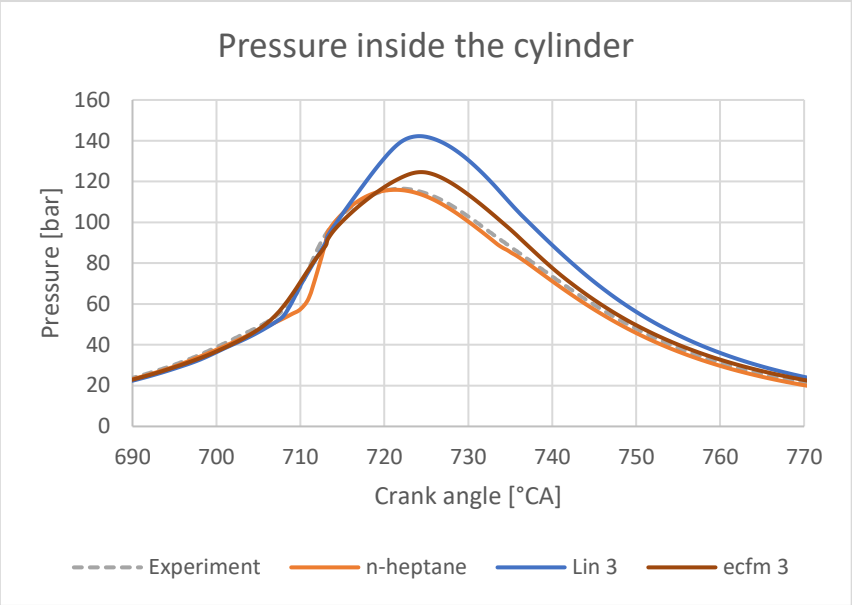

Figure 58 *Pressure inside the cylinder – case B – third injection regime*

Figure 59 exhibits similar behaviour as in Figure 43, however, the temperature values are closer to experimental data, and for both simulations, the temperature values start rising earlier. Besides, the maximum temperature values also increase and occur earlier in the simulations.

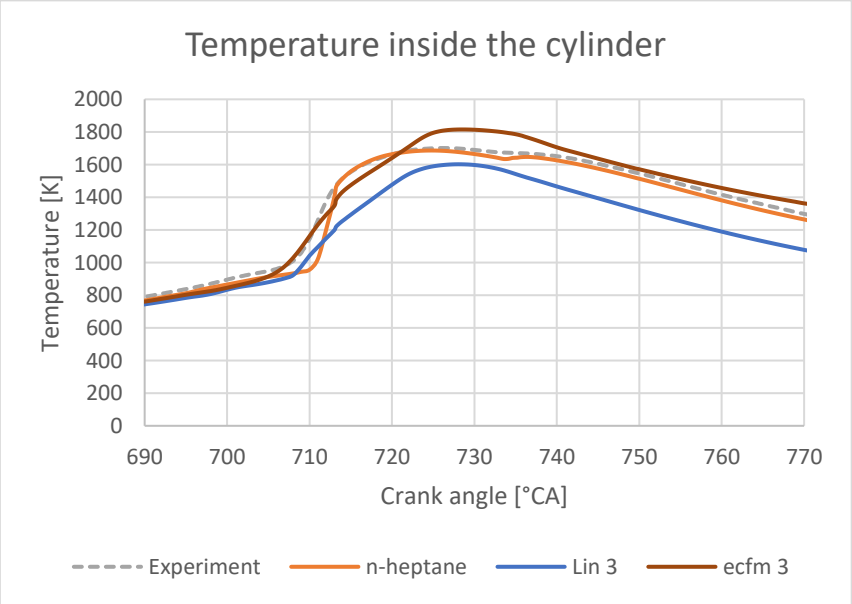

Figure 59 *Temperature inside the cylinder – case B – third injection regime*

Figure 60 shows, after the initial rise in the RoHR, fluctuating levels of RoHR, with values between 5 and 10 J/°CA. The simulation with Lin et al. mechanism shows a better initial match with experimental data than the simulation with the ECFM-3Z model. It is worth noting that both the Lin et al. mechanism and ECFM-3Z model exhibit a rapid increase in value at the same crank angle where the simulation with n-heptane reaches its maximum.

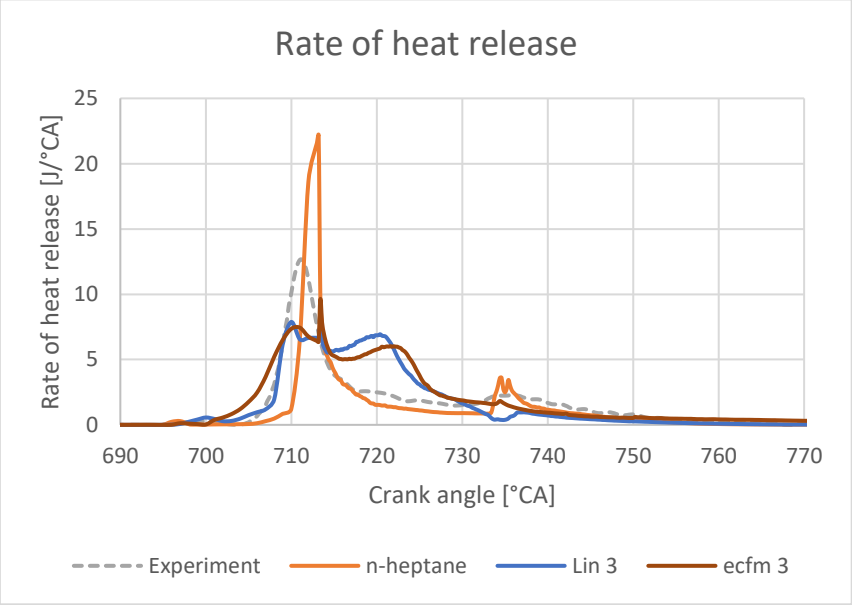

Figure 60 *Rate of heat release – case B – third injection regime*

Figure 61 shows the mass fraction of evaporated fuel during the 2nd, 3rd and 4th injection of fuel. Since the third injection regime consists of changed injection periods, they do not correspond anymore to the injection periods from n-heptane. For this reason, the first and third fuel mass region for n-heptane do not show any traces of fuel. When comparing the Lin et al. mechanism and ECFM-3Z model, the ECFM-3Z model shows better fuel evaporation, leading to higher temperatures inside the cylinder, as shown in the figure below.

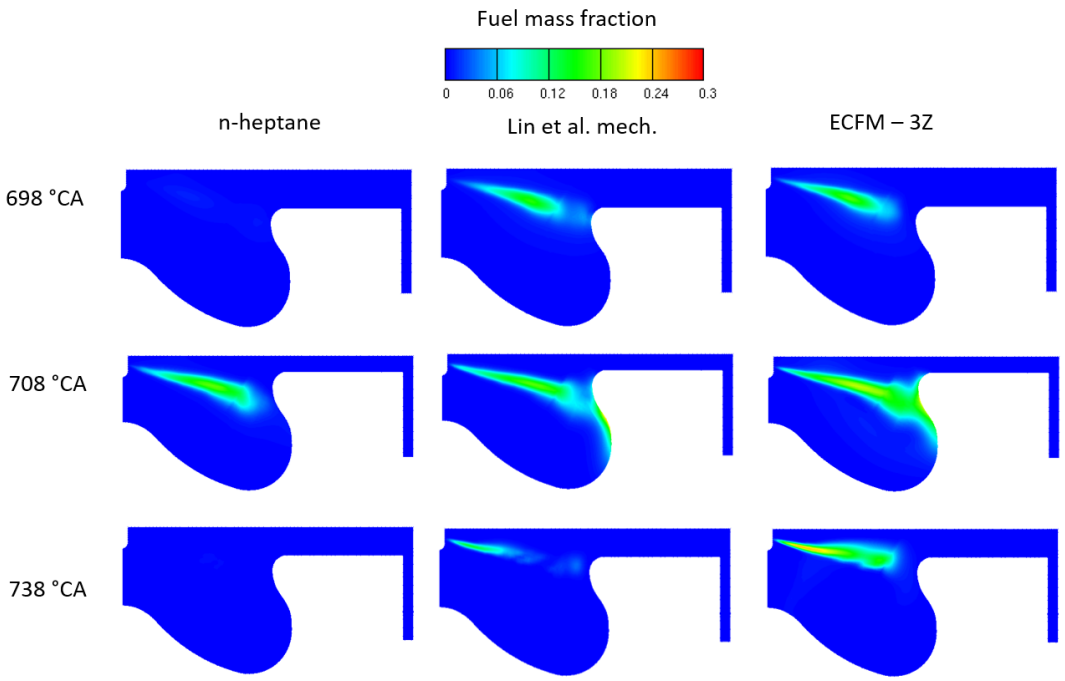

Figure 61 *Fuel mass fraction – case B – third injection regime*

Figure 62 shows the temperature profiles for various crank angles. The first two rows show temperature profiles during the 2nd and 3rd (main) fuel injection and how temperature decreases in the spray area. At 708 °CA, combustion already starts in the ECFM-3Z model. Like in the second injection regime, compared to n-heptane, the temperature profile is more uniform for both models using OME-3. Furthermore, compared to the single injection case, the temperature profile is more uniform due to better mixing of fuel and air, which occurs after the first two fuel injections.

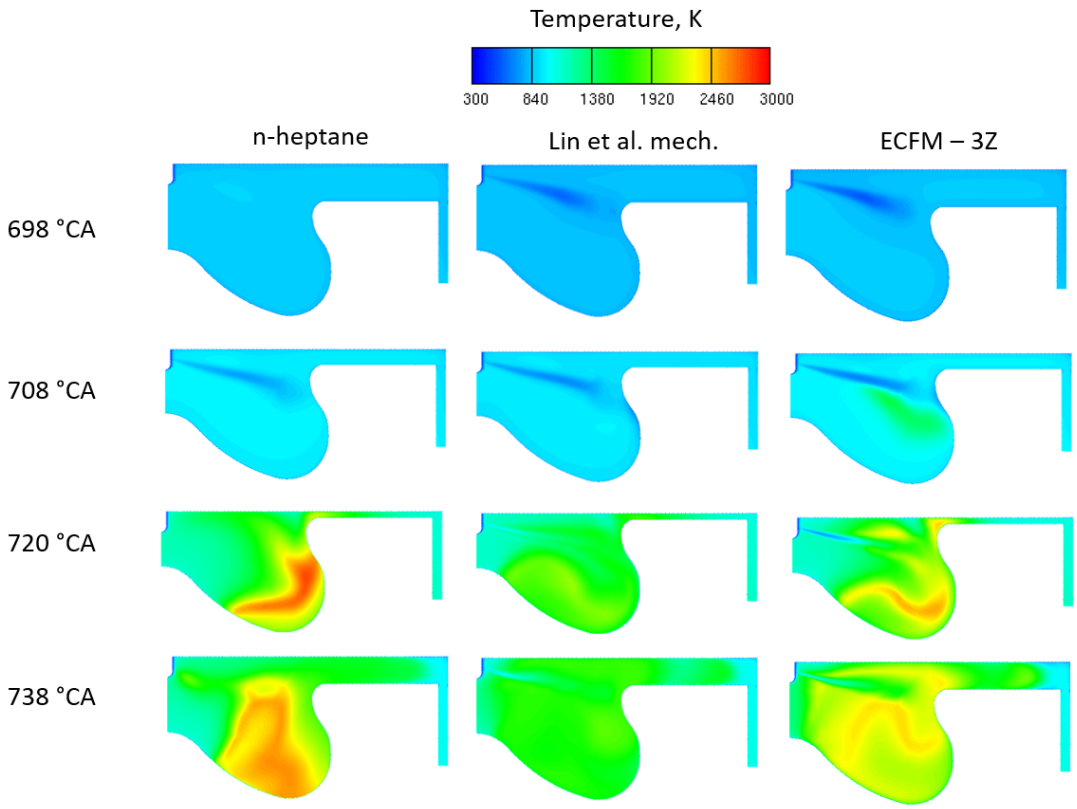

Figure 62 *Temperature field inside the cylinder – case B – third injection regime*

Figure 63 shows the CO profiles inside the cylinder. OME-3 shows higher CO concentrations during the main fuel injection than n-heptane, but this is due to more fuel being injected compared to n-heptane results. However, at later crank angles, CO decreases more quickly than for n-heptane. This is noticeable for Lin et al. mechanism at 735 °CA. Figure 64 also shows how the CO_2 mass fraction is the highest for Lin et al. mechanism.

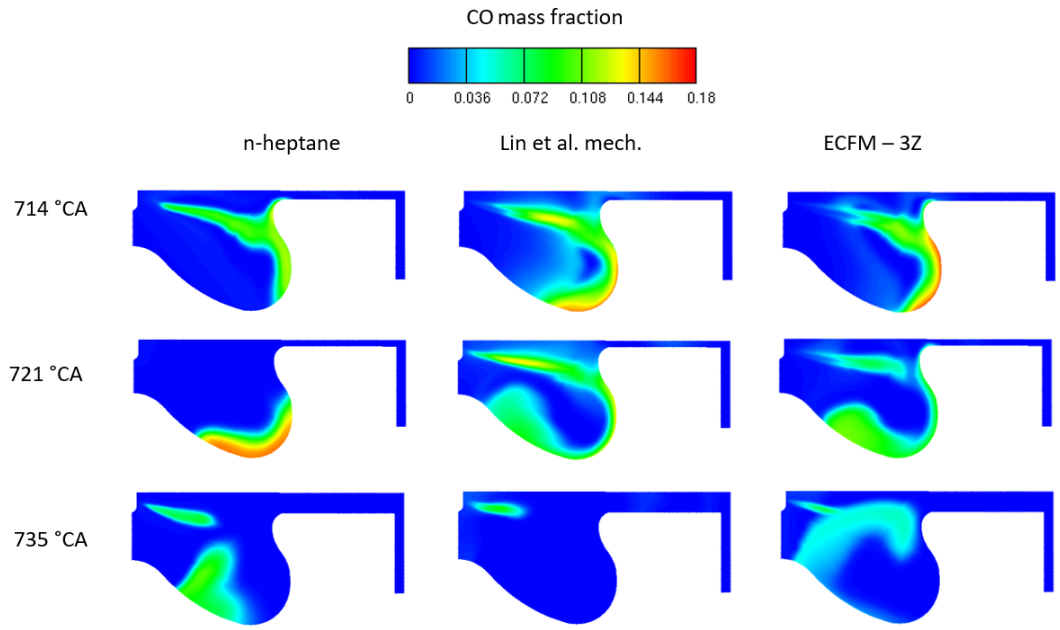

Figure 63 *CO mass fraction – case B – third injection regime*

Figure 64 shows the CO_2 profiles inside the cylinder. The results are very similar to the results in Figure 48. The most significant difference is seen in the simulation using Lin et al. mechanism. In the third injection regime, CO_2 develops earlier inside the cylinder. This is expected since the start of combustion, and the subsequent rise in pressure and temperature occur earlier than in the second injection regime. Compared to the single injection case, CO_2 is more evenly spread and reaches higher mass fraction values. This is most accentuated in Lin et al. mechanism.

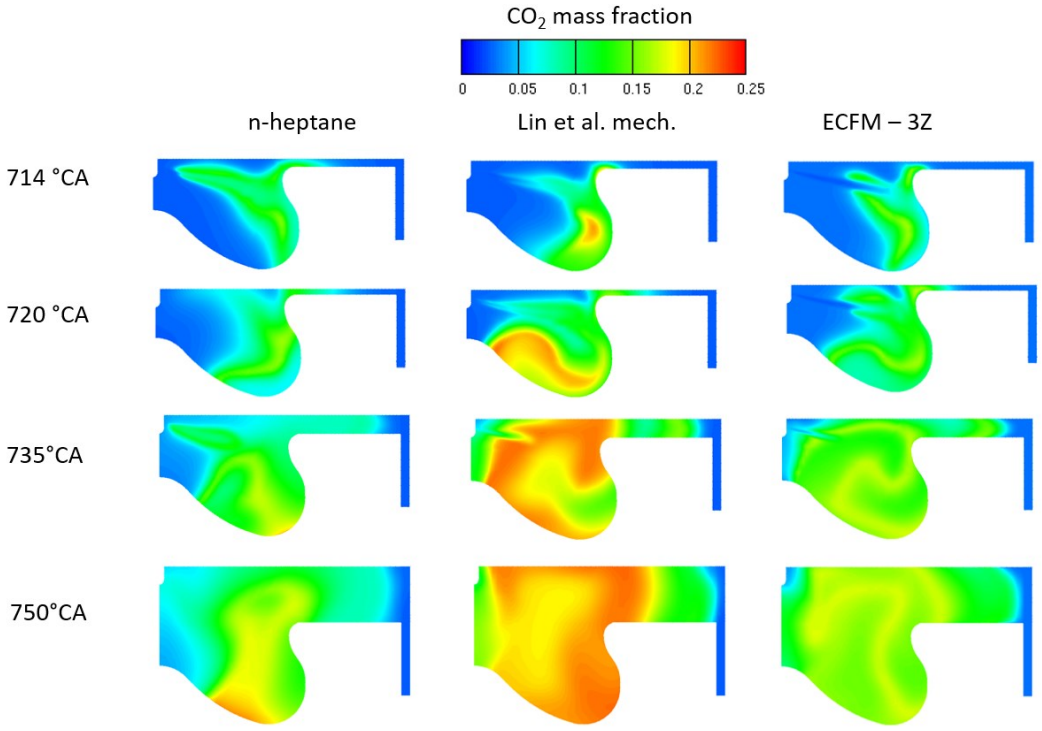

Figure 64 *CO_2 mass fraction – case B – third injection regime*

Table 17 and the subsequent figure show the resulting NOx emissions in exhaust gases. The results for Lin et al. mechanism and ECFM-3Z model are compared to experimental data and data from the simulation with n-heptane.

	NO_x mass fraction in exhaust gases
Experiment	8,80E-04
n-heptane simulation	9,77E-04
Lin et al. mech.	1,08E-06
ECFM-3Z	9,71E-04

Table 17 *NO_x mass fraction in exhaust gases – case B – third injection regime*

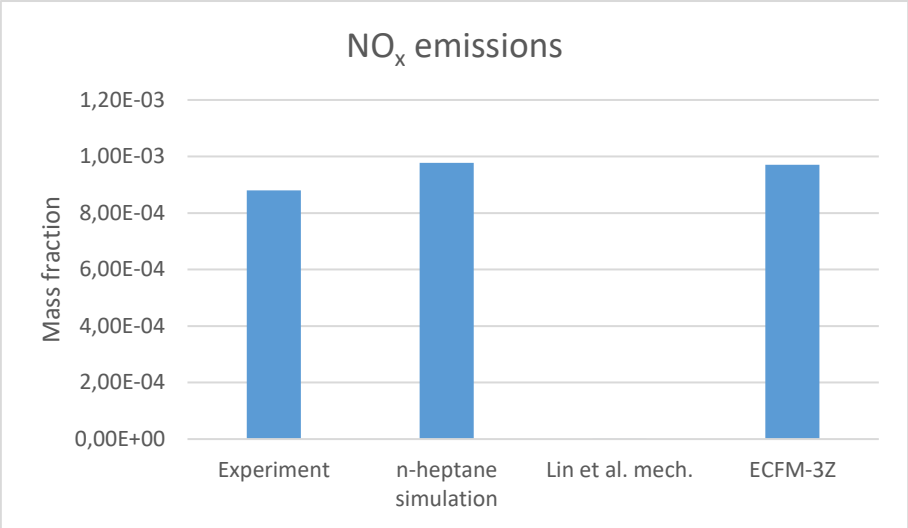

Figure 65 *NO_x mass fraction in exhaust gases – case B – third injection regime*

In this case, experimental data matches simulation data with n-heptane accurately. Similarly to previous cases, Lin et al. mechanism shows drastically lower NO_x emissions than the other simulations. In contrast, the ECFM-3Z model exhibits almost the same amount of NO_x emissions as the simulation with n-heptane. However, ECFM-3Z reaches higher temperature values than n-heptane, so that should be taken into account.

6. Conclusion

In this work, an overview of synthetic fuels was given with an emphasis on OME-3. A comprehensive list of all the phyisco-chemical properties was given in Chapter 2. The fuel has many favourable properties which allow for implementation in current ICE diesel engines. Also, a list of potential synthesis routes is given, with varying degrees of sustainability and operating cost.

CFD software AVL FIRE™ was used to model the diesel engine in which the simulations with e-fuel OME-3 were run. In the first step, the numerical mesh was validated against experimental data, where n-heptane was used as fuel. The simulation data in both the single and multi-injection case match the experimental data well, despite slight deviations of RoHR from experimental data. The next step consisted of varying the mass of injected fuel and injection regimes to assess how the fuel behaves and achieve performance comparable to that of n-heptane. When comparing OME-3 to n-heptane, it has to be noted that OME-3 has a significantly lower LHV than n-heptane, which means that in order to retain similar performance properties of current engines in the transport sector, fuel consumption and length of injection time will have to be increased. Additionally, this e-fuel will have to have an earlier start of injection compared to conventional fuel.

Compared to n-heptane, OME-3 allows a more uniform release of energy. It also improves combustion conditions, makes the combustion more complete due to a higher percentage of oxygen in the fuel molecules. It lowers NO_x and soot emissions which is also important for diesel engines. Considering all cases, the case with the multi injection regime of OME-3 displays a larger maximum pressure than n-heptane, suggesting that OME-3 performs better in that regime than in the single injection regime.

Even though there are differences present between the simulations using the Lin et al. chemical mechanism and ECFM-3Z combustion model, the main trends in the behaviour of OME-3 as a fuel are described. With additional validation with other models and additional optimisation of parameters, better results could be achieved, and more accurate predictions could be made.

Literature

[1] "Porsche to begin production of CO2-slashing eFuel next year | This is Money." https://www.thisismoney.co.uk/money/cars/article-9286773/Porsche-begin-production-CO2-slashing-eFuel-year.html (accessed Feb. 25, 2021).

[2] "Schematic illustration of the components of a fluorimeter. | Download Scientific Diagram." https://www.researchgate.net/figure/Schematic-illustration-of-the-described-power-to-X-technologies-A-Power-to-Gas-B_fig1_323094619 (accessed Jan. 05, 2021).

[3] S. Rönsch *et al.*, "Review on methanation - From fundamentals to current projects," *Fuel*, vol. 166, no. October, pp. 276–296, 2016, doi: 10.1016/j.fuel.2015.10.111.

[4] S. Friedman, P. M. Yavorsky, S. Akhtar, and I. Wender, "COAL LIQUEFACTION.," Jul. 1974, doi: 10.1002/14356007.a07_197.pub2.

[5] S. Schemme, R. C. Samsun, R. Peters, and D. Stolten, "Power-to-fuel as a key to sustainable transport systems – An analysis of diesel fuels produced from CO2 and renewable electricity," *Fuel*, vol. 205. Elsevier Ltd, pp. 198–221, 2017, doi: 10.1016/j.fuel.2017.05.061.

[6] A. De Klerk, "Transport Fuel. Biomass-, Coal-, Gas- and Waste-to-Liquids Processes.," in *Future Energy: Improved, Sustainable and Clean Options for our Planet*, Elsevier Inc., 2013, pp. 245–270.

[7] L. Yang and X. Ge, "Biogas and Syngas Upgrading," vol. 1, Elsevier, 2016, pp. 125–188.

[8] D. LIEDERMAN, S. YURCHAK, J. C. W. KUO, and W. LEE, "MOBIL METHANOL-TO-GASOLINE PROCESS.," *J ENERGY*, vol. V 6, no. N 5, pp. 340–341, 1982, doi: 10.2514/3.62614.

[9] S. Hafeez, E. Pallari, G. Manos, and A. Constantinou, "Catalytic conversion and chemical recovery," in *Plastics to Energy: Fuel, Chemicals, and Sustainability Implications*, Elsevier, 2018, pp. 147–172.

[10] M. De Falco, "Ether (DME)," 2017, Accessed: Dec. 30, 2020. [Online]. Available: http://www.oil-gasportal.com/dimethyl-ether-dme-production-2/?print=pdf.

[11] ISPT, "Institute for Sustainable Process Technology Power to Ammonia," 2017. Accessed: Dec. 16, 2020. [Online]. Available: https://www.topsectorenergie.nl/sites/default/files/uploads/Energie en Industrie/Power to Ammonia 2017.pdf.

[12] Generon, "How Is Nitrogen Produced for Industrial Applications? | GENERON," 2020. https://www.generon.com/how-is-nitrogen-produced-for-industrial-applications/ (accessed Dec. 16, 2020).

[13] R. Service, "Ammonia—a renewable fuel made from sun, air, and water—could power the globe without carbon," *Science (80-.).*, Jul. 2018, doi: 10.1126/science.aau7489.

[14] H. Liu *et al.*, "Performance, combustion and emission characteristics of a diesel engine fueled with polyoxymethylene dimethyl ethers (PODE3-4)/ diesel blends," *Energy*, vol. 88, pp. 793–800, Aug. 2015, doi: 10.1016/j.energy.2015.05.088.

[15] J. Burger, M. Siegert, E. Ströfer, and H. Hasse, "Poly(oxymethylene) dimethyl ethers as components of tailored diesel fuel: Properties, synthesis and purification concepts," *Fuel*, vol. 89, no. 11, pp. 3315–3319, 2010, doi: 10.1016/j.fuel.2010.05.014.

[16] H. Liu, Z. Wang, J. Zhang, J. Wang, and S. Shuai, "Study on combustion and emission characteristics of Polyoxymethylene Dimethyl Ethers/diesel blends in light-duty and heavy-duty diesel engines," *Appl. Energy*, vol. 185, pp. 1393–1402, Jan. 2017, doi: 10.1016/j.apenergy.2015.10.183.

[17] Y. Zheng, Q. Tang, T. Wang, Y. Liao, and J. Wang, "Synthesis of a green fuel additive over cation resins," *Chem. Eng. Technol.*, vol. 36, no. 11, pp. 1951–1956, 2013, doi: 10.1002/ceat.201300360.

[18] S. E. Iannuzzi, C. Barro, K. Boulouchos, and J. Burger, "Combustion behavior and soot formation/oxidation of oxygenated fuels in a cylindrical constant volume chamber," *Fuel*, vol. 167, pp. 49–59, Mar. 2016, doi: 10.1016/j.fuel.2015.11.060.

[19] C. J. Baranowski, A. M. Bahmanpour, and O. Kröcher, "Catalytic synthesis of polyoxymethylene dimethyl ethers (OME): A review," *Appl. Catal. B Environ.*, vol. 217, pp. 407–420, 2017, doi: 10.1016/j.apcatb.2017.06.007.

[20] S. Deutz *et al.*, "Cleaner production of cleaner fuels: Wind-to-wheel-environmental assessment of CO2-based oxymethylene ether as a drop-in fuel," *Energy Environ. Sci.*,

vol. 11, no. 2, pp. 331–343, 2018, doi: 10.1039/c7ee01657c.

[21] C. H. Gierlich, K. Beydoun, J. Klankermayer, and R. Palkovits, "Challenges and Opportunities in the Production of Oxymethylene Dimethylether," *Chemie-Ingenieur-Technik*, vol. 92, no. 1–2, pp. 116–124, 2020, doi: 10.1002/cite.201900187.

[22] M. Ouda *et al.*, "Poly(oxymethylene) dimethyl ether synthesis-A combined chemical equilibrium investigation towards an increasingly efficient and potentially sustainable synthetic route," *React. Chem. Eng.*, vol. 2, no. 1, pp. 50–59, Feb. 2017, doi: 10.1039/c6re00145a.

[23] K. Thenert, K. Beydoun, J. Wiesenthal, W. Leitner, and J. Klankermayer, "Ruthenium-Catalyzed Synthesis of Dialkoxymethane Ethers Utilizing Carbon Dioxide and Molecular Hydrogen," *Angew. Chemie - Int. Ed.*, vol. 55, no. 40, pp. 12266–12269, 2016, doi: 10.1002/anie.201606427.

[24] Q. Zhao *et al.*, "Synthesis of polyoxymethylene dimethyl ethers from methanol and trioxymethylene with molecular sieves as catalysts," *Ranliao Huaxue Xuebao/Journal Fuel Chem. Technol.*, vol. 39, no. 12, pp. 918–923, 2011, doi: 10.1016/s1872-5813(12)60003-6.

[25] J. M. Tatibouët, "Methanol oxidation as a catalytic surface probe," *Applied Catalysis A: General*, vol. 148, no. 2. Elsevier, pp. 213–252, Jan. 02, 1997, doi: 10.1016/S0926-860X(96)00236-0.

[26] K. A. Thavornprasert, M. Capron, L. Jalowiecki-Duhamel, and F. Dumeignil, "One-pot 1,1-dimethoxymethane synthesis from methanol: A promising pathway over bifunctional catalysts," *Catal. Sci. Technol.*, vol. 6, no. 4, pp. 958–970, 2016, doi: 10.1039/c5cy01858g.

[27] B. G. Schieweck and J. Klankermayer, "Tailor-made Molecular Cobalt Catalyst System for the Selective Transformation of Carbon Dioxide to Dialkoxymethane Ethers," *Angew. Chemie - Int. Ed.*, vol. 56, no. 36, pp. 10854–10857, 2017, doi: 10.1002/anie.201702905.

[28] AVL List GmbH, "AVL FIRE Species Transport User Manual."

[29] AVL List GmbH, *AVL FIRE CFD Solver User Manual*. 2014.

[30] AVL List GmbH, *AVL FIRE Spray User Manual*, 2020 R2. 2020.

[31] AVL List GmbH, *AVL FIRE General Gas Phase Reactions Module User Manual*. 2017.

[32] AVL List GmbH, "AVL FIRE Combustion User Manual."

[33] O. Colin and A. Benkenida, "The 3-Zones Extended Coherent Flame Model \(Ecfm3z\) for Computing Premixed/Diffusion Combustion; The 3-Zones Extended Coherent Flame Model \(Ecfm3z\) for Computing Premixed/Diffusion Combustion," 2004, doi: 10.2516/ogst:2004043ï.

[34] AVL List GmbH, "AVL FIRE Emission User Manual," 2020.

[35] Q. Lin, K. L. Tay, D. Zhou, and W. Yang, "Development of a compact and robust Polyoxymethylene Dimethyl Ether 3 reaction mechanism for internal combustion engines," *Energy Convers. Manag.*, vol. 185, no. February, pp. 35–43, 2019, doi: 10.1016/j.enconman.2019.02.007.